UNIVERSITY OF CALIFORNIA,
IRVINE

Informing Dark Matter Indirect Detection with FIRE Simulations and Providing New Constraints

DISSERTATION

submitted in partial satisfaction of the requirements
for the degree of

DOCTOR OF PHILOSOPHY

in Physics

by

Daniel McKeown

Dissertation Committee:
Professor James Bullock, Chair
Professor Kevork Abazajian
Professor Simona Murgia

2022

DEDICATION

To my parents and my son Elijah

TABLE OF CONTENTS

LIST OF FIGURES

LIST OF TABLES

ACKNOWLEDGMENTS

This moment is the culmination of a 12 year journey that began at Saint Louis Community College, where I started taking my first classes. I want to thank Dr. Bob Larson, who was my first physics teacher, for a wonderful introduction to the subject. Every day he brought a new and challenging set of problems and discussions for me to ponder over. After two years at Saint Louis Community College, I transferred to the University of Missouri at Saint Louis, where I had a great Undergraduate experience. In particular, I want to thank Dr. Erika Gibb, for giving me my first opportunity to do research with her in her lab on Comet Ison, the summer after my Junior year. It was my very first research experience, and I gained incredibly valuable insights from her. I also want to thank Dr. Bob Henson, who went the extra mile to ensure that I got all my questions answered, and who often stayed after class to answer any follow up questions I had. Finally, I want to thank Dr. Ta-Pei Cheng for his wonderful introduction to Relativity course, and for his advice and insights he gave me about applying to graduate schools.

After graduating from University of Missouri Saint Louis with B.S. in Physics, I completed my M.S. in Physics with emphasis in Astronomy at San Francisco State University. It was there that I had my first experience researching with Galaxy Simulations, working with the very talented Dr. Andy Mahdavi. I am forever grateful for Andy's insights, and helping me gain the opportunity to do research on the Illustris simulations.

Now I want to thank everyone at University of California Irvine, who have been so encouraging and amazing as mentors, advisors, and colleagues. In particular, I want to thank Jose Flores Velazquez for a wonderful friendship. I will never forget BBQing with you and Elijah at the Verano Commons, and your smile will forever endure in my mind. I miss you brother. I also want to thank everyone in the Bullock Group for all your insights during meetings. You have been a great group to work with. members, Dr. Kevork Abazajian and Dr. Simona Murgia for all the help and time they have provided. Finally, I want to thank Dr. James Bullock for being the greatest mentor ever to me. I am so glad I was able to join James' group and had the opportunity to learn from him and his wisdom.

This journey in some sense is just beginning. I have an incredible amount of new ideas thanks to all the wonderful insights and exposure to the fascinating scientific problems, mysteries and puzzles that continue to illuminate the human imagination and mind. Questioning,thinking over, and attempting to unravel these things is the ultimate life pursuit.

DM is supported by NSF grant AST-1910346.

The text of a portion of this dissertation (Chapters 1 and 2) is a reprint of the material as it appears in (**D. McKeown**, J. S. Bullock, F. Mercado, Z. Hafen,M. Boylan-Kolchin , A. Wetzel, L Necib, P Hopkins, S. Yu *Amplified J-factors in the Galactic Centre for velocity-dependent dark matter annihilation in FIRE simulations*, Monthly Notices of the Royal Astronomical Society,513, no. 1 (2022): pages 55-70.). The co-authors listed in this publication are James Bullock, Francisco Mercado, Zach Hafen, M. Boylan-Kolchin, Andrew

Wetzel, Lina Necib, Philip Hopkins and S. Yu.

VITA

Daniel McKeown

EDUCATION

Doctor of Philosophy in Physics **2022**
University of California Irvine *Irvine, Ca.*

Master's of Science in Physics **2017**
San Francisco State University *San Francisco, Ca.*

Bachelor of Science in Physics **2014**
University of Missouri-Saint Louis *Saint Louis, Mo.*

RESEARCH EXPERIENCE

Graduate Student Researcher **2018–2022**
University of California, Irvine *Irvine, California*

Graduate Research Assistant **2016–2017**
San Francisco State University *San Francisco, California*

TEACHING EXPERIENCE

Graduate Teaching Assistant **2017–2018**
University of California Irvine *Irvine, Ca.*

Graduate Teaching Assistant **2014–2016**
San Francisco State University *San Francisco, Ca.*

REFEREED JOURNAL PUBLICATIONS

1. **D. McKeown**, J. S. Bullock, F. Mercado, Z. Hafen,M. Boylan-Kolchin , A. Wetzel, L Necib, P Hopkins, S. Yu *Amplified J-factors in the Galactic Centre for velocity-dependent dark matter annihilation in FIRE simulations*, Monthly Notices of the Royal Astronomical Society,513, no. 1 (2022): pages 55-70.

ABSTRACT OF THE DISSERTATION

Informing Dark Matter Indirect Detection with FIRE Simulations and Providing New Constraints

By

Daniel McKeown

Doctor of Philosophy in Physics

University of California, Irvine, 2022

Professor James Bullock, Chair

We use FIRE-2 zoom cosmological simulations of Milky Way size galaxy halos to calculate astrophysical J-factors for dark matter annihilation and indirect detection studies. In addition to velocity-independent (s-wave) annihilation cross sections $\langle \sigma v \rangle$, we also calculate effective J-factors for velocity-dependent models, where the annihilation cross section is either either p-wave ($\propto v^2/c^2$) or d-wave ($\propto v^4/c^4$). We use 12 pairs of simulations, each run with dark-matter-only (DMO) physics and FIRE-2 physics. We observe FIRE runs produce central dark matter velocity dispersions that are systematically larger than in DMO runs by factors of $\sim 2.5-4$. They also have a larger range of central (~ 400 pc) dark matter densities than the DMO runs ($\rho_{\rm FIRE}/\rho_{\rm DMO} \simeq 0.5-3$) owing to the competing effects of baryonic contraction and feedback. At 3 degrees from the Galactic Center, FIRE J-factors are $3-60$ (p-wave) and $10-500$ (d-wave) times higher than in the DMO runs. The change in s-wave signal at 3 degrees is more modest and can be higher or lower ($\sim 0.3-7$). We find these results for s-wave are broadly consistent with the range of assumptions in most indirect detection studies, though our p-wave and d-wave values are significantly enhanced compared to what is commonly adopted. Contrary to past estimates, we suggest that thermal models with p-wave annihilation may be within range of detection in the near future. We then look at the shapes of the emission signal and find that the shape of the predicted J-factor-scaled

emission is significantly different in FIRE compared to DMO. Contours of constant J on the sky are well-fit by ellipses. At a fixed fraction of peak J-factor on the sky, DMO runs have short-to-long axis ratios that are typically elliptical at ~ 0.6, though demonstrate a broad range from $0.4 - 0.95$. The FIRE runs are usually rounder, with axis ratios ~ 0.8, and, importantly have narrower range of expected shapes ($\sim 0.7 - 0.85$). The long axis is always aligned with the Galactic plane in the FIRE simulations, to within $\sim 5^{\circ}$. These predictions should be useful as priors in dark matter indirect detection studies, providing new constraints for a detection signal that our high resolution simulations have allowed.

Chapter 1

Introduction

There is significant astrophysical and cosmological evidence showing that non-baryonic dark matter dominates the mass in the Universe [30, 76, 86, 89, 62, 57]. Cosmological constraints have pinpointed that the dark matter mass density relative to critical is $\Omega_{\rm dm} \simeq 0.27$ today, [73]. For a comprehensive historical perspective on the observational and theoretical motivations for dark matter Ref.[13].

One popular theory for dark matter suggests that it is made up of Weakly Interacting Massive Particles (WIMPs) see [48, 29, 32, 14, 65] for in depth discussions. In the standard WIMP scenario, where dark matter particles are their own antiparticles, WIMPs self-annihilate and recombine in equilibrium when the Universe is young, hot, and dense. As the Universe cools and expands, annihilation rates become too low to maintain equilibrium, and the co-moving particle abundance "freezes out." The resultant abundance is set directly by the interaction cross section during freeze-out, and this gives us a way to relate a macroscopic observable ($\Omega_{\rm dm} \simeq 0.27$) to microscopic properties of the particle. Specifically, if the thermally-averaged cross-section during freeze out is $\langle \sigma_A v \rangle \equiv \langle \sigma_A v \rangle_T \simeq 2.3 \times 10^{-26}$ cm^3 s^{-1}, then the thermal relic density is naturally of the right order of magnitude to match the observed abundance

[83].

The same annihilations that set the thermal abundance of WIMPs in the early Universe should be occurring again today in regions where the dark matter has become dense in dark matter halos. If those annihilations produce Standard Model particles, this provides a means for indirect dark matter detection. Specifically, an observed flux of Standard Model particles from such a location could provide evidence for dark matter. One region of particular interest is the Galactic Center [11]. Not only is the Galactic Center expected to be dense in dark matter but its relative proximity to Earth has made it a subject of significant study for indirect messengers of annihilation, including cosmic rays and neutrinos (see [38] for a full review). If annihilation to quarks and charged lepton states happens for dark matter particles, this will ultimately produce photons with energies of order $\sim 10\%$ of the dark matter particle mass, making gamma-ray observations of particular interest for indirect searches for WIMP dark matter with $m_\chi \sim 100$ GeV [23].

An observed excess in gamma-ray emission from the Galactic Center based on Fermi Large Area Telescope observations has sparked considerable interest as a potential indirect detection signal [44, 3, 63, 6, 5]. The basic excess has been confirmed by multiple groups [67] and is consistent with expectations for a dark matter particle with mass $m_\chi \sim 10 - 100$ GeV annihilating with a velocity-averaged cross section that matches the thermal WIMP expectation. A different signal from the Andromeda galaxy halo is potentially consistent with this interpretation [50]. Although a dark matter origin of the Galactic Center Excess (GCE) is the most intriguing possibility, astrophysical sources, including gamma-ray emitting pulsars [1, 9] and supernovae remnants [19] are plausible alternatives.

The case for an astrophysical interpretation has been strengthened over the last several years, with analyses showing that the morphology of the excess traces the flattened "boxy" stellar over-density of the Galactic bulge, rather than the more spherical distribution one would expect for a dark matter signal [61, 10]. Based on this realization, Ref.[2] used templates for

the galactic and nuclear stellar bulges to show that the GC shows no significant evidence for DM annihilation and used this to place strong constraints on the s-wave cross section. In particular, in the case of a pure b-quark annihilation channel, assuming a range of DM profiles consistent with numerical simulations, [2] ruled out s-wave cross sections $\gtrsim 0.015\langle\sigma_A v\rangle_T$ for dark matter masses $m_\chi \sim 10$ GeV.

One way that this thermal limit could be avoided is if dark matter annihilation is velocity-dependent [74, 39, 20, 72, 16, 47, 8, 15]. Specifically, in some models, symmetries forbid the s-wave contribution to the annihilation cross-section, and the leading contribution to DM annihilations could be p-wave $\sigma v \propto (v/c)^2$ or even d-wave $\sigma v \propto (v/c)^4$. In the Milky Way, typical DM velocities are usually thought to be $\sim 3 \times 10^{-4} c$ near the Galactic Center, while at thermal freeze out $v \sim 0.1c$. This means that for p-wave, the cross section is expected to be suppressed by a factor of $\sim 10^{-5}$ compared to the value during freeze-out.

For a fixed particle physics model with s-wave annihilation, the expected annihilation signal depends on the square of the dark matter density along the line-of-sight from the observer. This "astrophysical J-factor" is therefore critical to the interpretation of any indirect dark matter search [84, 27, 82, 49, 40]. It is common for interpretive analyses to adopt analytic priors for the dark matter profile shape inferred from cosmological simulations and to normalize the profiles so that the local dark matter density near the Sun matches observationally-inferred values [68]. For velocity-dependent models, the J-factor is generalized to include the local velocity distribution Ref.[16]. Recently, Ref.[15] used several cosmological zoom hydrodynamical simulations to investigate the generalized J-factor for velocity dependent models for Milky-Way size galaxies. They found that J-factors were enhanced for hydrodynamic runs in p and d-wave cases. They also concluded that the J-factor in all models was strongly correlated with the local dark matter density.

In this paper, we perform a similar analysis to that in Ref. [15] utilizing 12 Milky Way mass zoom simulations done as part of the FIRE-2 collaboration [87, 35, 46, 33, 58]. For

each halo, we have a dark-matter-only version, and this allows us to explore the differential effect of galaxy formation physics on J-factor predictions. However, our analysis goes beyond that of Ref. [15] in many ways, most importantly, in terms of having much higher angular resolution than their analysis. As we will see, an incredible amount of physics concerning J-factors occurs in the very center of galaxies in our simulations, which greatly affects the results of J-factors both in terms of their shapes, magnitudes, and how the signal varies from halo to halo as well. These results, particularly the high variance from halo to halo in terms of signal, were unexpected and have important implications which we discuss in the next Chapters.

Chapter 2

J - factors

In this chapter, we perform a similar analysis to that in Ref. [15] utilizing 12 Milky Way mass zoom simulations done as part of the FIRE-2 collaboration [87, 35, 46, 33, 58]. For each halo, we have a dark-matter-only version, and this allows us to explore the differential effect of galaxy formation physics on J-factor predictions. We can thus directly compare how J-factor emissions are effected by the dynamics of stars and gas via their interactions on the dark matter particles, since both dark matter density distributions and velocity distributions are affected by interactions with baryonic components of the galaxy or group of galaxies.

Compared to the work of Ref.[15], our work extends analysis of J-factors in 3 significant ways. First, our simulations have $\sim$ 10 times better mass resolution and this allows us to resolve the J-factor ~ 3 times closer the Galactic Center (within 2.75°) than they were able to do. Second, we do not assume spherical symmetry in our analysis, and this allows us to explore the shape of emission on the sky. We make no assumptions as to the shape of the emission, and we use the local values of both density and velocity differences for the calculation of our J-factors which allows us to look at the shape of emission on the sky, which we will discuss in depth in Chapter 3. Finally, we re-normalize every halo so that

the local dark matter density at mock solar locations are identical. This allows us to mimic what is done in indirect detection analyses and to explore how differences in the shape of the dark matter density and velocity profile will affect J-factor predictions from simulation to simulation in a way scales out the expected dependence on local density. Furthermore, 6 of the simulations we analyze are galaxy pairs, closely matching and relating to our own Milky Way/Andromeda galaxy pair. This gives us the added advantage of having a more realistic representation of the galactic components and their mutual interaction. Finally, for our full hydrodynamic simulations, we have the benefit having some of the most accurate and realistic feedback mechanics implemented into the galactic dynamics via FIRE-2 [45].

2.1 Overview of Simulations

Our analysis relies on cosmological zoom-in simulations performed as part of the Feedback In Realistic Environments (FIRE) project[1] with FIRE-2 feedback implementation [46] with the gravity plus hydrodynamics code GIZMO [45]. FIRE-2 includes radiative heating and cooling for gas with temperatures ranging from 10 K to 10^{10} K, an ionising background [31], stellar feedback from OB stars, AGB mass-loss, type Ia and type II supernovae, photoelectric heating, and radiation pressure. Star formation occurs in gas that is locally self-gravitating, sufficiently dense (> 1000 cm^{-3}), Jeans unstable, and molecular (following [56]). Locally, the star formation efficiency is set to 100% per free-fall time, though the global efficiency of star formation within a giant-molecular cloud (or across larger scales) is self-regulated by feedback to $\sim$1-10% per free-fall time [70].

In this work, we analyse 12 Milky-Way-mass galaxies (Tables 2.1, 2.2,2.3,2.4). These zoom simulations are initialised following the approach outlined in [69] using the MUSIC code [43]. Six of these galaxies were run as part of the Latte suite [87, 36, 33, 78, 46] and have names

[1] `https://fire.northwestern.edu/`

Table 2.1: (1) Simulation name. The suffix "DMO" stands for "Dark Matter Only" and refers to the same simulation run with no hydrodynamics or galaxy formation physics. (2) Factor f by which dark matter particle masses have been multiplied ($m_{\rm dm} \rightarrow f m_{\rm dm}$) in order to normalize the dark matter density at $\rho(r = R_\odot) = 10^7\ M_\odot {\rm kpc}^{-3} = 0.38 {\rm GeV\ cm}^{-3}$ for a mock solar location $R_\odot = 8.3$ kpc. (3) Stellar mass $M_\star$ of the central galaxy. (4) Virial mass (of raw simulation, not including the f factor) defined by [18]. The following quantities are derived after normalizing (by f) to the local dark matter density: (5) Cumulative s-wave J-factor within 3 degrees of the Galactic Center. (6) Cumulative s-wave J-factor within 10 degrees of the Galactic Center. (7) Cumulative s-wave J-factor integrated over the sky.

Simulation	f	$M_\star$ 10^{10} $M_\odot$	$M_{\rm vir}$ 10^{12} $M_\odot$	$J_s(<3^\circ)$	$J_s(<10^\circ)$ (10^{22}	$J_s^{\rm tot}$ GeV^2 cm^{-3})
`M12i`	1.28	6.4	0.90	1.34	7.05	17.6
`M12iDMO`	1.59	-	1.3	0.489	2.33	9.58
`M12c`	1.26	6.0	1.1	1.16	6.27	17.6
`M12cDMO`	1.83	-	1.3	1.27	5.10	14.3
`M12m`	0.885	11	1.2	0.607	3.92	13.9
`M12mDMO`	1.42	-	1.4	1.56	6.12	15.3
`M12f`	1.01	8.6	1.3	0.978	5.93	16.2
`M12fDMO`	1.82	-	1.6	1.22	4.87	14.1
`M12w`	1.28	5.8	0.83	1.32	5.60	15.6
`M12wDMO`	1.68	-	1.1	0.798	3.24	11.0
`M12b`	0.990	8.1	1.1	1.17	6.97	17.7
`M12bDMO`	1.25	-	1.4	2.06	7.09	18.6

Table 2.2: (1) Simulation name. The suffix “DMO" stands for “Dark Matter Only" and refers to the same simulation run with no hydrodynamics or galaxy formation physics. (2) Cumulative p-wave J-factor within 3 degrees of the Galactic Center. (3) Cumulative p-wave J-factor within 10 degrees of the Galactic Center.(4) Cumulative p-wave J-factor integrated over the sky. (5) Cumulative d-wave J-factor within 3 degrees of the Galactic Center. (6) Cumulative d-wave J-factor within 10 degrees of the Galactic Center. (7) Cumulative d-wave J-factor integrated over the sky.

Simulation	$J_p(< 3^\circ)$	$J_p(< 10^\circ)$	$J_p^{\rm tot}$	$J_d(< 3^\circ)$	$J_d(< 10^\circ)$	$J_d^{\rm tot}$
		(10^{16} GeV^2 cm^{-3})			(10^{10} GeV^2 cm^{-3})	
M12i	4.90	22.1	44.7	24.6	95.9	163
M12iDMO	0.137	0.913	5.73	0.066	0.572	5.13
M12c	3.74	17.8	39.8	16.6	69.6	130
M12cDMO	0.294	1.65	6.62	0.112	0.843	4.70
M12m	2.46	14.3	41.3	13.7	71.9	174
M12mDMO	0.490	2.52	8.56	0.237	1.56	7.21
M12f	4.05	21.3	47.2	23.2	106	197
M12fDMO	0.316	1.73	7.65	0.131	0.960	6.54
M12w	3.91	15.5	34.8	15.9	58.6	111
M12wDMO	0.212	1.26	6.23	0.093	0.757	5.18
M12b	6.49	31.2	60.5	50.6	198	310
M12bDMO	0.791	3.74	13.6	0.462	2.96	14.7

Table 2.3: Halo properties and s-wave J factor values for paired runs (MW and Andromeda. Description for column values same as with table 2.1

Simulation	f	$M_\star$ 10^{10} $M_\odot$	M_{vir} 10^{12} $M_\odot$	$J_s(<3^\circ)$	$J_s(<10^\circ)$ (10^{22}	J_s^{tot} GeV^2 cm^{-3})
Romeo	0.99	7.4	1.0	4.50	15.7	27.7
RomeoDMO	1.26	-	1.2	3.07	8.83	18.3
Juliet	1.31	4.2	0.85	4.43	15.5	26.4
JulietDMO	1.59	-	1.0	3.72	11.0	23.7
Thelma	1.17	7.9	1.1	0.391	2.81	11.5
ThelmaDMO	1.70	-	1.3	1.27	4.80	13.2
Louise	1.42	2.9	0.85	1.28	6.85	17.9
LouiseDMO	1.41	-	1.0	1.79	6.68	19.6
Romulus	1.00	10	1.53	7.95	19.9	31.4
RomulusDMO	1.01	-	1.9	1.19	4.83	13.9
Remus	1.10	5.1	0.97	2.04	8.90	19.9
RemusDMO	1.18	-	1.3	2.26	7.91	19.7

Table 2.4: J factor values (p and d wave)for paired runs MW and Andromeda. Description for column values same as with prior table 2.2

Simulation	$J_p(< 3^\circ)$	$J_p(< 10^\circ)$ (10^{16} GeV^2 cm^{-3})	$J_p^{\rm tot}$	$J_d(< 3^\circ)$	$J_d(< 10^\circ)$ (10^{10} GeV^2 cm^{-3})	$J_d^{\rm tot}$
Romeo	10.9	37.7	64.2	36.1	123	203
RomeoDMO	1.08	4.30	12.5	0.584	3.22	13.1
Juliet	11.4	35.0	52.4	40.6	109	148
JulietDMO	1.13	4.74	12.6	0.543	3.08	10.0
Thelma	1.31	8.67	28.5	6.04	36.7	99.9
ThelmaDMO	0.310	1.69	7.36	0.129	0.986	6.55
Louise	2.17	10.7	25.4	4.99	22.9	49.6
LouiseDMO	0.661	3.40	12.6	0.373	2.55	11.7
Romulus	28.5	66.8	97.8	139	306	421
RomulusDMO	0.531	3.00	12.5	0.385	2.91	17.0
Remus	4.98	20.5	41.3	16.6	64.3	119
RemusDMO	0.933	4.46	14.9	0.596	3.78	16.8

following the convention `m12*`. The other six, with names associated with famous duos, are set in paired configurations to mimic the Milky Way and M31 [33, 37]. Analysis has shown these are good candidates for comparison with the Milky Way [80]. Gas particles for the `M12*` runs have initial masses of $m_{\rm g,i} = 7070\ M_\odot$. The ELVIS on FIRE simulations have roughly two times better mass resolution ($m_{\rm g,i} \simeq 3500 - 4000\ M_\odot$). Gas softening lengths are fully adaptive down to $\simeq$0.5$-$1 pc. The dark matter particle masses are $m_{\rm dm} = 3.5 \times 10^4\ M_\odot$for the Latte simulations and $m_{\rm dm} \simeq 2 \times 10^4\ M_\odot$for the ELVIS runs. Star particle softening lengths are $\simeq$4 pc physical and a dark matter force softening is $\simeq$40 pc physical.

Lastly, each FIRE simulation has an analogous dark matter only (DMO) version. The individual dark matter particle masses in the DMO simulations are larger by a factor of $(1 - f_{\rm b})^{-1}$ in order to keep the total gravitating mass of the Universe the same, where $f_{\rm b} = \Omega_{\rm b}/\Omega_{\rm m}$ is the cosmic baryon fraction. The initial conditions are otherwise identical. DMO versions of each halo are referred to with the same name as the FIRE version with the added suffix "DMO."

As can be seen in Table 2.1 and 2.3, the stellar masses of the main galaxy in each FIRE run (second column) are broadly in line with the Milky Way: $M_\star \approx (3 - 11) \times 10^{10}\ M_\odot$. The virial masses [18] of all the halos in these simulation span a range generally in line with expectations for the Milky Way: $M_{\rm vir} \approx (0.9 - 1.8) \times 10^{12}\ M_\odot$. In every case, the DMO version of each pair ends up with a higher virial mass. This is consistent with the expectation that halos will have lost their share of cosmic mass by not retaining all baryons in association with feedback. As we discuss in the next section, in our primary analysis we re-normalize all halos (both FIRE and DMO runs) so that they have the same "local" dark matter density at the Solar location (by the factor f listed in the tables 2.1 and 2.3.).

2.2 Dark Matter Density and Velocity Dispersion Profiles

Ref.[58] provide an extensive discussion of the dark matter halo density profiles for the simulations we analyze here. Every system has more than $\sim$ 1000 dark matter particles within the inner 400pc and is converged outside of this radius according to the criteria discussed [46]. Though some systems are even better converged, for simplicity we adopt the same convergence radius, $r_{\rm conv} = 400$pc, for each halo and only present values that depend on quantities outside of this radius. For an adopted Solar location at radius $R_\odot = 8.3$ kpc, our 400 pc convergence radius corresponds to an angle $\psi = 2.75^\circ$ in projection at the Galactic Center.

Figures 2.1 and 2.2 show the spherically-averaged density and velocity dispersion profiles of the simulations in our sample. The first two plots in figure 2.1 on page 13 show raw simulation results, with differential density profiles on at the top and velocity-dispersion profiles on the bottom. For both density and velocity dispersion profiles,the DMO simulations are in black and FIRE runs are in blue.

2.2.1 Dark Matter Density Profiles

Note that the density profiles of the FIRE runs are systematically steeper for $r \gtrsim 3$ kpc than the DMO runs. This is consistent with the expectations that baryonic contraction makes halos more concentrated at this stellar-mass scale [58]. At smaller radii ($r \lesssim 3$ kpc), however, the FIRE halos have a larger range of central densities; sometimes feedback produces a core-like profile and sometimes the halo remains fairly steep. For an investigation into the origin of this variation see [64].

.

2.2.2 Dark Matter Velocity-Dispersion Profiles

The FIRE halos also have systematically higher central dark matter velocity dispersion than the DMO runs. A similar result was reported by [75], which studied the velocity dispersion profiles of cold dark matter halos using zoom in dark matter simulations that included a slowly-grown Milky-Way disk potential. In these simulations, even without feedback, they found that the central velocity dispersion of the dark matter was much higher in runs with disk potentials compared to those without. [15] also found that the central dark matter velocity dispersion was higher in simulations that included full galaxy formation physics (though with a different implementation than our own). Taken together, these results suggest that the dark matter velocity dispersion at the center of Milky-Way mass halos should be significantly higher than would be expected from DMO simulations, irrespective of galaxy formation model.

2.2.3 Comparisons of Profiles after re-scaling

The pair of panels of Figure 2.2 on page 14 show the profiles after we have re-scaled them to the defaults we will use in the rest of the analysis. Our aim here is to normalize each run to have the same local dark matter density at the solar location $r = R_{\odot}$. We are motivated to do this because it is customary in indirect-detection analyses to normalize the assumed profile at $R_{\odot}$ and to marginalize about the local density range inferred by observations. Note that even when normalized at the solar radius, there is almost an order of magnitude scatter in the inner ($\sim$ 400pc) density for the FIRE simulations. This reveals that full feedback effects and galactic dynamics have a significant influence on dark matter distributions and can affect them very strongly in the galactic center, showing a much wider variance in this

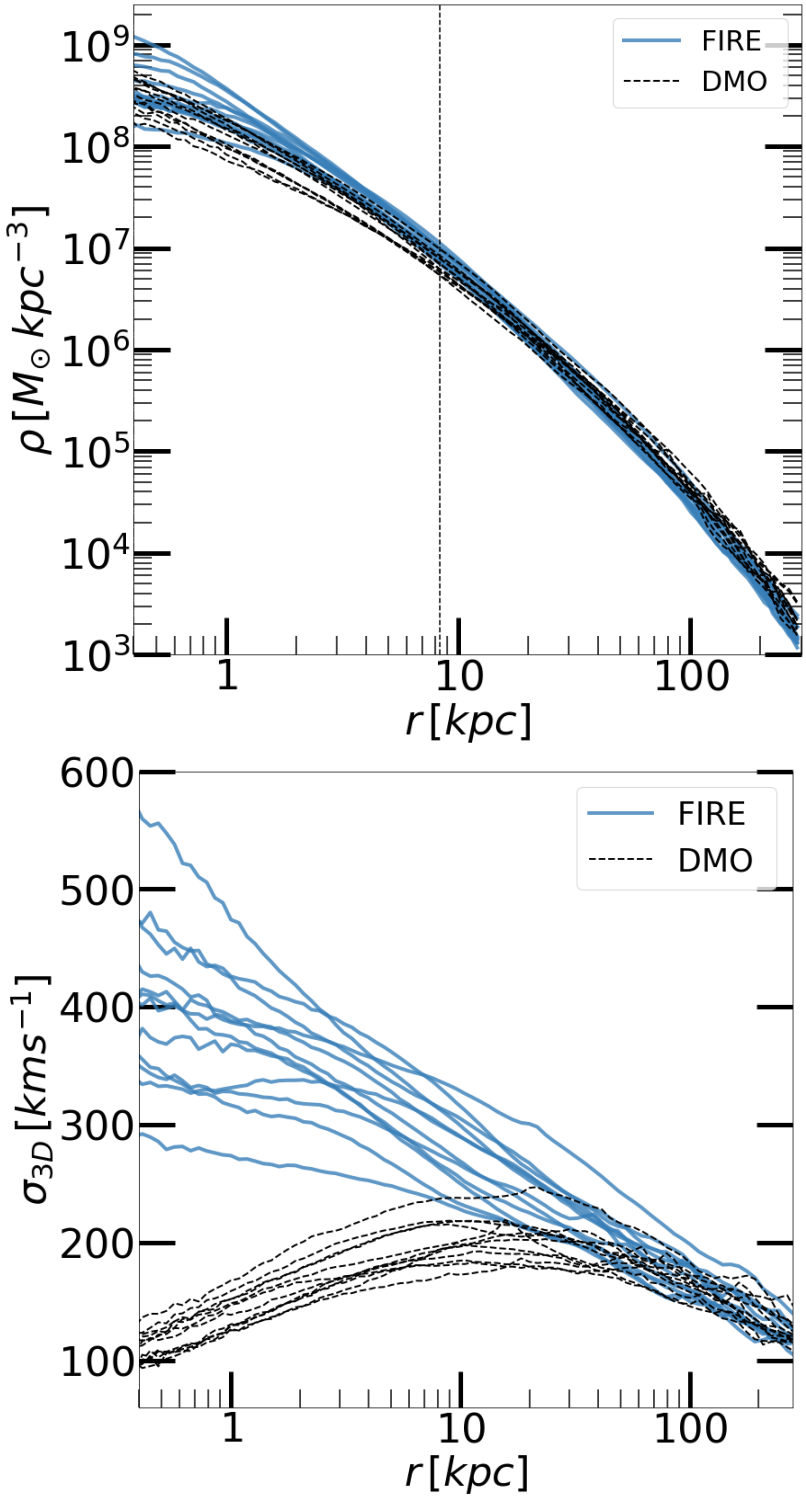

Figure 2.1: **Top**
Simulated dark matter halo density profiles for all DMO (dashed) and FIRE (solid) runs (solid). **Bottom:** Three-dimensional dark matter velocity dispersion profiles for all DMO (dashed) and FIRE (solid) simulations.

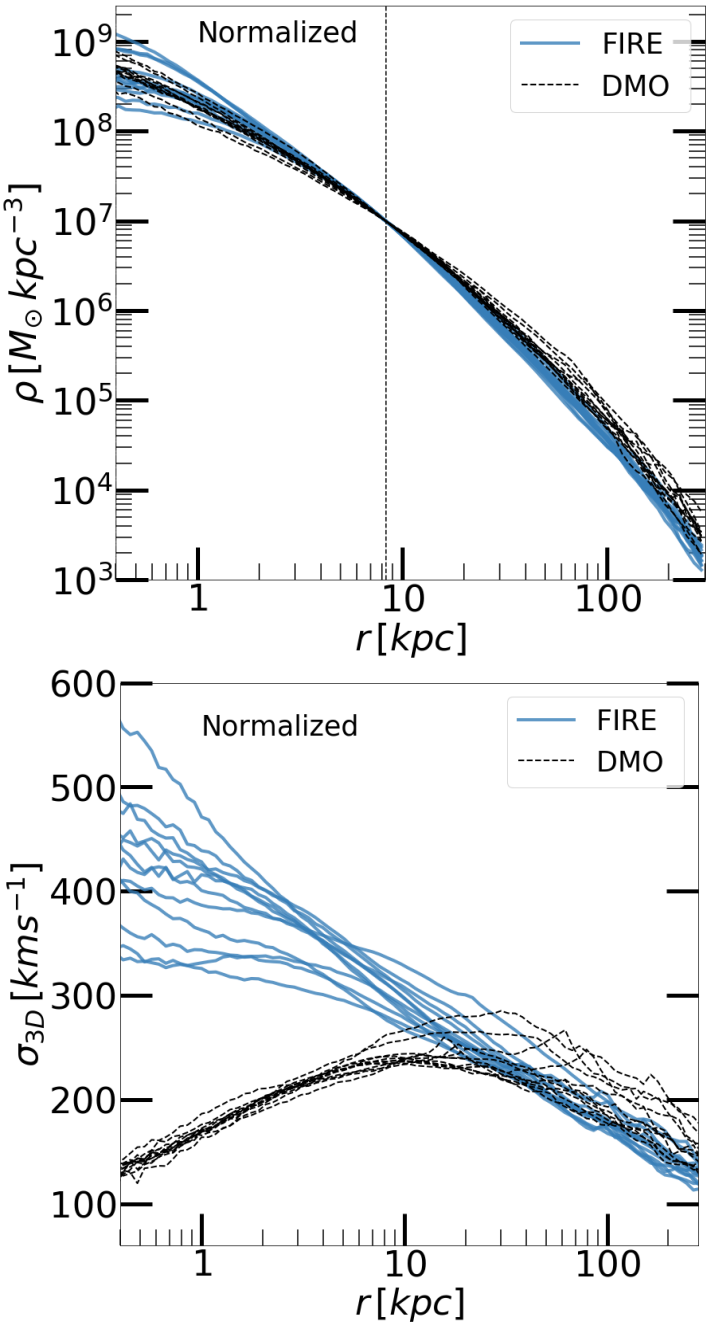

Figure 2.2: **Top** Dark matter density profiles after re-normalizing. The mass per particle in each simulation has been multiplied by a factor f (ranging from $f = 0.89 - 1.8$, see Tables 1 and 3) to give them the same density at a mock solar location: $\rho(r = R_\odot) = 10^7\ M_\odot \mathrm{kpc}^{-3}$ with $R_\odot = 8.3$ kpc (vertical dotted line). **Bottom** Velocity dispersion profiles for each halo after re-scaling the particle velocities by a factor $\sqrt{f}$. This roughly accounts for the re-scaling of the mass/density profile. Note that after re-scaling, the DMO velocity dispersion profiles become similar for $r \lesssim R_\odot$. Even when normalized, there is almost an order of magnitude scatter in the inner (~ 400pc) density for the FIRE simulations.

inner galactic region than their DMO counterparts.

In 2.2 we have also plotted the velocity dispersion profiles for each halo after re-scaling the particle velocities by a factor $\sqrt{f}$. This roughly accounts for the re-scaling of the mass/density profile. Note that after re-scaling, the DMO velocity dispersion profiles become similar for $r \lesssim R_\odot$. Note that they all have higher central dark matter velocities than would have been expected from DMO simulations.

While our halos are Milky-Way like in virial mass and stellar mass, they are not precise replicas of the Milky Way. By re-normalizing at the solar location, our results become primarily about profile *shape* rather normalization, and can be scaled appropriately as observational estimates of the local density become more precise. We assume $R_\odot = 8.3$ kpc (vertical dotted lines in the left panels) and set the density there to be $\rho(r = R_\odot) = 10^7\ M_\odot \mathrm{kpc}^{-3} = 0.38$ GeV cm^{-3} [41]. We do this by scaling the particle masses in each simulation (post process) by a factor f: $\mathrm{m_{dm}} \rightarrow f\,\mathrm{m_{dm}}$. The values of f for each simulation are given in Table 1 and range from $f = 1.8$ to $f = 0.89$. We also re-scale the particle velocities in each simulation by a factor[2] $\sqrt{f}$ in order to roughly account for the re-scaling of the total mass: $v \rightarrow \sqrt{f}v$. Note that after re-scaling, the DMO velocity dispersion profiles become similar for $r \lesssim R_\odot$, as expected.

Even when normalized at the Solar radius, there is considerable scatter in the inner density and the FIRE simulations display more variance than the DMO simulations. The difference between DMO and FIRE is most systematic in the inner velocity dispersion (of Figure 2.2). While the normalized DMO simulations all have $\sigma \simeq 140\,\mathrm{km\,s^{-1}}$ at $r = 400$ pc, the FIRE runs have $\sigma \simeq 350 - 550\,\mathrm{km\,s^{-1}}$ at the same radius. While this scatter is interesting to note, giving a precise and detailed answer as to why it occurs while require more analysis and is the topic for future analysis. For this present paper, we note that it exists, and that is has

[2]This assumes $v \propto \sqrt{fM/r}$. We have checked that the dark matter velocity dispersion in our simulations does roughly scale with the local dark matter density as $\sqrt{f}$.

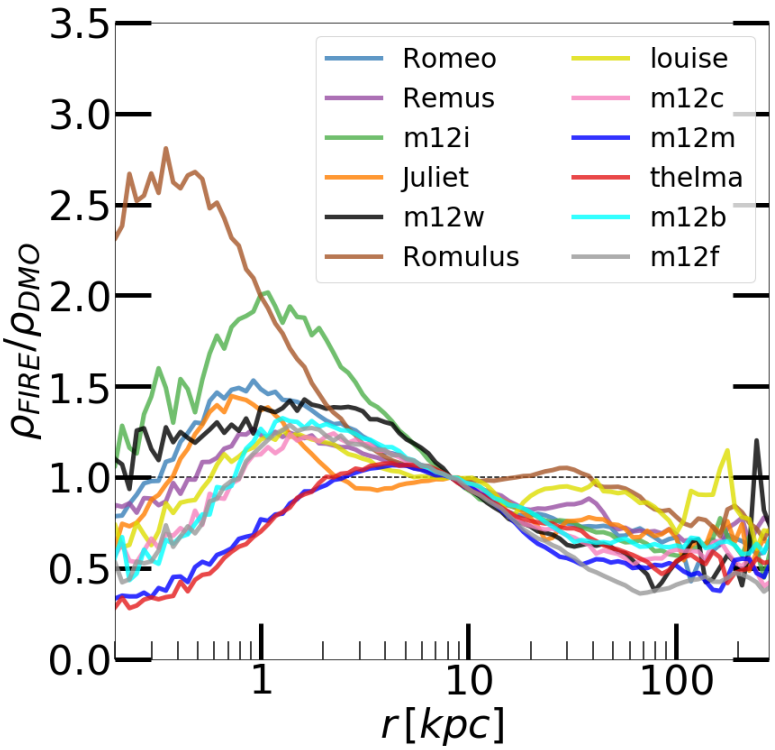

Figure 2.3: The ratio of the FIRE dark matter density profiles shown in Figure 2.1 to its DMO counterpart. We see that in some cases the FIRE runs are less dense than the DMO runs though most halos get denser at small radius in response to galaxy formation.

a significant impact on the magnitude of the J-factor signal, so that the total magnitude of the J-factor signal varies quite significantly from halo to halo.

2.2.4 Fire/DMO ratios for normalized density and velocity distributions

Figures 2.3 and 2.4 show FIRE to DMO ratios for the normalized density profile and velocity dispersion profile of each halo pair of 2.2. Looking at figure 2.3 we see that galaxy formation has generally made the halos less dense at large radii, corresponding to steeper (contracted) density profile.

The effect of galaxy formation on the inner density is quite varied, with some systems (e.g.

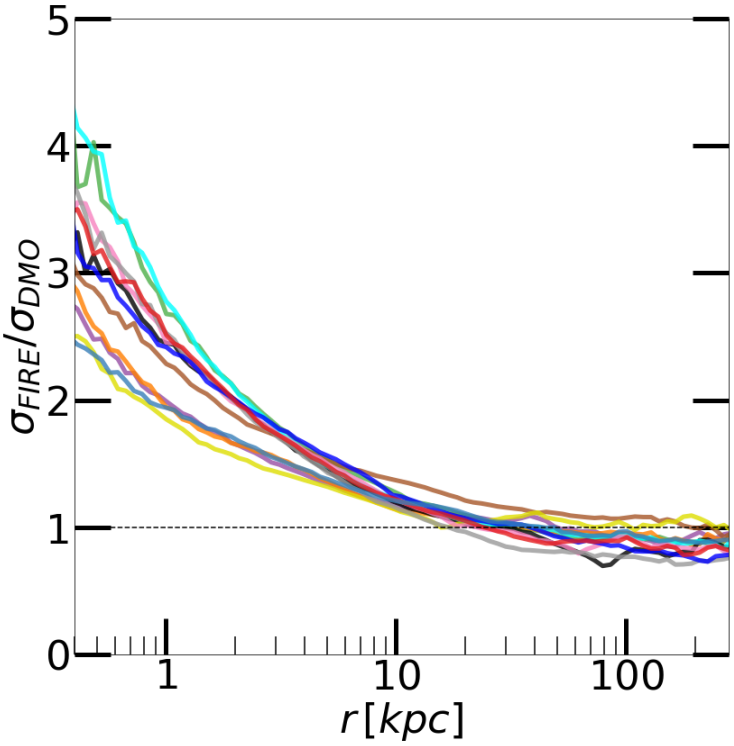

Figure 2.4: The ratio of the FIRE dark matter halo velocity dispersion profiles shown in Figure 2.1 divided by the DMO version for each halo. We see that in every case, the process of galaxy formation heats the dark matter at small radius.

Romulus and Romeo) displaying higher central densities in the FIRE runs, while others (e.g. Thelma and m12m) have lower densities. There is no clear trend with stellar mass or virial mass associated with these differences. Thelma and Romeo, for example, have very similar galaxy masses and virial masses but galaxy formation seems to have had an opposite effect on their relative density profiles. This is likely an artifact of some of the important baryonic differences between halos at late times, which are studied in other papers: some have late-occurring minor mergers or strong stellar bars [79, 24], (which tend to push DM outwards and lower central densities). Others have strong torques or early multiple-mergers which produce inflows and dense bulges and more compact disks [34, 60]. For the purposes of this paper, it is noted that it impacts the calculated J-factor and affects variance from halo to halo.

Figure 2.4 shows again that the effect of galaxy formation on the dark matter velocity dispersion is systematic. In every case the FIRE runs are hotter, with $\sim 3-4$ times higher velocity dispersion than their DMO counterparts at $r = 400$ pc. We have found that these halos become baryon dominated within 3-8 kpc from the center and we will discuss this later (Figure 2.23.) As discussed next, this enhancement in central velocity dispersion has a systematic effect on the dark-matter annihilation J-factors for velocity-dependent cross sections.

2.3 Astrophysical J-Factors

2.3.1 Definitions

If dark matter particle of mass m_χ is its own antiparticle with an annihilation cross section σ_A, the resulting differential particle flux produced by annihilation in a dark matter halo can be written as the integral along a line of sight ℓ from the observer (located at the solar

location in our case) in a direction $\vec{\theta}$ in the plane of the sky over pairs of dark matter particles with velocities $\vec{v}_1$ and $\vec{v}_2$:

$$\frac{d^2\Phi}{dEd\Omega} = \frac{1}{4\pi}\frac{dN}{dE}\int \mathrm{d}\ell\ \mathrm{d}^3v_1\,\mathrm{d}^3v_2 \frac{f(\vec{r},\vec{v}_1)}{m_\chi}\frac{f(\vec{r},\vec{v}_2)}{m_\chi}\frac{(\sigma_A v_{\rm rel})}{2}\ . \tag{2.1}$$

Here, $\vec{r} = \vec{r}(\ell,\vec{\theta})$ is the 3D position, which depends on the distance along the line of sight ℓ and sky location $\vec{\theta}$. The dark matter velocity distribution $f(\vec{r},\vec{v})$ is normalized such that $\int d^3v f(\vec{r},\vec{v}) = \rho(\vec{r})$, where ρ is the dark matter density at that location. The symbol $v_{\rm rel} = |\vec{v}_1 - \vec{v}_2|$ represents the relative velocity between pairs of dark matter particles. The quantity m_χ is the dark matter particle mass and dN/dE is the particle energy spectrum ultimately produced by a single annihilation.

Following [16], we parameterize the velocity-dependence of the dark matter annihilation cross section as

$$\sigma_A v_{\rm rel} = [\sigma v]_0\, Q(v_{\rm rel}), \tag{2.2}$$

where $[\sigma v]_0$ is the overall amplitude and the function $Q(v)$ gives parameters to the velocity dependence. For s-wave, p-wave, and d-wave annihilation, $Q(v) = 1$, $(v/c)^2$, and $(v/c)^4$, respectively. We can then rewrite the differential particle flux as

$$\frac{d^2\Phi}{dE\mathrm{d}\Omega} = \frac{(\sigma_A v)_0}{8\pi m_X^2}\frac{dN}{dE_\gamma}\left[\frac{dJ_Q}{d\Omega}\right]\ . \tag{2.3}$$

Here, the term in brackets absorbs all of the astrophysics inputs and defines the astrophysical "J-factor"

$$\frac{dJ_Q}{d\Omega}(\vec{\theta}) = \int \mathrm{d}\ell \int \mathrm{d}^3v_1 f(\vec{r},\vec{v}_1)\int \mathrm{d}^3v_2 f(\vec{r},\vec{v}_2)\, Q(v_{\rm rel})\,. \tag{2.4}$$

In principle, the ℓ integral above sums pairs along the line-of-sight from the observer ($\ell = 0$)

to infinity. In practice, we are focusing on J-factors arising from an individual “Milky Way" halo, and truncate our integrals at the halo's edge (see below).

It is often useful to quote the cumulative J-factor within a circular patch of sky of angular radius ψ centered on the Galactic Center. In this case, the patch defined by ψ subtends a solid angle $\Omega_\psi = 4\pi \sin^2(\psi/2)$ and we have:

$$J_Q(<\psi) = \int_0^{\Omega_\psi} \frac{dJ_Q}{d\Omega}(\vec{\theta})\, \mathrm{d}\Omega\,. \tag{2.5}$$

2.3.2 Approach

In what follows we aim to determine the astrophysical J-factors for each of our simulated halos for s-wave, p-wave, and d-wave annihilation. In doing so we approximate the dark matter distribution $f(\vec{r}, \vec{v})$ as a separable function:

$$f(\vec{r}, \vec{v}_1) = \rho(\vec{r})\, g(\vec{v}(\vec{r})), \tag{2.6}$$

with the dark matter density ρ estimated using direct particle counts in the simulation. In this estimate, we use a cubic spline smoothing kernel [66] with smoothing length set to contain the mass of the nearest 32 neighbors. [45] describes this.

For standard s-wave annihilation we have $Q(v) = 1$ and the effective J-factor (Eq. 2.4) reduces to a simple integral over the density squared:

$$\begin{aligned} \frac{dJ_s}{d\Omega}(\vec{\theta}) &= \int \mathrm{d}\ell\, \rho^2(\vec{r}) \int \mathrm{d}^3 v_1\, g_r(v_1) \int \mathrm{d}^3 v_2\, g_r(v_2) \\ &= \int \mathrm{d}\ell\, \rho^2[\ell(\vec{r})]. \end{aligned} \tag{2.7}$$

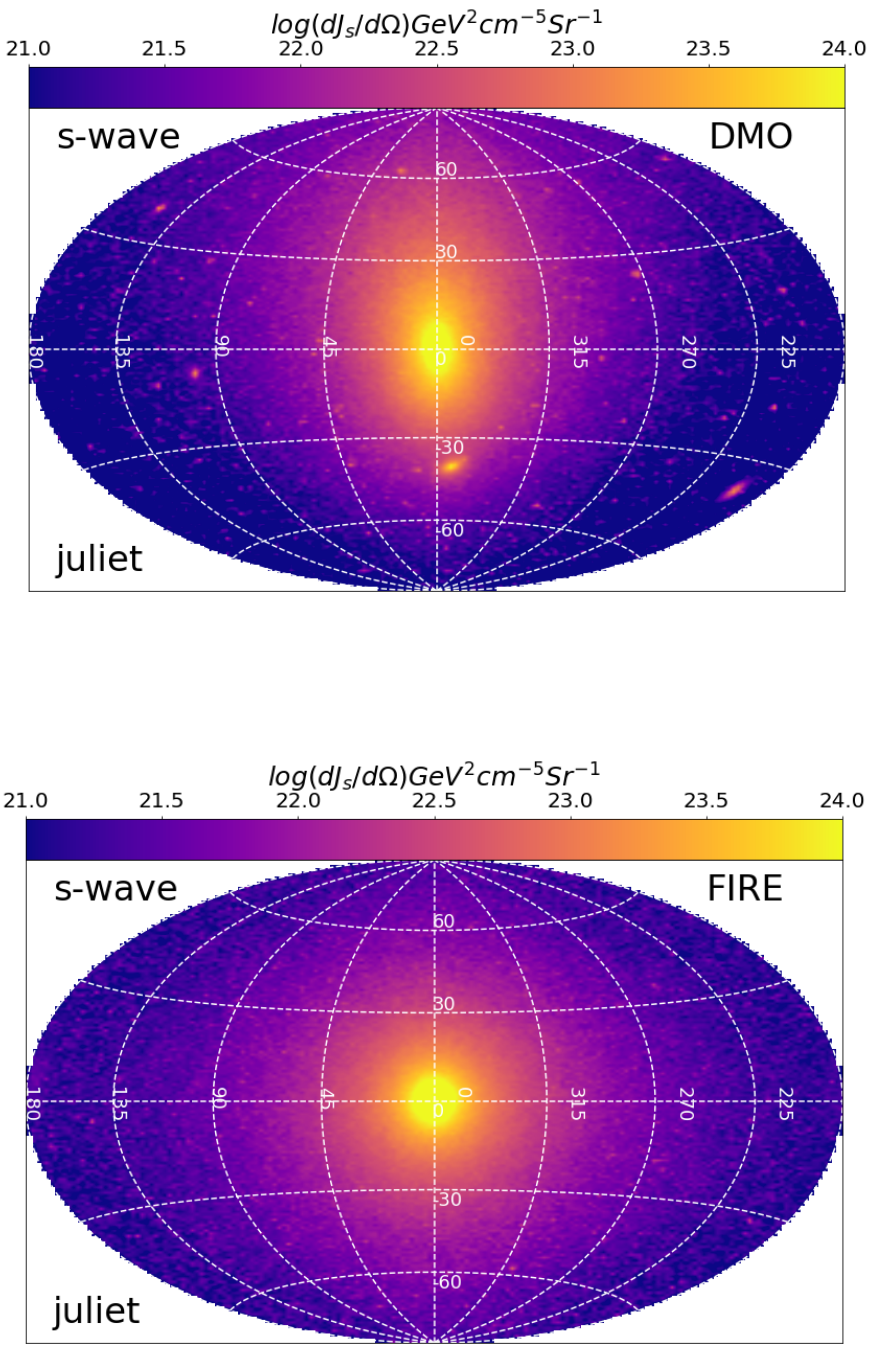

Figure 2.5: All-sky Hammer projections of J-factors ($dJ/d\Omega$) for `JulietDMO` (top) and `Juliet` (bottom) in Galactic coordinates as viewed from mock solar locations 8.3 kpc from the halo centers. Maps utilize bins of roughly 1.3 square degrees on the sky.

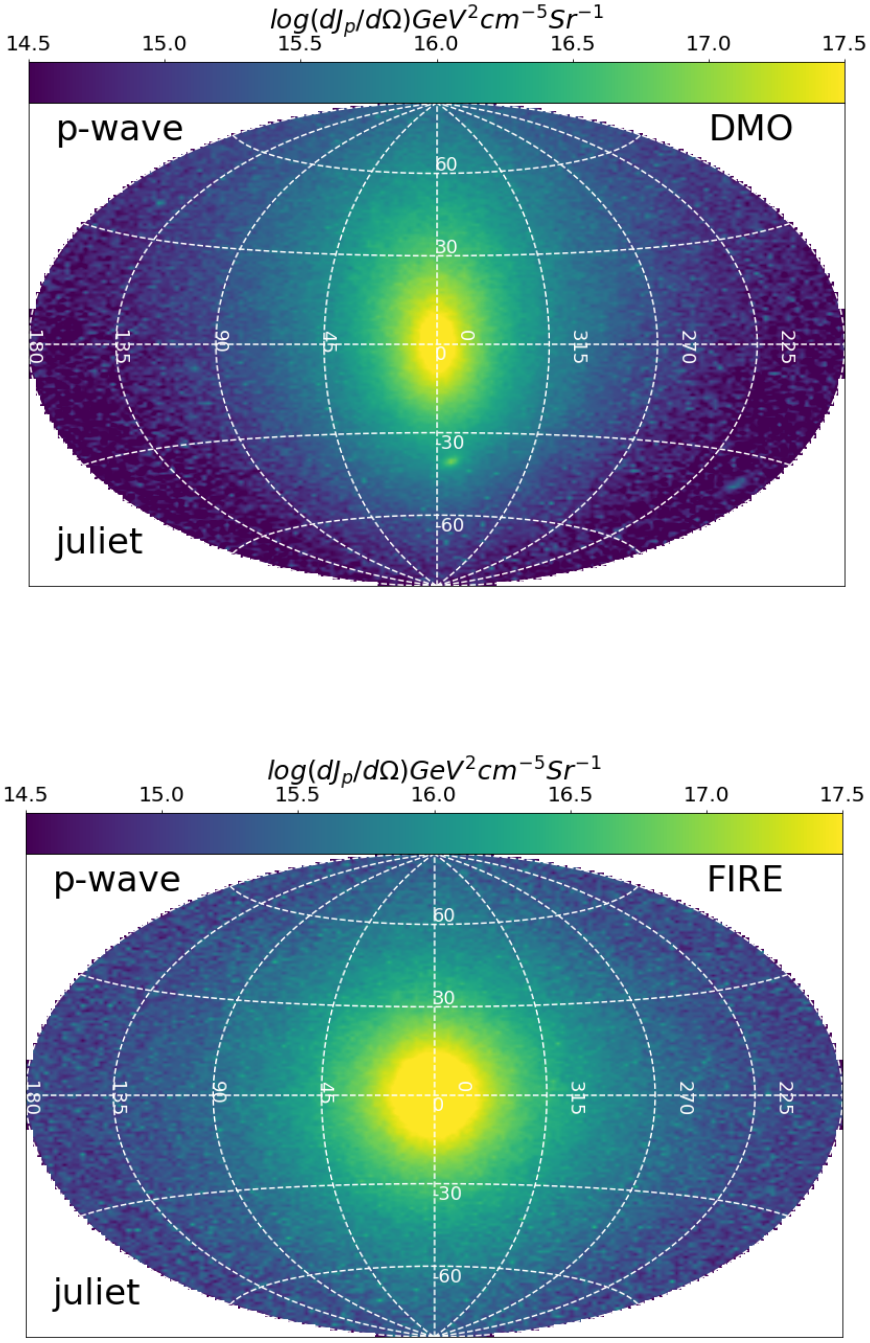

Figure 2.6: The color map in each pair of panels is fixed for each type of assumed annihilation and is logarithmic in $dJ/d\Omega$, as indicated by the bar along the top of each image. Note that FIRE runs (bottom) produce systematically rounder J-factor maps on the sky. The p-wave maps are brighter and have a larger extent, owing to the effects of galaxy formation in enhancing dark matter velocity dispersion in the center of each halo.

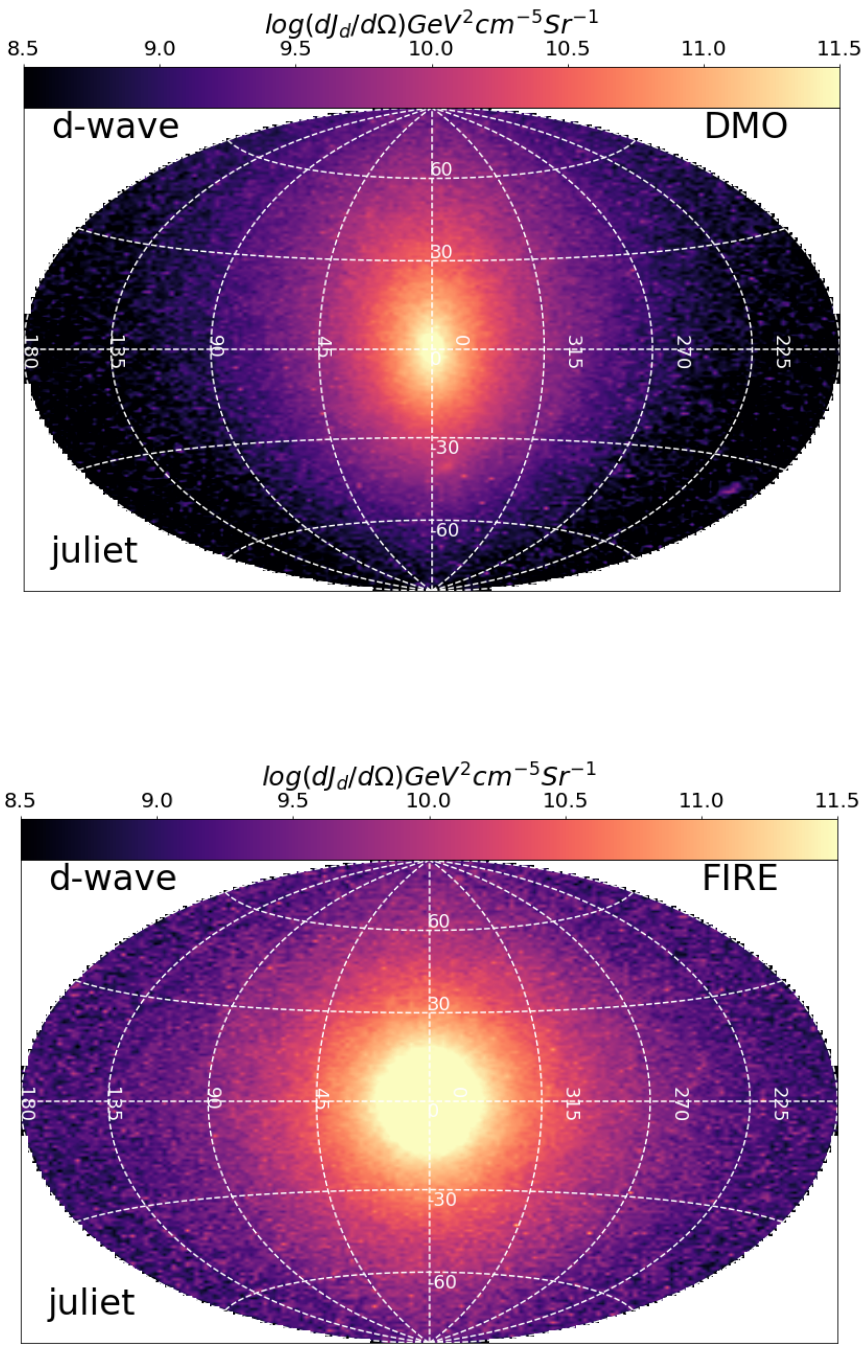

Figure 2.7: Compared to DMO (top), the d-wave maps are significantly brighter and more extended for the FIRE runs as well(bottom), having the largest difference of all, since d-wave annihilation has the largest velocity dependence.

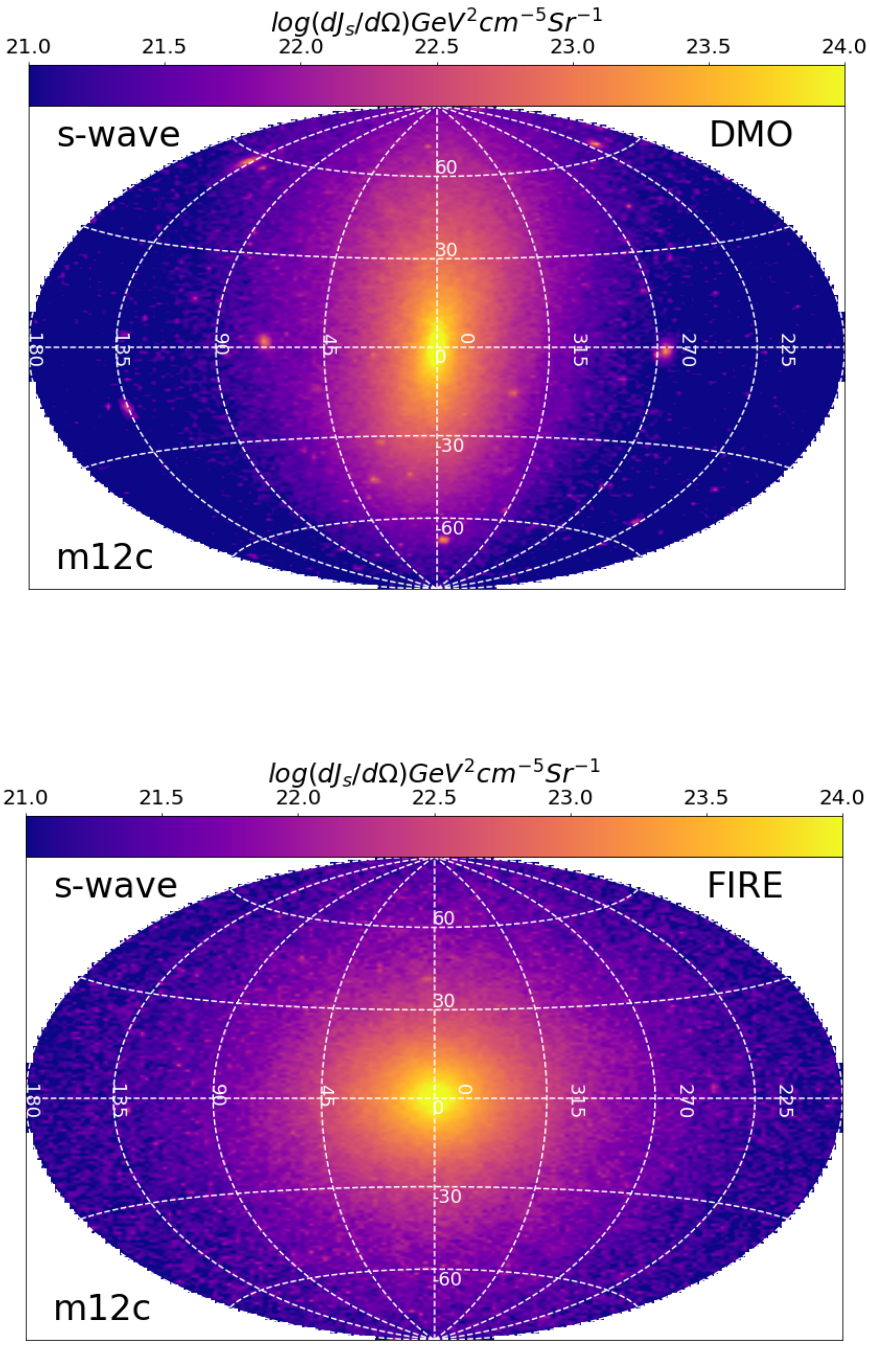

Figure 2.8: m12c s-wave J-factors. Same description as for Juliet s-wave figure.

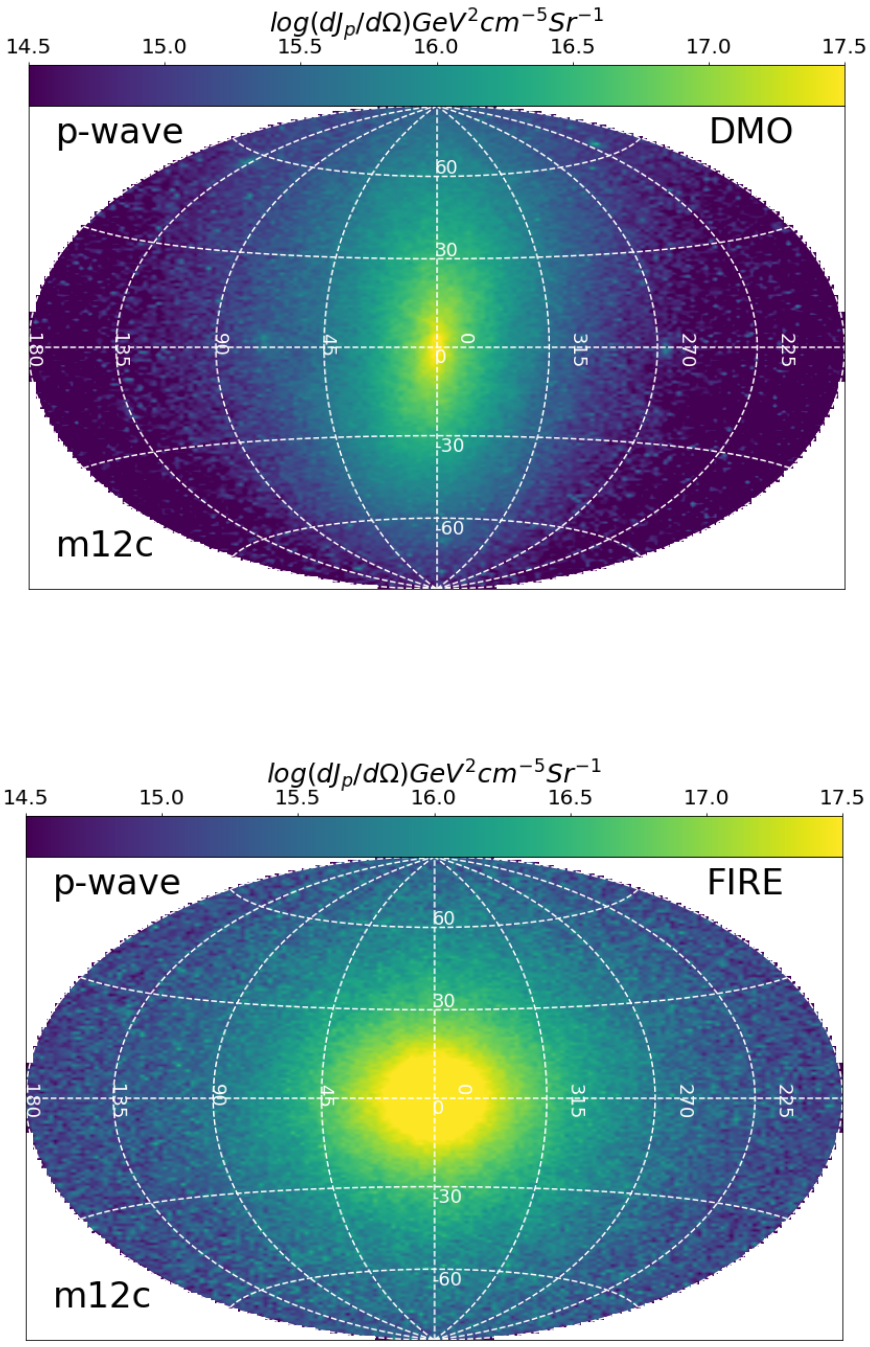

Figure 2.9: m12c p-wave J-factors. Same description as for Juliet p-wave figure

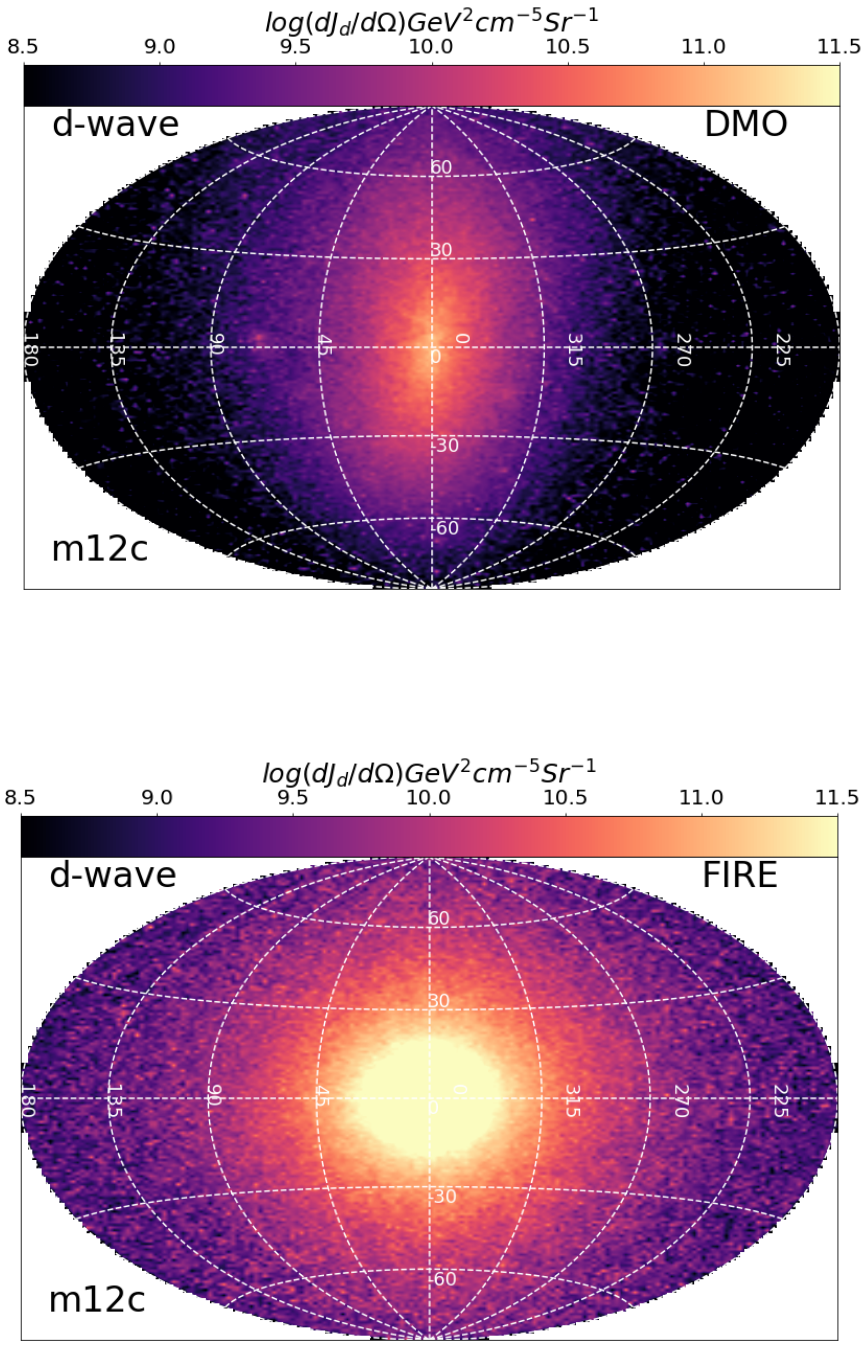

Figure 2.10: m12c d-wave J-factors. Same description as for Juliet d-wave figure

For p-wave annihilation, $Q(v) = (v/c)^2$, and Eq. 2.4 becomes

$$\begin{aligned}\frac{dJ_p}{d\Omega}(\vec{\theta}) &= \int \mathrm{d}\ell\, \rho^2(\vec{r}) \int \mathrm{d}^3 v_1\, g_r(v_1) \int \mathrm{d}^3 v_2\, g_r(v_2)\, \frac{|\vec{v_1} - \vec{v_2}|^2}{c^2} \\ &= \frac{1}{c^2} \int \mathrm{d}\ell\, \rho^2[\ell(\vec{r})]\, \mu_2(\ell(\vec{r})). \end{aligned} \tag{2.8}$$

In the second line we have used μ_2 to represent the second moment of the relative velocity at position $\vec{r}$. For d-wave annihilation, $Q(v) = (v/c)^4$, which implies

$$\begin{aligned}\frac{dJ_d}{d\Omega}(\vec{\theta}) &= \int \mathrm{d}\ell\, \rho^2(\vec{r}) \int \mathrm{d}^3 v_1\, g_r(v_1) \int \mathrm{d}^3 v_2\, g_r(v_2)\, \frac{|\vec{v_1} - \vec{v_2}|^4}{c^4} \\ &= \frac{1}{c^4} \int \mathrm{d}\ell\, \rho^2[\ell(\vec{r})]\, \mu_4(\ell(\vec{r})). \end{aligned} \tag{2.9}$$

Here μ_4 is the fourth moment of the relative velocity at position $\vec{r}$. We measure both μ_2 and μ_4 at each particle position using the nearest 32 dark matter particles. [3]

2.3.3 Geometric Setup

For each halo in our sample, we calculate J-factors as defined in Equation 2.4, integrating from a mock Solar location (setting $\ell = 0$) to the edge of the halo, which we define as a sphere of radius $r = 300$ kpc from the center of each halo in every case. While the virial radii [18] of our halos range from $300 - 335$ kpc, we fix 300 kpc as the halo boundary for consistency. Since most of the J-factor signal comes from the inner halo, changing the outer

[3] For a perfectly spherically symmetric Maxwellian distribution, we expect the cross terms to vanish such that $\langle(\vec{v_1} - \vec{v_2})^2\rangle = 2\sigma_v^2$ and $\langle(\vec{v_1} - \vec{v_2})^4\rangle = 48\sigma_v^4 \;/\; 9$, where σ_v is the local velocity dispersion. We show in Section 2.9 that direct measurement gives slightly lower estimates than would be expected from the simplified Maxwellian expectation. We then construct all-sky maps of the relevant J-factors using appropriately-weighted and smoothed projections from mock observer locations (see below).

radius by 10% has no noticeable affect on our results.

For the DMO runs, we assume that the Galactic Center corresponds to the halo center and fix the observer location to be at a distance 8.3 kpc from the halo center along the x-axis of the simulation. For FIRE runs, we position the observer in the galaxy disk plane at a radius of 8.3 kpc from the halo center. We define the disk plane to be perpendicular to the angular momentum vector of all the stars within 20 kpc of the central galaxy.

2.4 Results

2.4.1 Skymaps

Figures 2.5 and 2.8 illustrate graphically our results for two example halo pairs, `Juliet` and `m12c`, respectively for s-wave annihilation models for both DMO(top) and FIRE(bottom). These maps are thus the all-sky Hammer projections of $dJ/d\Omega$ for s-wave annihilation. Figures 2.6 and 2.9 represent the same, but this time for p-wave annihilation. Finally, figures 2.7 and 2.10 represent the d-wave J factors for the DMO (top) and FIRE (bottom) run of each halo. We are viewing the Galactic Center (middle of each image) from mock solar locations as defined in the previous section. The color bars are mapped to J-factor amplitude as indicated at the top of each image. Note that every row has the same color mapping, so that the relative difference between DMO and FIRE runs can be seen clearly for each assumed velocity dependence. The binning in these maps is 1.3 square degrees.To find the local density of the particles and the nearest neighbors for our velocity calculations, we used Firestudio [42].

The first takeaway from these images is that the FIRE runs are significantly brighter (with amplified J-factors) than the DMO runs for the p-wave and d-wave cases. This is a direct

result of the FIRE halos having enhanced dark matter velocity dispersion compared to the DMO halos (e.g. Figure 2.4). The FIRE maps are also more extended from the Galactic Center in terms of their signal, showing that they generally have a higher flux of gamma rays at higher energies than their DMO counterparts.

The s-wave J-factor maps are not as different from one another, given the modest differences in central densities for these particular halos (see Figure 2.3), though substructure is significantly reduced in the FIRE runs, as expected from the destructive effects of the central galaxy [35, 52]. Note that in all cases, including s-wave, the FIRE maps are *rounder* on the sky – this is a result of galaxy formation tending to sphericalize the dark matter distributions compared to DMO runs in halo centers [25, 12, 21, 52, 81, 77]. The fact that we expect annihilation signals to be even rounder than in the DMO case should in principle make it easier to detect or exclude dark matter annihilation in the face of astrophysical backgrounds, which are expected to track more closely the shape of the Galaxy [2]. We will not focus on quantifying this difference in shape on the sky here because it will be the subject of future work (see Chapter 3). We will instead focus on azimuthally-averaged results in what follows.

2.4.2 Differential J-factor profiles

Figure 2.11 provides a summary of J-factor results for s-wave for all of our FIRE halos (solid blue) and DMO halos (dashed black). Plotted are $dJ/d\Omega$ profiles (Equation 2.4) as a function of angle ψ with respect to the Galactic Center. Similarly, results for p-wave (Figure 2.12) and d-wave (Figure 2.13) are shown as well. As expected, the FIRE runs are generally amplified compared to DMO runs, especially for the p-wave and d-wave cases. The shapes of the profiles are also significantly different in character. While the DMO runs show a trend for J-factor profiles to be more peaked at small angle for s-wave, and to become flatter and more extended on the sky as we progress to p-wave and d-wave, the FIRE profiles are more

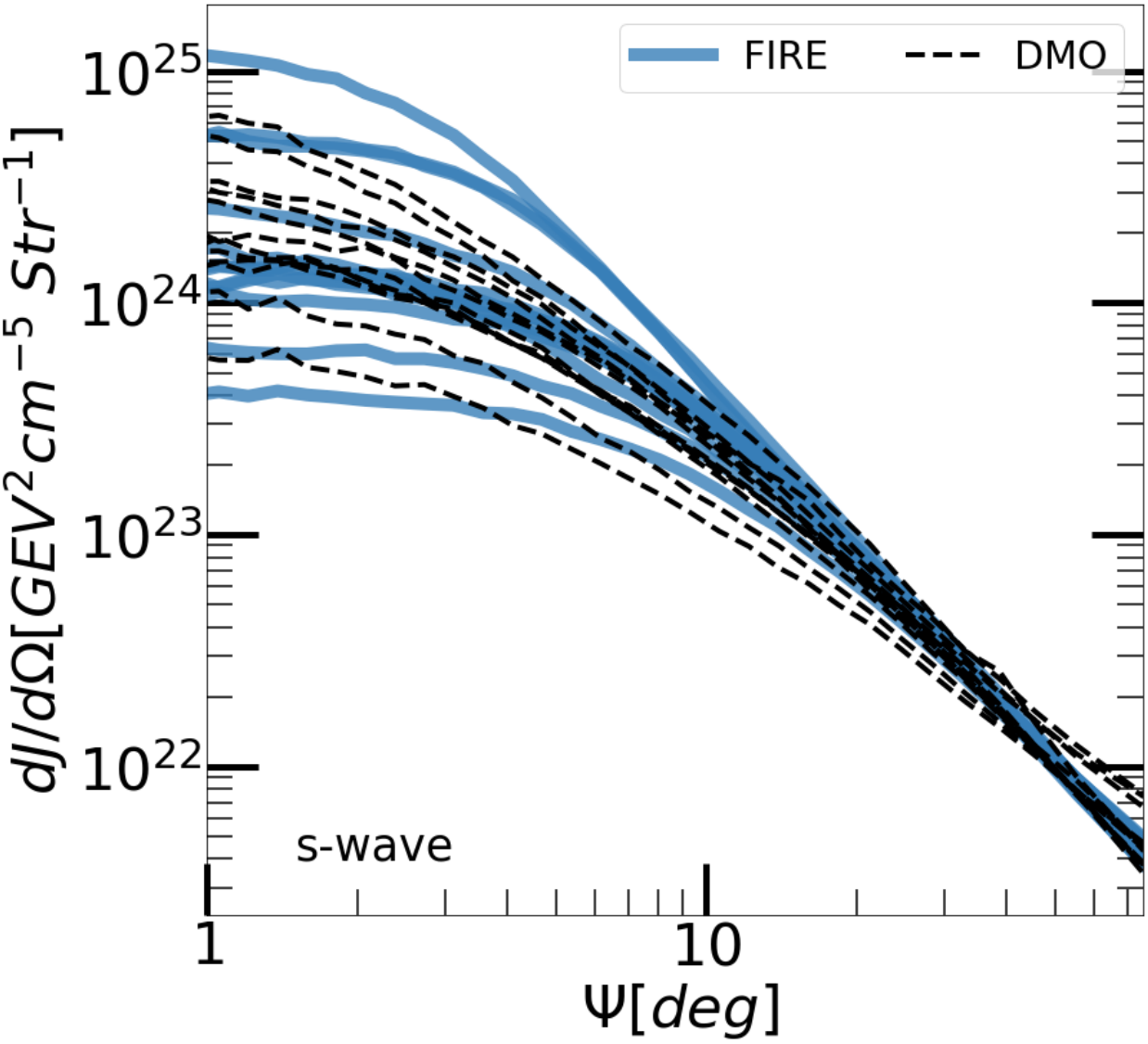

Figure 2.11: The FIRE simulation halos for s-wave are shown as solid blue lines and their DMO counterparts are shown as dashed black lines. We see that the central J-factor values are similar for FIRE and DMO cases, though the FIRE profiles are flatter at small angle, and more extended on the sky.

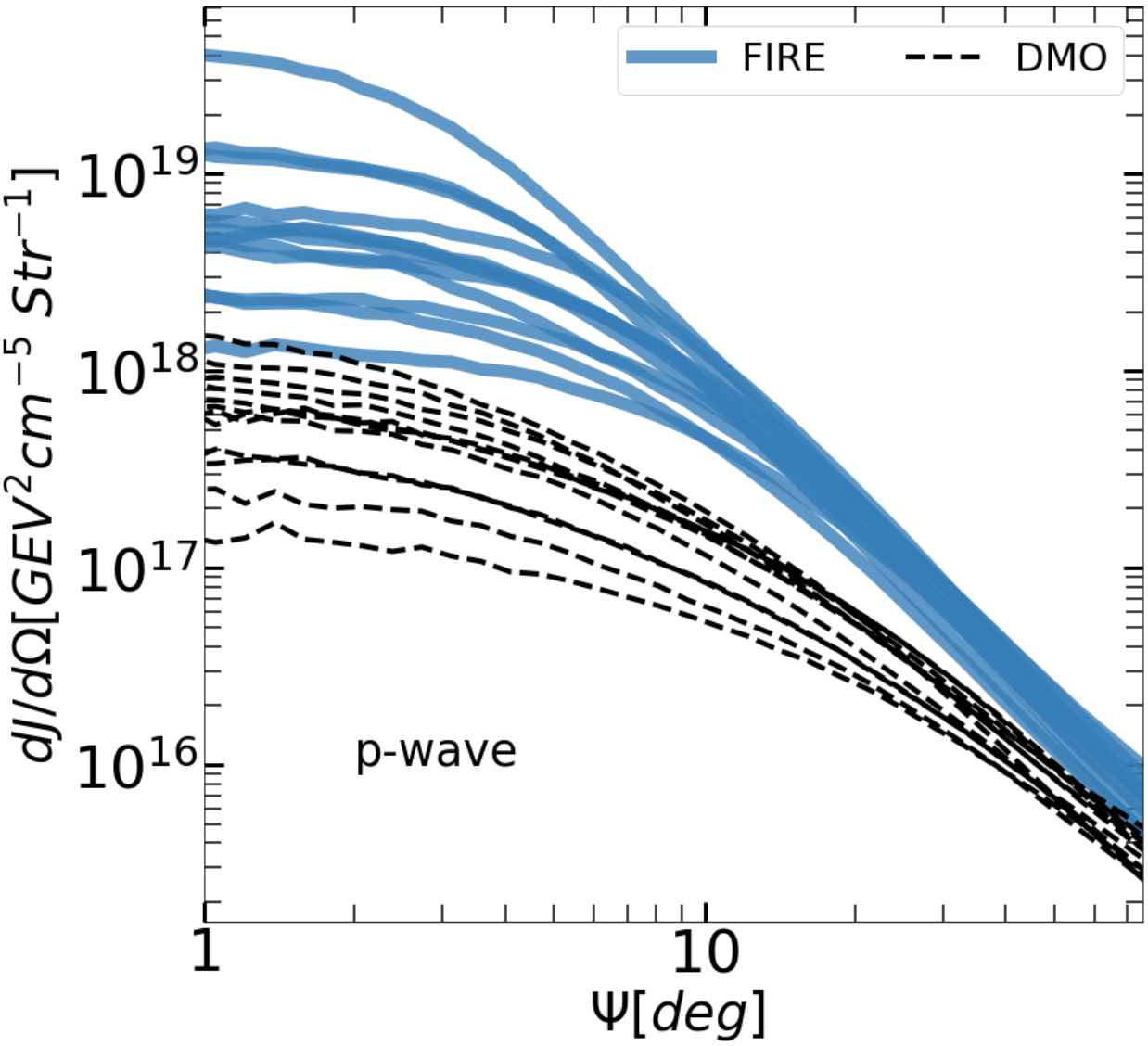

Figure 2.12: The FIRE simulation halos are shown as solid blue lines and their DMO counterparts are shown as dashed black lines. The FIRE p-wave profiles (blue) are a noticeably amplified compared to the DMO cases(black dashed). Their shapes are also significantly different – with a flatter inner profile and sharper fall-off at angles beyond 10 degrees.

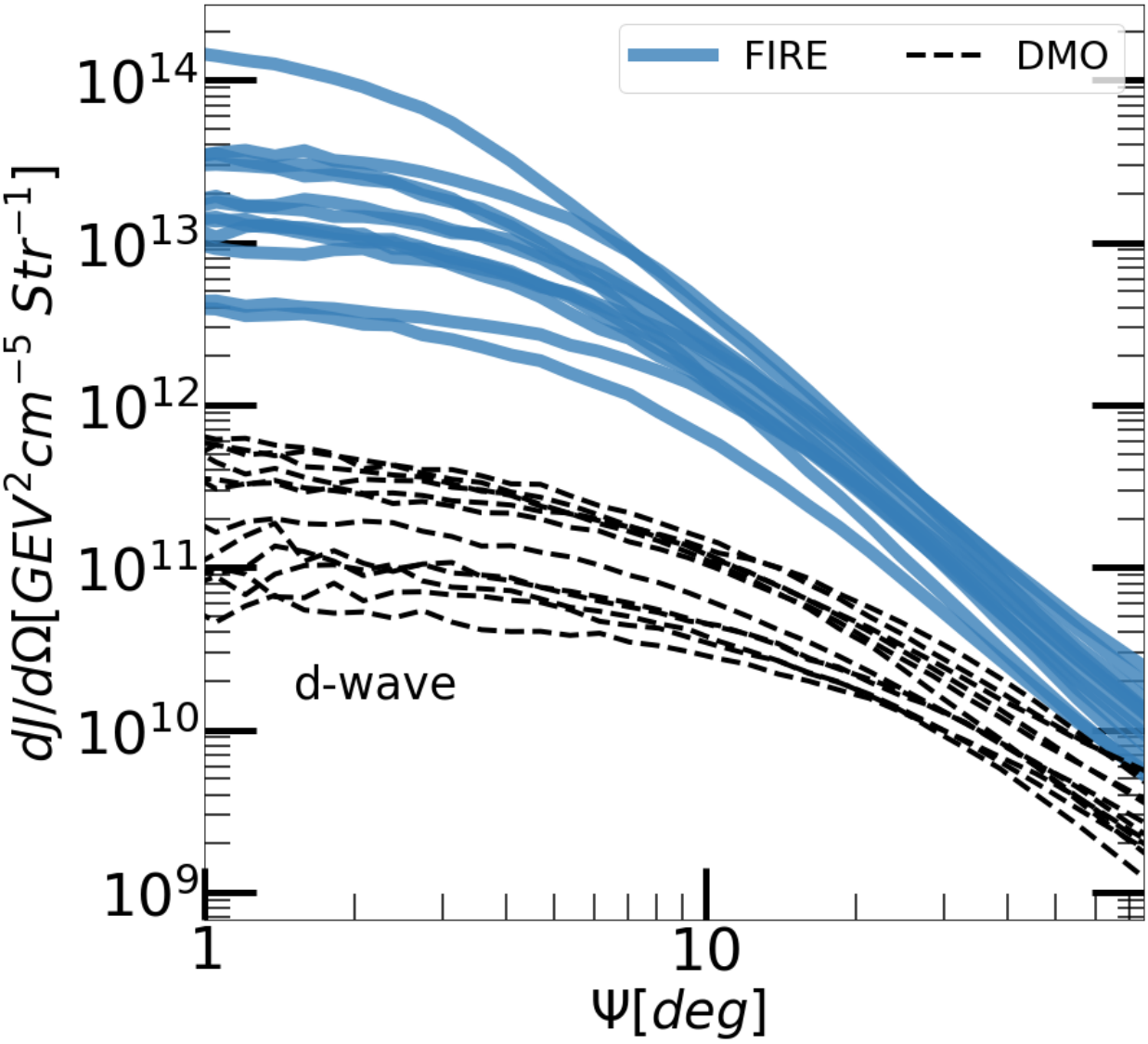

Figure 2.13: The FIRE simulation halos are shown as solid blue lines and their DMO counterparts are shown as dashed black lines.The d-wave case demonstrates the starkest difference between FIRE and DMO runs.

similar in shape. In all cases (s-wave, p-wave, and d-wave) the "emission" profile is fairly constant out to $\sim 5-10$ degrees in the FIRE runs, with a steep fall-off towards larger angles beyond that point.

2.4.3 Differential J-factor Ratios

Figure 2.14 shows, for each halo pair, the ratio of $dJ/d\Omega$ in FIRE to the DMO case as a function of angle from the Galactic Center, ψ for s wave. Each halo pair has a unique color, as indicated. For s-wave annihilation we see that the FIRE runs sometime produce higher J-factors (up to a factor of ~ 6) at small angle and sometimes give decreased J-factors (as small as ~ 0.3 of the DMO value). Because for s-wave annihilation the J-factor depends only on the density, this behavior tracks what seen for the density profiles (Figure 2.3). Sometimes feedback has produced a cored-out central density profile, leading to a lower central J-factor; sometimes baryonic contraction is more important, and this creates higher central densities and higher J-factors at small angle.

Figures 2.15 and 2.16 show that the J-factor ratios are higher, in all cases, for the FIRE runs for p-wave and d-wave annihilation. This is because the dark matter velocities are always enhanced (see Figure 2.2) by factors of $2.5-4$, which is enough to boost the p-wave and d-wave annihilation with respect to DMO runs, even in the cases where the central density is slightly smaller. Typical amplification factors are ~ 10 for p-wave and ~ 100 d-wave. In cases like `M12i` and `Romulus`, where the dark matter density is also higher in the FIRE runs, the p-wave and d-wave ratios can very large (factors of $\sim 40-60$ and $\sim 400-500$, respectively).

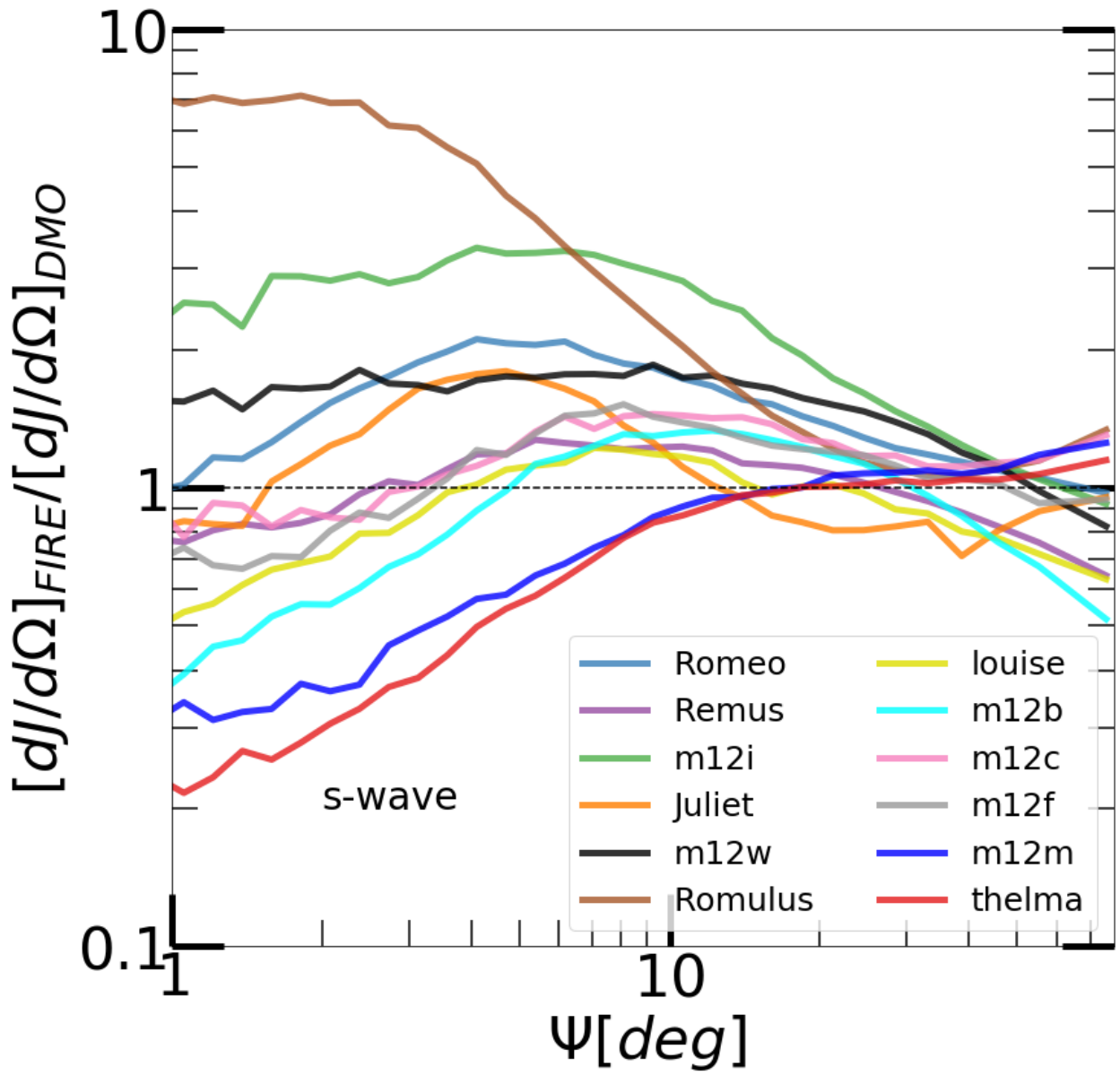

Figure 2.14: Ratio of FIRE to DMO J-factors for each halo as a function of angle ψ from the Galactic center for s-wave. Each halo pair has a unique color, as indicated. For the case of s-wave the ratio is of order unity, ranging from a factor of 3 higher to a factor of 0.3 lower at small angles.

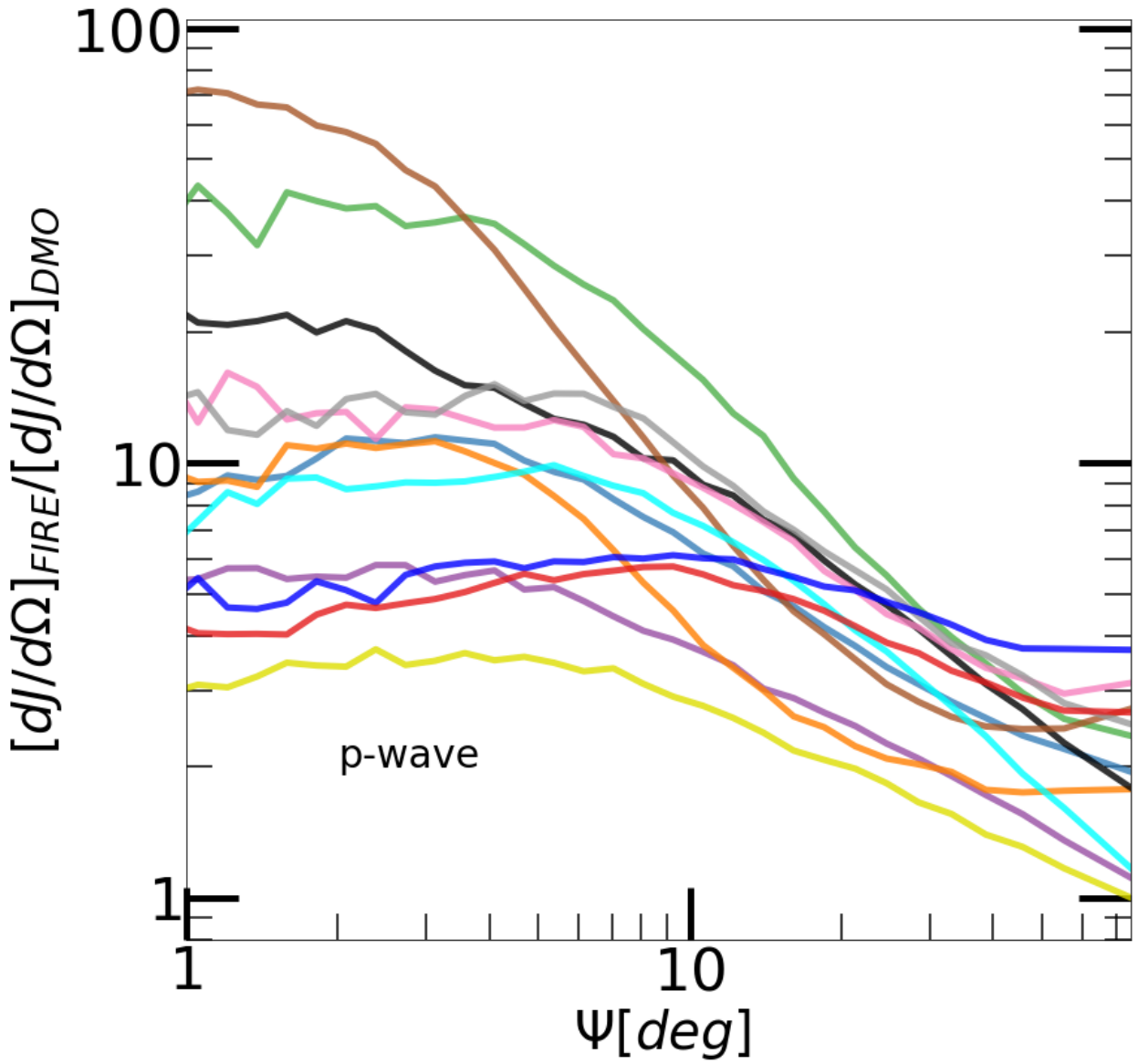

Figure 2.15: The FIRE p-wave profiles are noticeably amplified compared to the DMO cases. Their shapes are also significantly different – with a flatter inner profile and sharper fall-off at angles beyond 10 degrees.

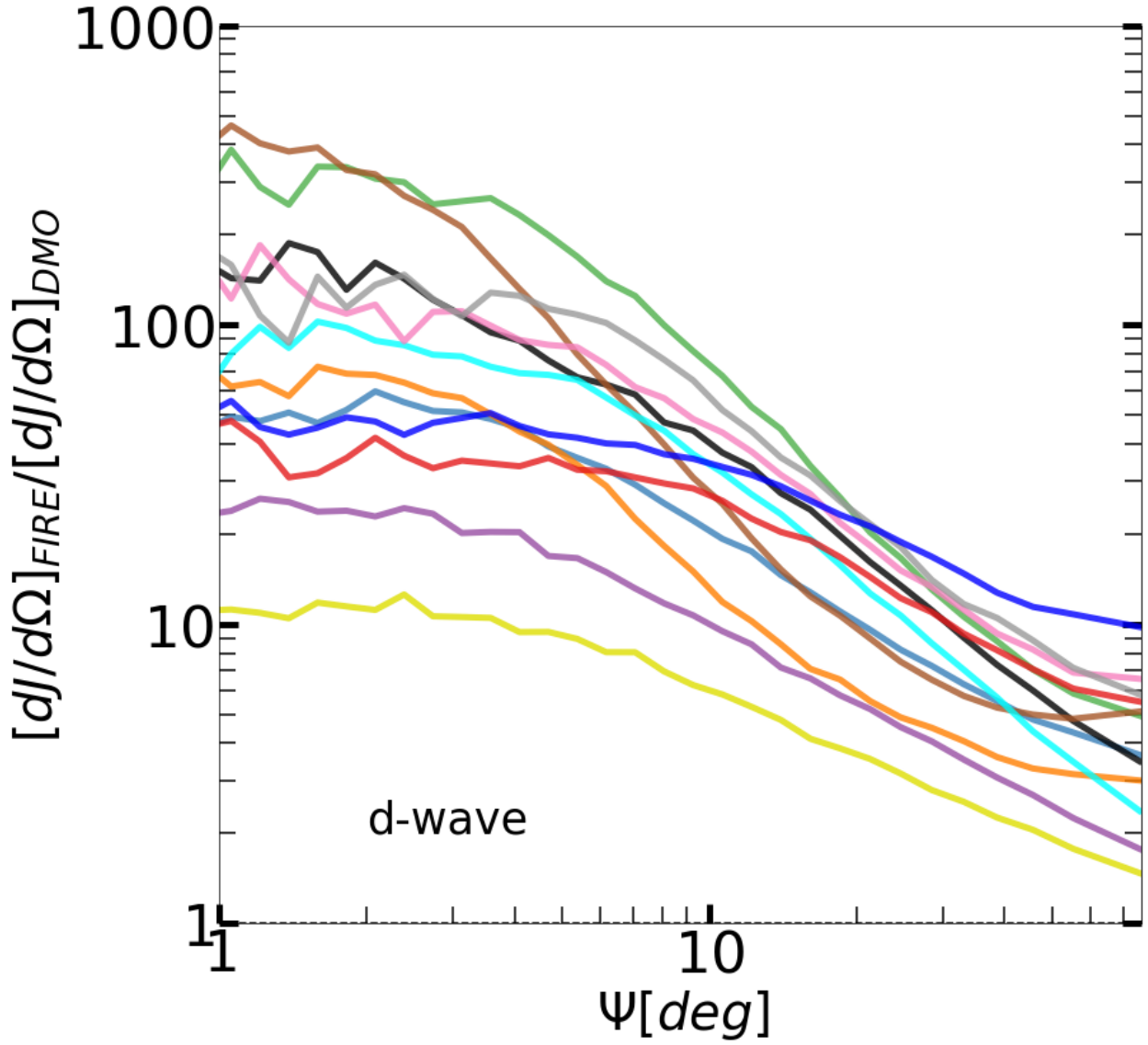

Figure 2.16: The d-wave case demonstrates the starkest difference between FIRE and DMO runs.

2.4.4 Cumulative J-factor's as a function of angle from the Galactic Center

Another way to see the difference between DMO and FIRE models is to compare the cumulative J-factors within annular angle ψ from the Galactic Center.

Figure 2.17 shows this quantity for each DMO (top) and FIRE (bottom) run. Each halo pair has a unique color, as indicated. For s-wave annihilation (Figure (2.17)), we see that the FIRE runs generally do have larger integrated J-factors within 20 degrees of the Galactic Center, even in cases (like `Thelma`) that have somewhat smaller signals within 10 degrees.

For p and d wave, Figures 2.18 and 2.19 show that the J-factor cumulative totals are higher in all cases, for the FIRE runs, though the cumulative totals are more enhanced within ~ 10 degrees owing the shape of the profile.

In the next section we explore implications of our results for dark matter indirect detection.

2.5 Implications

One of our primary results is that the DM velocities in our full galaxy formation runs are significantly higher than would be expected from DMO runs; this elevates the expected signal for fixed cross section in p-wave and d-wave models (Figures 2.18 and 2.19). In what follows we aim to provide a schematic illustration of how our results may impact attempts to constrain dark matter models with thermal abundance cross sections, especially those with velocity dependence. We use the published results of [2] in this illustrative example, and adopt a simple scaling of their published limits to provide a first-order sketch of how our results may impact future attempts to constrain s, p, and d-wave annihilation.

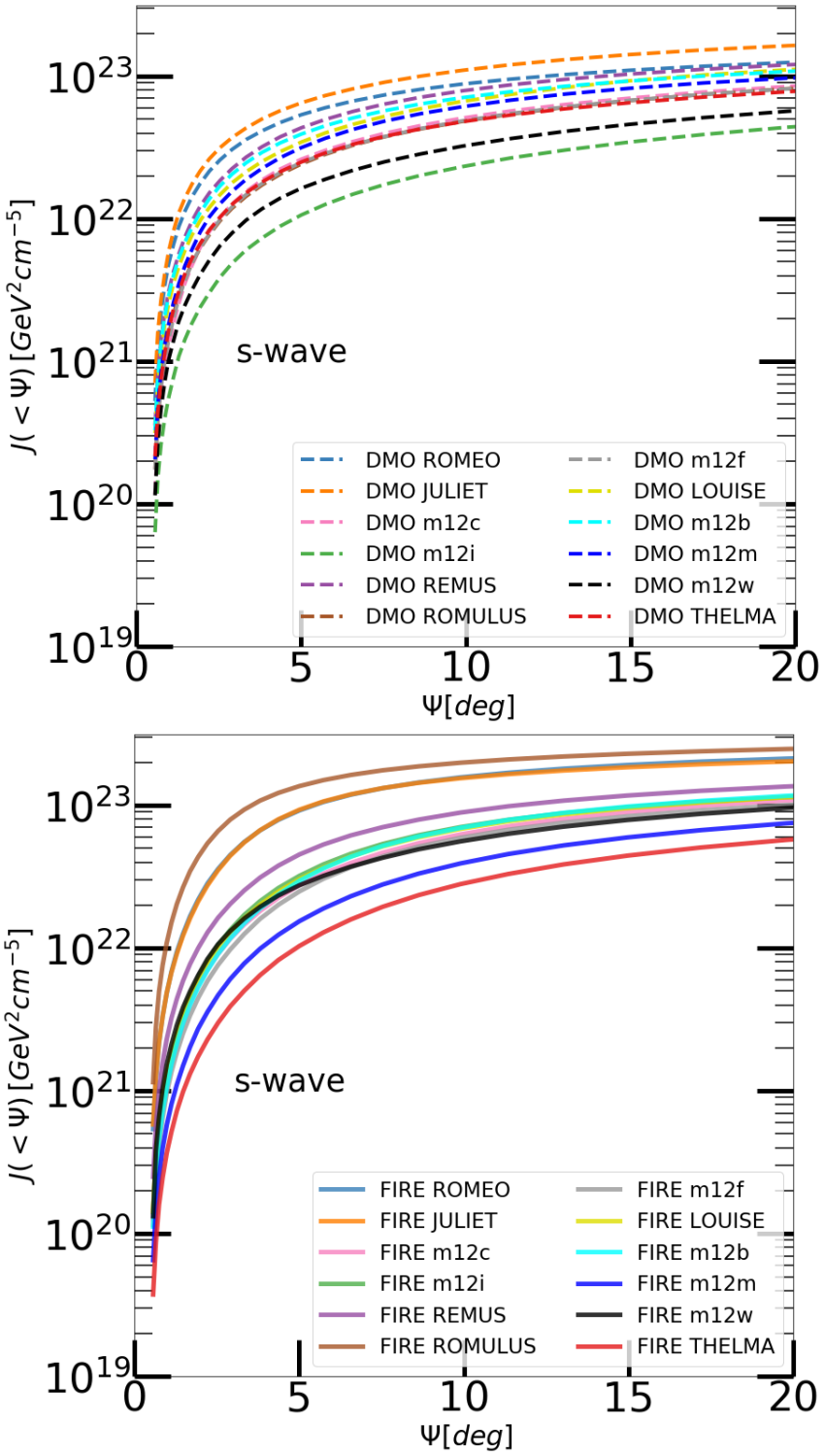

Figure 2.17: For the s-wave case, FIRE runs (bottom fig. with solid lines) have J-factors of the same order of magnitude as the DMO runs (top fig. with dashed lines.)

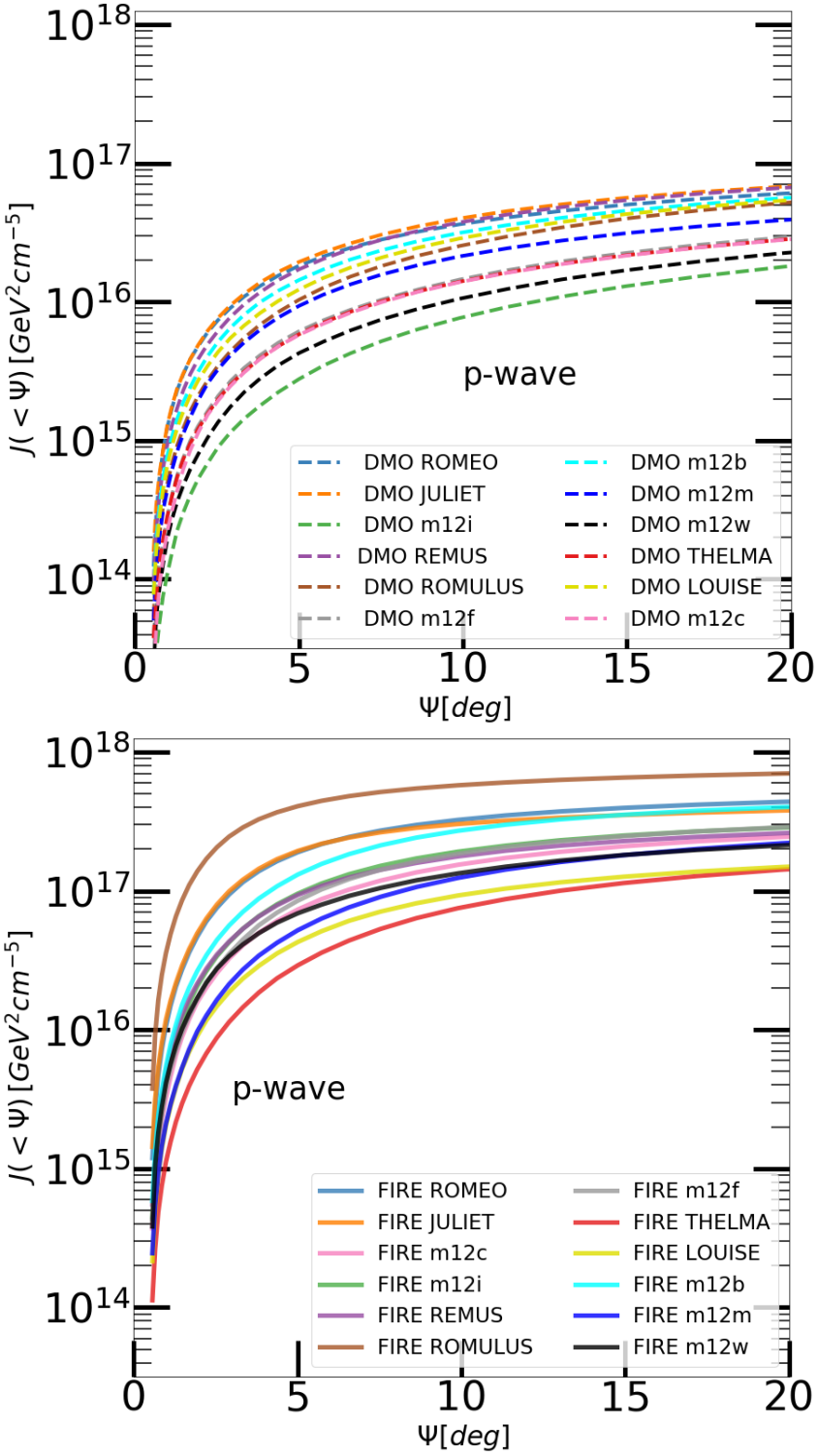

Figure 2.18: For p-wave, J-factors are considerably higher for FIRE (bottom fig. solid lines) than DMO (top fig. with dashed lines) .

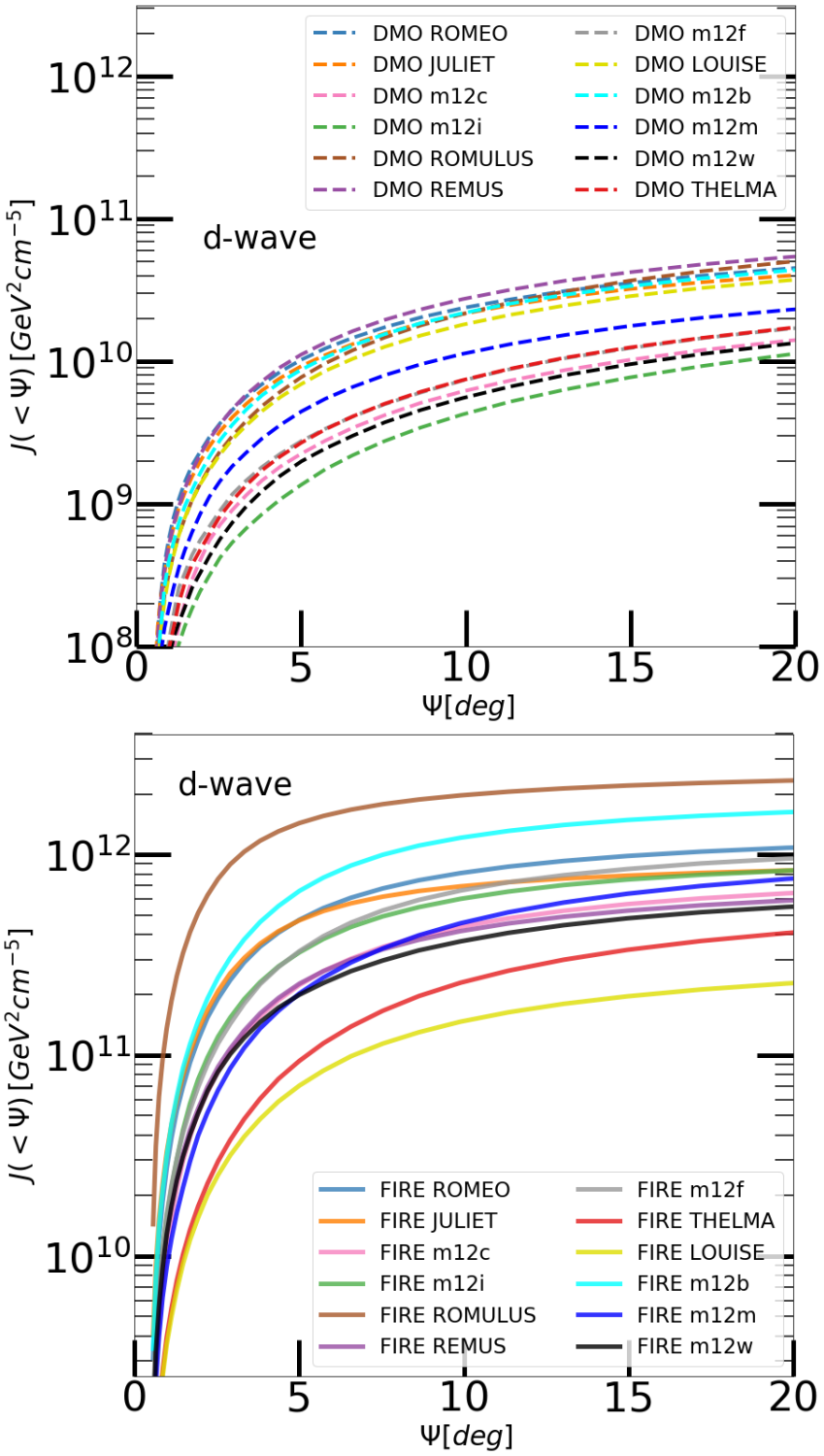

Figure 2.19: d-wave shows the largest differences between DMO and FIRE, with FIRE(bottom) being much larger.

As discussed in the introduction, the realization that the observed Galactic Center gamma-ray excess has a non-circular, boxy shape that traces the Galactic Bulge [61, 10] has allowed [2] to rule out a number of thermal-abundance WIMP models with s-wave annihilation channels for $m_\chi \lesssim 500$ GeV. Such a result motivates the exploration of p-wave (and d-wave models). There is a general expectation that velocity-suppressed p-wave and d-wave annihilation will be far from detectable in the Milky Way [47]. This is because typical DM velocities in the Galactic Center are usually thought to be $v \sim 100$ km s^{-1} (based on DMO simulations), compared values $\sim 10^3$ times higher during thermal freeze out. While, from the point of view of a model builder, such a suppression is "good" because it evades direct-detection bounds, from the point of view of an observer or experimentalist, this level of suppression is a potential nightmare: how can we detect such a signal?

The thick black lines of Figure 2.20 for both DMO(top) and FIRE(bottom) cases, reproduce the s-wave constraints published by [2]. The horizontal axis shows the WIMP mass and vertical axis is the velocity-averaged cross section. In our generalized language, the vertical axis specifically corresponds to the normalization $[\sigma v]_0$, defined by $\langle \sigma v \rangle = [\sigma v]_0 Q(v_{\rm rel})$ in Equation 2.10, where $Q(v) = 1$ is the s-wave case. Cross sections above the black line are excluded. In deriving this constraint, they assumed a $b\bar{b}$ annihilation channel and a plausible range of Milky Way dark matter profiles (their "NFW" case) as expected from DMO simulations. The dashed line shows the required cross section to produce the correct thermal abundance of dark matter observed [83].

The blue lines in Figure 2.20 provide schematic estimates for how the [2] limit would shift for s-) annihilation for halos that match our simulation results. Here we have made the simplistic assumption that limit will scale in direct proportion to the integrated J-factor within 10° of the Galactic Center. The range of NFW profiles considered in [2] have central densities quite similar to our own `M12wDMO` case, and we use this to set the reference J-factor for the constraint: $J_s(< 10^\circ) \equiv J_{\rm ref} = 1.7 \times 10^{22}$ GeV^2 cm^{-3}. Note that this reference J$_s$-factor is

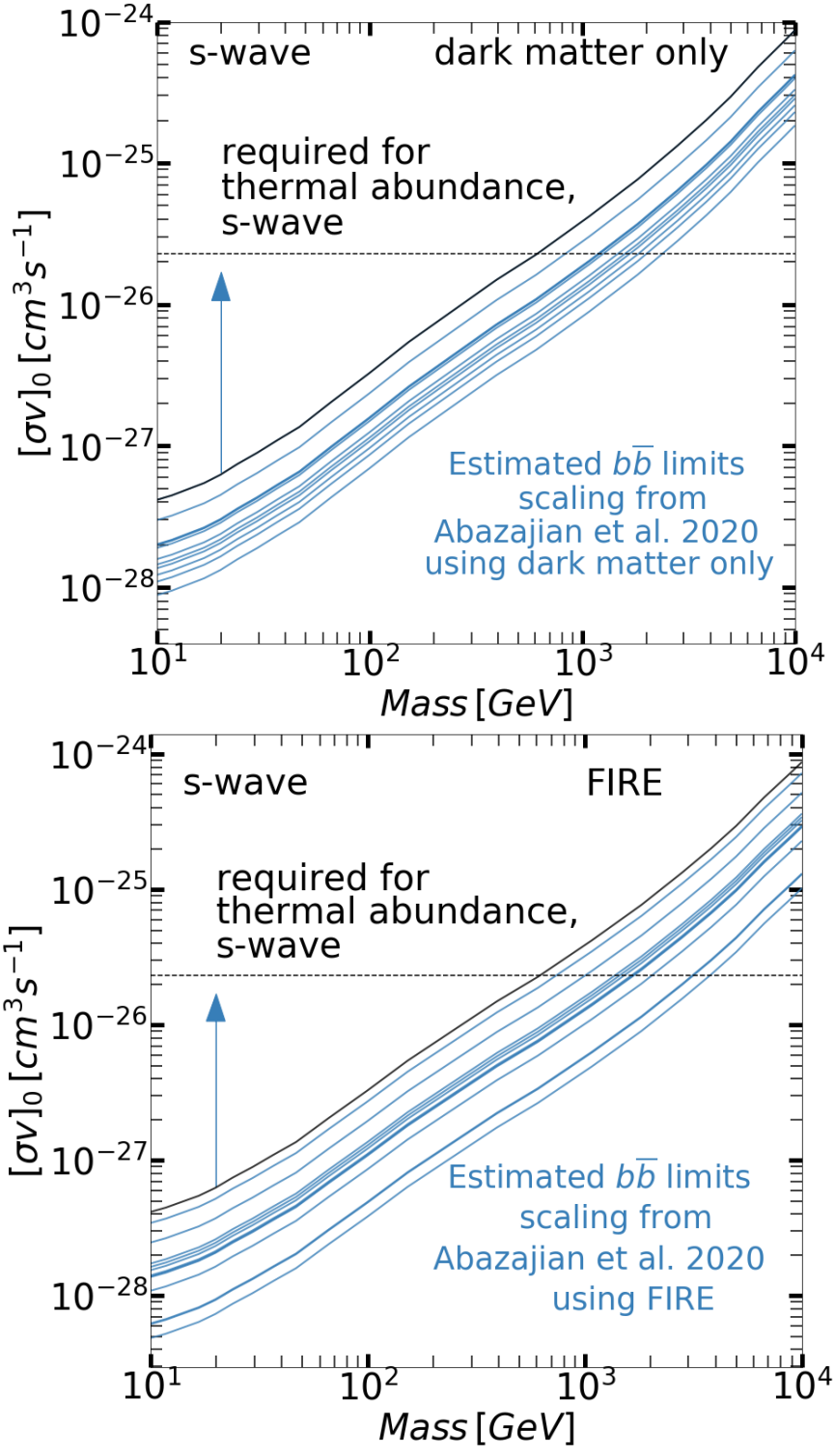

Figure 2.20: annihilation based on the relative J-factors (blue) from each of our DMO (top) and FIRE runs (bottom). The dotted lines show the $[\sigma v]_0$ required for thermal dark matter to match the observed abundance.

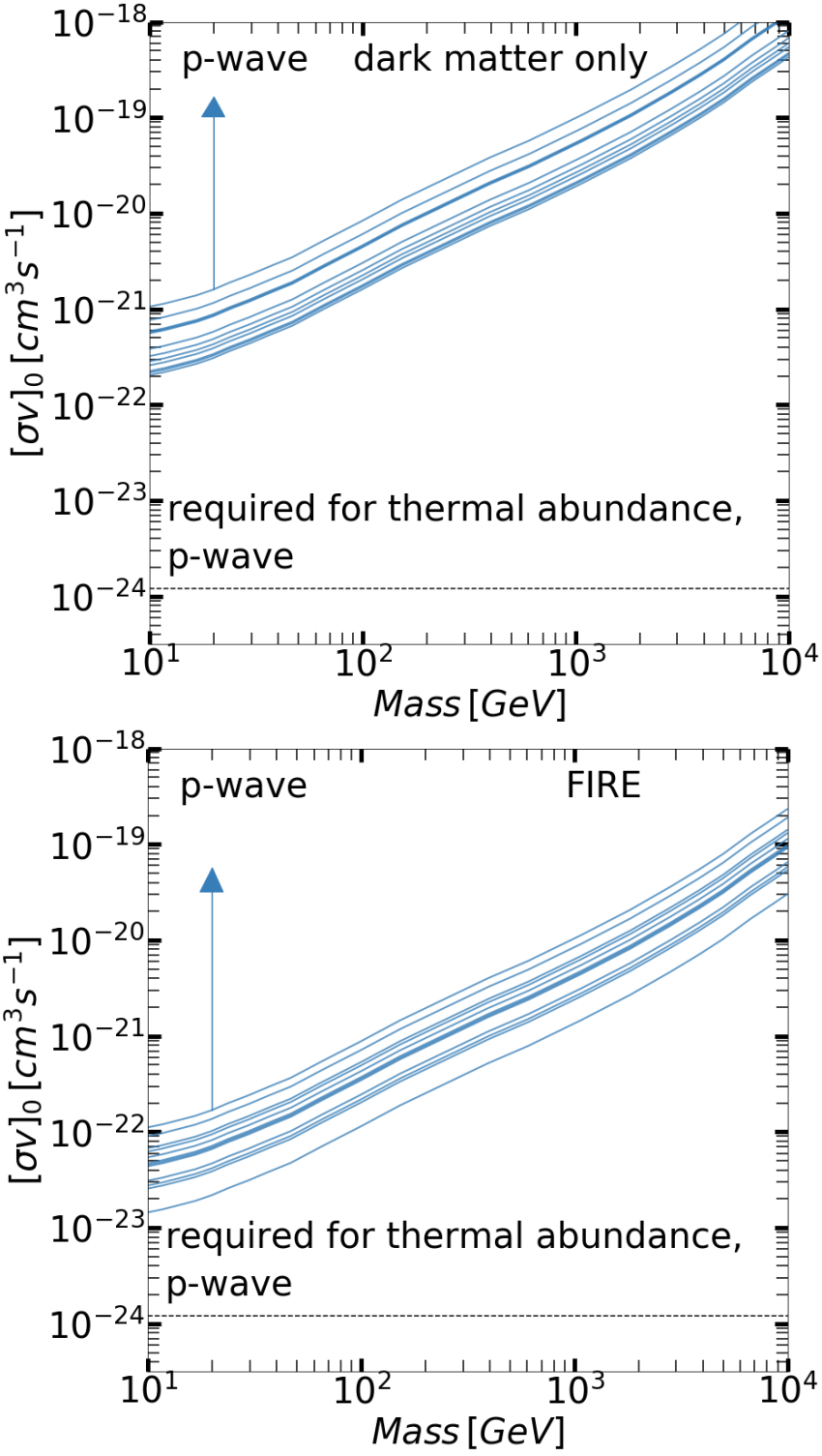

Figure 2.21: Schematic illustration of how the cross section versus particle mass constraints from [2](black solid lines, upper panels) would shift for p-wave. FIRE results suggest that current constraints for p-wave are much closer to the thermal cross section than would have been expected from DMO halos, potentially within a factor of ~ 10 for 10 GeV WIMPS.

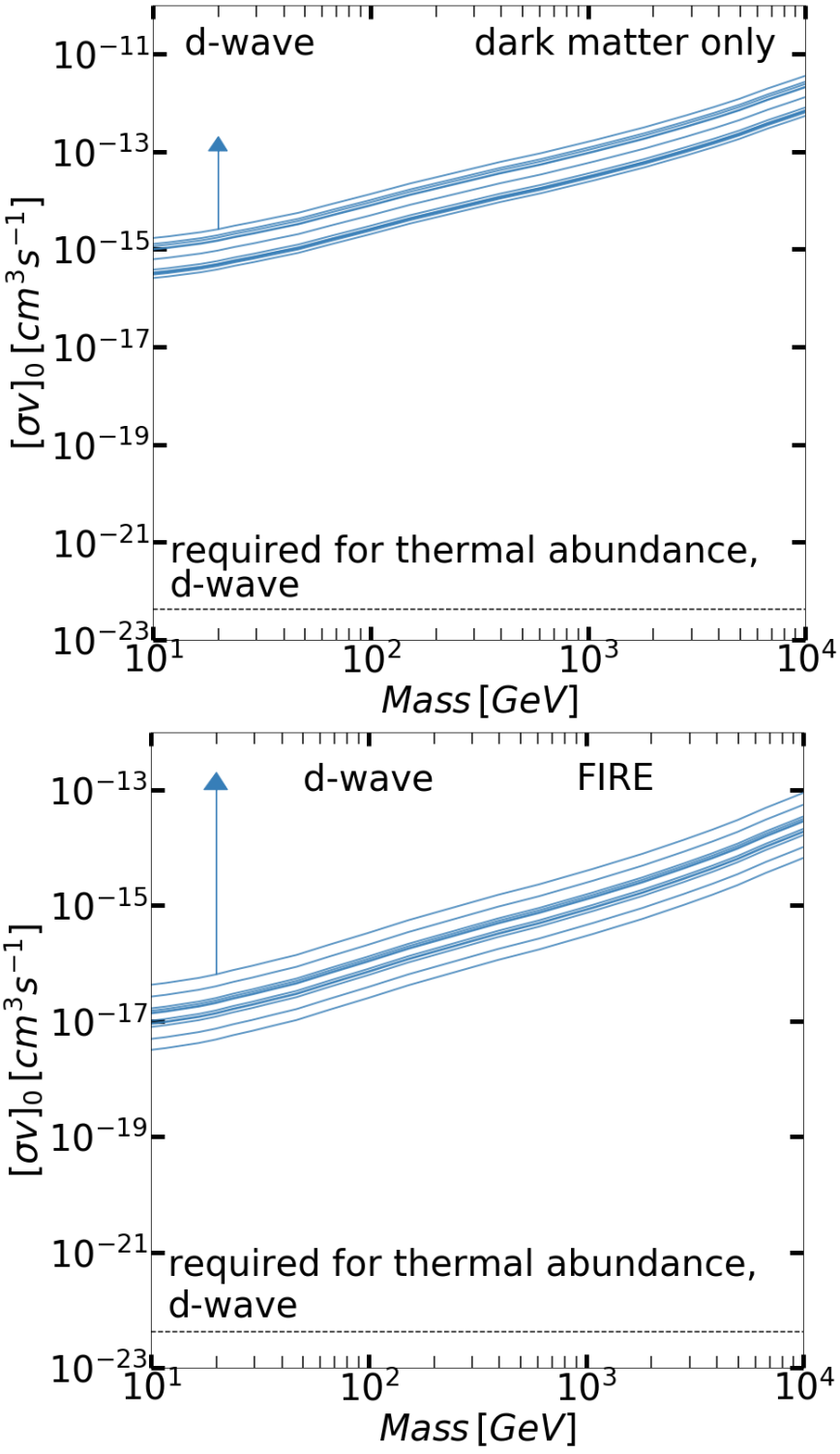

Figure 2.22: Schematic illustration of how the cross section versus particle mass constraints from [2] (black solid lines, upper panels) would shift for d-wave annihilation based on the relative J-factors (blue) from each of our DMO (top) and FIRE runs (bottom). The region above the lines is ruled out. This suggests that the cross section would be difficult to measure experimentally if it has a d-wave nature.

at the lower range of those from our DMO halos (See Table 2.1).

This is mainly due to the fact that while we normalized each halo to a local, solar dark matter density of 0.38 GeV cm^{-3}, they assumed a median normalization of 0.28 GeV cm^{-3} at the solar radius. Some of our DMO halos also deviate somewhat from a strict NFW shape, effectively making them slightly denser at ~ 1 kpc than that shape would predict for a fixed solar normalization [58].

Each blue line is a scaled version of the black line. Specifically, for each halo in our suite, we determine the ratio of the reference J-factor from Abazajian et al. to the measured J-factor for s, p, and d-wave cases: $J_{\rm ref}/J_q(< 10^\circ)$ (for $q =$ s, p, and d), and multiply the Abazajian limit by that ratio to estimate the implied limit.

Thus, Figure 2.20 shows how the implied limit scales for each of our DMO runs (top) and FIRE runs (bottom) in the s-wave case. As mentioned above, even in the DMO case, our halos tend to have larger J-factors than the halos used in [2] because of our chosen local-density normalization. The spread in lines comes about because of the halo-to-halo scatter. Interestingly, for the FIRE cases, which we regard as more realistic, the limit lies above all lines, though is within $\sim 25\%$ of the upper envelope. One way to interpret this is that the Abazajian limit is conservative in comparison to our expectations, but not exceedingly so, especially considering the sensitivity to local dark matter density normalization. In this sense, our results are unlikely to affect current constraints for the s-wave cross section significantly.

Next, Figure 2.21 shows the implied constraints for the case of p-wave annihilation, with DMO halos on the top and FIRE halos on the bottom. The dotted line shows the required cross section normalization for the thermal abundance in the p-wave annihilation case. The value is about 50 times higher than the s-wave thermal abundance normalization to make up for the fact that the total cross section is suppressed by a factor $Q = (v/c)^2$ with $v/c \sim 0.15$

during freeze-out. We work out the thermal abundance normalization explicitly for p-wave and d-wave dark matter in Section 2.7.

Note that the scaled limits in the DMO p-wave panel are more than two orders of magnitude above the thermal cross section, which would suggest indirect detection for such a model is unlikely. The bottom half of Figure 2.21 unitizes what we believe to be more realistic p-wave J-factors from our FIRE runs. The blue lines in this case suggest that a much more powerful constraint is possible for p-wave annihilation than would have been expected from DMO halos alone. In particular, we see that for low-mass WIMPS, we may be within a factor of $\sim 10 - 20$ of detecting a p-wave annihilation signal if the Milky Way resembles halos like `Romulus`, `Juliet`, and `Romeo`, which have among our highest p-wave J-factors.

Finally, Figure 2.22 shows the implied constraints for the case of d-wave annihilation. The required cross section normalization for the thermal abundance (dotted line) in the d-wave annihilation case is ~ 2000 times higher than the s-wave thermal abundance normalization (Section 2.7), though it is still orders of magnitude below any of the scaled constraints. Inferred constraints from the DMO halos (top) are five to six orders of magnitude above the thermal abundance normalization. For the FIRE cases (bottom), the situation is slightly better (roughly four orders of magnitude) though still far out of reach.

Of course, realistic constraints will require a careful analysis of Fermi-LAT Galactic Center observations, including templates for the stellar galactic and nuclear bulges, variations in the Galactic diffuse emission models, and a careful consideration of the shape of p-wave J-factor models of the kind shown in Figures 2.6 and 2.9, which tend to be even less boxy in the hydrodynamic runs than would be expected in DMO. Based on the rough estimates presented here, such an analysis is certainly warranted, and serves as further motivation for the analysis we explore in Chapter 3.

2.6 Comparison to previous work

As discussed in the introduction, [15] have presented an analysis similar to ours, comparing velocity-dependent J-factors in both DMO and hydrodynamic simulations. In this short section we compare our results to theirs. Importantly, we are in general agreement on the key result: both of us find that the (more realistic) hydrodynamic simulations predict higher central dark matter particle velocities towards the Galactic center, and this enhances J-factors for p- and d-wave annihilation compared to DMO simulations.

For a more specific comparison, we must take into account three key differences in our efforts. First, their work relies on lower-resolution simulations from the APOSTLE and Auriga suites. This means that they can only make predictions to within 10 (APOSTLE) and 7 (Auriga) degrees, compared to our 2.75 degree resolution. For this reason, we will make comparisons at 10 degrees in the discussion that follows. However, it is important to note that based on our results, this higher resolution is very critical to the question of the origin of the galactic center excess, as the galactic central region can vastly enhance the velocities of dark matter particles, and yet the majority of this enhancement occurs in the inner most approximately 7 degrees (see Figures 2.15 , 2.16 , as well as 2.18 and 2.19), showing that the higher resolution of our simulations gives many advantages by giving us the ability to detect these enhancements in signal due to velocity dispersion at small radii.

A second difference in our analysis is that we have re-scaled all of our simulations to have the same local dark matter density at mock solar locations, and have chosen a value that matches observational constraints for the Milky Way. [15] present J-factors based on raw simulation results, which will naturally scale as the local density squared by definition. A third difference is that [15] assume their halos are spherically symmetric in characterizing velocity moments, while we use direct particle counts to estimate the local density and velocity moments. This allows us to place the observer in the plane of the galactic disk

in constructing emission maps and also allows us explore how galaxy formation affects the shape of expected emission on the sky (we find it makes it much more round than naively would be expected).

The s-wave differential J-factor predictions for the DMO runs in [15] are roughly ~ 4 times lower at 10 degrees than those shown in Figure 2.11 for our DMO halos. This stems from the fact that their dark matter halos are less dense by a factor of ~ 2 at the solar location than our chosen normalization. Their hydrodynamic runs produce similar s-wave J-factors to our FIRE runs at 10 degrees ($\sim 50\%$ lower in the median). This is because their halos have become more dense in the center as a result of galaxy formation, bringing them closer, though still slightly below, the normalization we have chosen. Note that, like [15], we also find that galaxy formation usually makes halos slightly denser, as can be seen in our un-normalized profiles shown in Figure 2.1. Their DMO J-factors for p-wave and d-wave models are also consistent with ours modulo the density normalization factor.

Among the most important results in both of our papers is the systematic enhancement in p- and d-wave J-factors in hydrodynamic simulations compared to DMO cases. While [15] do not show ratios for each halo individually, they generally find that their DMO halos have p-wave J-factors at 10 degrees that are ~ 5 times lower than their full-physics runs at the same angular scale. This is close to the typical ratio we present in Figure 2.15 at 10 degrees. Similarly, for d-wave, their galaxy formation simulations have larger J-factors by ~ 30, and this is consistent with our typical ratio at 10 degrees as well , 2.16.

As mentioned above, a key advance in the present research is in our ability to push predictions towards the inner few degrees of the Galactic center, which is an important region for the gamma ray excesses seen in the Milky Way [51]. In these inner regions, we find that our FIRE halos show enhancements by factors as high as ~ 50 (p-wave) and ~ 300 (d-wave) – both of which are ~ 10 times higher, (see inner regions of (Figures 2.15) and 2.16 than the amplification seen at 10 degrees in both [15] and our analysis. Thus, our resolution at small

angles and smaller radii from the galactic center is a crucial and important gain.

2.7 Thermal cross section for velocity-dependent annihilation

In this subsection we provide an estimate for the required thermal cross section to match the observed dark matter abundance for models with a velocity-dependent annihilation cross section. We are assuming that

$$\langle \sigma v \rangle = [\sigma v]_0 Q(v_{\rm rel}) \tag{2.10}$$

where $[\sigma v]_0$ is a normalization constant and $Q(v) = 1$, v^2/c^2, and v^4/c^4, for s, p, and d-wave annihilation, respectively. For the standard s-wave case ($Q = 1$), the normalization required for thermal abundance was worked out carefully by [83], who find

$$[\sigma v]_0^{T\,s} \simeq 2.3 \times 10^{-26} {\rm cm}^3\,{\rm s}^{-1} \tag{2.11}$$

for WIMP masses above $\sim$ 10 GeV [83]. Our goal here is to determine how the required normalization changes for p-wave and d-wave.

We will follow the textbook treatment of WIMP freeze-out [54, 29, 65, 59], with the standard assumption that WIMPs are their own anti-particle and initially in thermal equilibrium with Standard Model particles in the early universe with photon temperature T. In this case the dark matter number density n can be tracked using a simplified version of the Boltzmann equation

$$\frac{dn}{dt} + 3H(t)n = \langle \sigma v \rangle (n_{eq}^2 - n^2), \tag{2.12}$$

where $H(t)$ is the Hubble parameter. Here, n_{eq} is the equilibrium number density in physical coordinates [54], which scales with the expansion factor a as $n_{eq} \propto T^3 \propto a^{-3}$ for relativistic species and becomes thermally suppressed for non-relativistic species $\propto e^{-m/T}$, where m is the dark matter particle mass. It is useful to rewrite this equation in terms of a new variable $Y \equiv n/T^3$, which scales out the expansion of the universe and eliminates the $3H(t)$ term on the left-hand side of Eq. 2.12:

$$\frac{dY}{dt} = T^3\langle\sigma v\rangle(Y_{eq}^2 - Y^2) \longrightarrow \frac{dY}{dx} = \frac{\lambda(x)}{x^2}(Y_{eq}^2 - Y^2), \tag{2.13}$$

where $Y_{eq} \equiv n_{eq}/T^3$ and the arrow points to an equivalent equation that uses a new time variable $x = m/T$. The variable $\lambda(x) \equiv m^3\langle\sigma v\rangle/H(m)$, where $H(m)$ in the denominator is the Hubble parameter evaluated at the time when the temperature $T = m$. In the standard (s-wave) treatment, λ is a constant. More generally $\lambda(x) \propto [\sigma v]_0\, x^{-n}$ with $n = 0$, 1, and 2 for s-wave, p-wave, and d-wave, respectively.

While there is no analytic solution to Equation 2.13, we can estimate how the ultimate abundance will scale with input parameters. At early times ($x \ll 1$), the coefficient λ/x^2 will be very large and Y will track the equilibrium abundance. As time progresses, the λ/x^2 term will become smaller than unity as the annihilation rate drops below the expansion rate. After this point, the dark matter particles will no longer track the equilibrium abundance but instead "freeze out". For typical models, the freeze-out time is well into the non-relativistic regime $x_f \simeq 25$. After this time ($x \gtrsim x_f$), we expect $Y \gg Y_{eq}$ because $Y_{eq} \propto \exp(-x)$. In this limit, Equation 2.13 simplifies to

$$\frac{dY}{dx} = \frac{-\lambda(x)}{x^2}Y^2. \tag{2.14}$$

We can estimate Y today by solving the above equation as an integral over x from the freeze-out time x_f to today $x_0 = m/T_0 \simeq \infty$. The value of Y today, Y_∞, maps directly to

the dark matter density today: $\Omega_{dm} \propto mY_\infty/\rho_{\rm crit}$. This allows us to write

$$\Omega_{dm} \propto \left[\int_{x_f}^{\infty} \frac{[\sigma v]_0}{x^{n+2}} dx\right]^{-1} \tag{2.15}$$

$$= \frac{(n+1)x_f^{n+1}}{[\sigma v]_0}. \tag{2.16}$$

Equation 2.16 allows us to estimate how $[\sigma v]_0$ must change as a function of velocity-dependence n in order to keep $\Omega_{\rm dm}$ fixed:

$$[\sigma v]_0 \propto (n+1)x_f^{n+1}. \tag{2.17}$$

Since we expect x_f to vary only logarithmically with the cross section, let us assume $x_f \simeq 25$ in all cases. According to Equation 2.17, scaling the s-wave cross section normalization (2.11) by a factor $2x_f^2$ will give us a thermal cross section estimate for p-wave ($n = 1$):

$$[\sigma v]_0^{T\,p} \approx 50[\sigma v]_0^{T\,s} = 1.2 \times 10^{-24} \mathrm{cm}^3\,\mathrm{s}^{-1}. \tag{2.18}$$

For d-wave ($n = 2$), the scaling is $3x_f^3$ and we have

$$[\sigma v]_0^{T\,d} \approx 1875[\sigma v]_0^{T\,s} = 4.3 \times 10^{-23} \mathrm{cm}^3\,\mathrm{s}^{-1}. \tag{2.19}$$

We have checked the above two numbers by solving Equation 2.13 numerically and find them to be good approximations.

2.8 Baryonic vs. dmo densities in the Galactic Centers

We examined the ratios of the densities of ordinary matter (gas and stars) to that of dark matter in regions near the galactic center of FIRE -2 halos. Our results are shown in Figure 2.23. As anticipated, the halos are dominated by baryonic matter near their most central regions, and then fall below an even 1:1 at 3-8 kpc from the center. Interestingly, the ratios vary substatially from halo to halo. For example, `Louise` and a few others have a baryonic content roughly 10 times larger than their dark matter content within the innermost resolved region (400 pc), but other halos, such as Thelma have ratios of up to 20 to 30 times greater at the same radius. Understanding the run-to-run variance in baryonic to dark matter density ratios will be a goal of future work.

2.9 Comparison to Local Maxwellian Assumption

As discussed in Section 2.3.2, we calculate the p-wave and d-wave J-factors (Equations 2.8 and 2.9) by measuring local relative velocity moments μ_2 and μ_4 in the vicinity of each dark matter particle in the simulation. In this section we ask how our results would have changed had we instead estimated the velocity moments using the local velocity dispersion $\sigma_v^2 = \langle v^2 \rangle$ and assumed a spherically-symmetric Maxwellian approximation. With this assumption, the second moment of the relative velocity would be $\mu_2 = \langle (\vec{v_1} - \vec{v_2})^2 \rangle = 2\langle v^2 \rangle$, since the cross terms vanish under spherical symmetry. The same assumptions give $\mu_4 = \langle (\vec{v_1} - \vec{v_2})^4 \rangle = 2\langle v^4 \rangle + 2\langle v^2 \rangle^2 = 48/9 \langle v^2 \rangle^2$. Here we are using $\langle v^4 \rangle = 15/9 \, \langle v^2 \rangle^2$ from the Maxwellian assumption and again assuming the cross terms vanish by spherical symmetry.

We see that the direct calculation yields results that are $\sim 20\%$ lower for p-wave and $\sim 40\%$ lower for d-wave. Similar results were obtained for all the other halos.

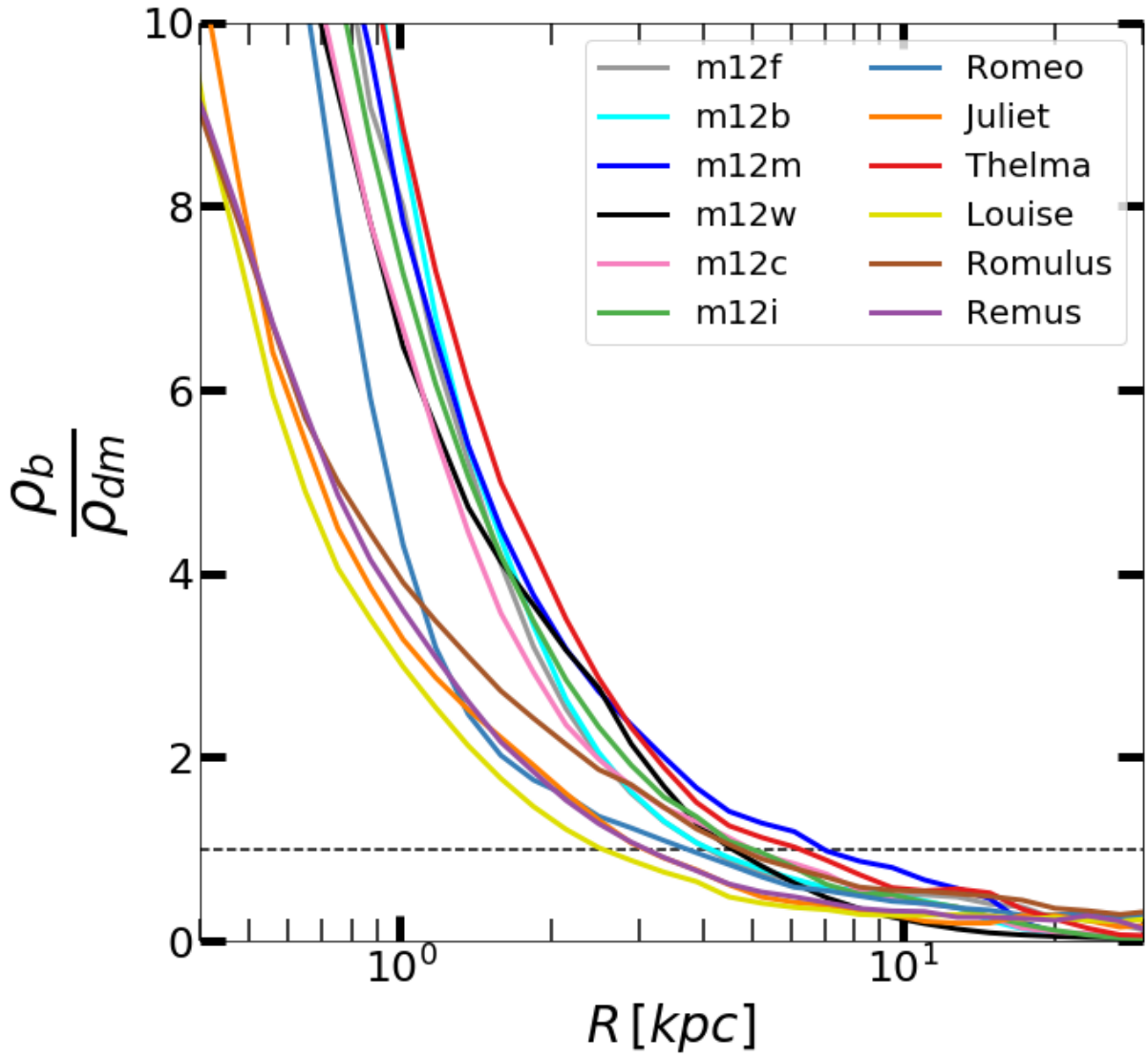

Figure 2.23: Ratio of baryonic density to dark matter density at as a function of radius within FIRE halos .Note all halos are baryon dominated at inner radii until falling to roughly 1:1 near a mock solar location $\sim$ 8 kpc.

Figure 2.24 shows the comparison of our standard treatment (solid) to the spherical Maxwellian treatment (dashed) for `Juliet`. We see that the direct calculation yields results that are $\sim 20\%$ lower for p-wave and $\sim 40\%$ lower for d-wave. Similar results were obtained for all the other halos.

2.10 Conclusions

We have explored how galaxy formation affects predictions for the astrophysical J-factors of Milky Way size dark matter halos. For a fixed particle physics model, astrophysical J-factors are directly proportional to the expected flux of Standard Model particles sourced by dark matter annihilation, and therefore provide a crucial input for dark-matter indirect detection searches in the Milky Way (see Eq. 2.4). In particular, we have used twelve FIRE zoom simulations of Milky Way-type galaxies along with dark-matter-only (DMO) versions of the same halos and worked out implications for both velocity-independent (s-wave) and velocity-dependent (p-wave and d-wave) annihilation cross sections.

One significant result is that the central dark matter velocity dispersion in FIRE halos is *systematically* amplified by factors of $\sim 2.5 - 4$ compared to their DMO counterparts (see Figure 2.4). The effect of galaxy-formation on the central dark matter density in the same halos is less systematic, sometimes increasing and sometimes decreasing the central density,

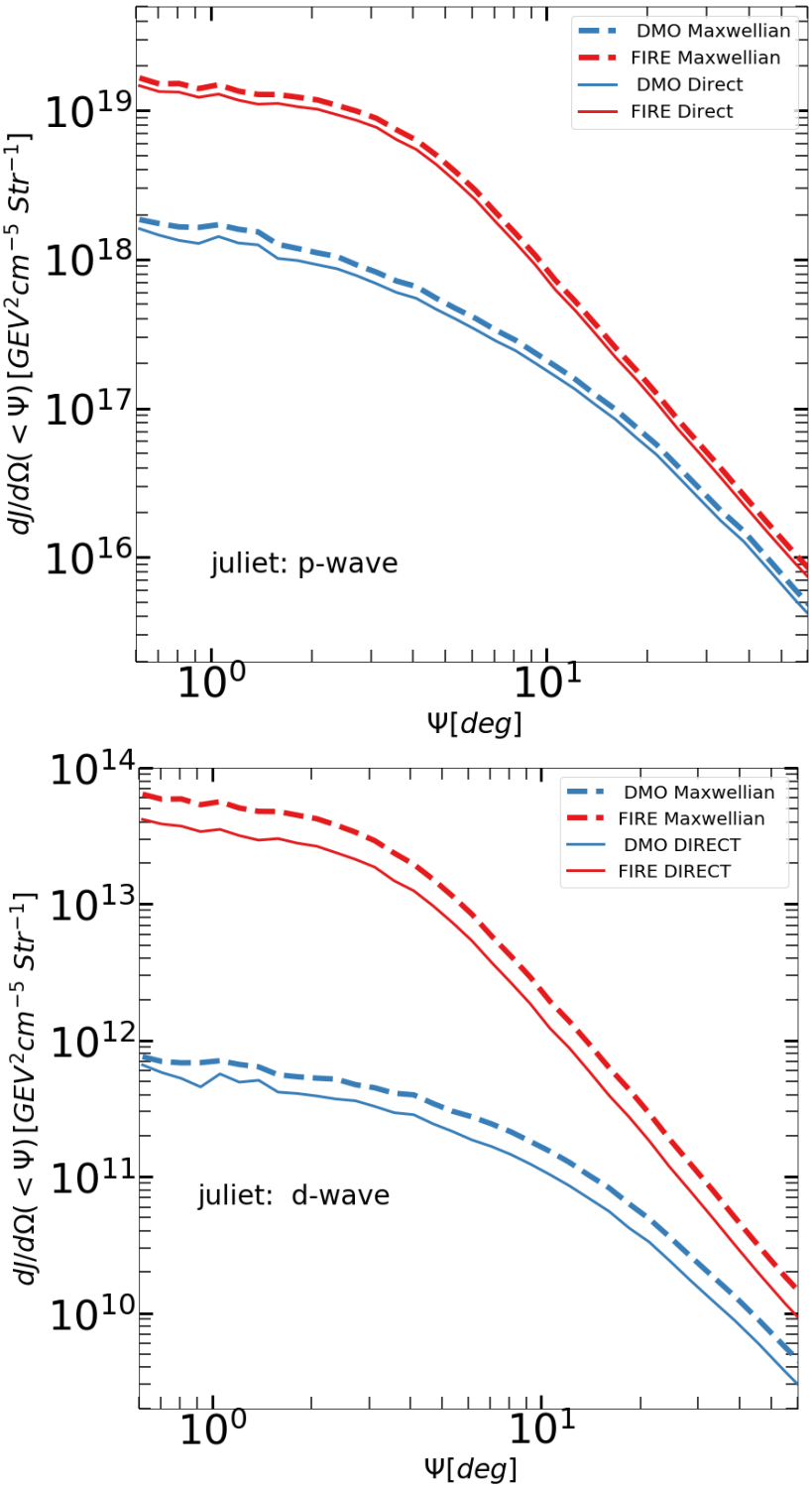

Figure 2.24: Comparison of differential p-wave (top) and d-wave (bottom) J-factor for `Juliet` using a local spherical Maxwelllian approximation (dashed) and direct velocity moments (solid)

.

with ratios ranging from $\sim 0.3 - 2.5$ (see Figure 2.3.) For p-wave ($\propto (v/c)^2$) and d-wave ($\propto (v/c)^4$) models, our FIRE-derived J-factors are amplified by factors of $\sim 3 - 60$ and $\sim 10 - 500$ compared to DMO runs (see Figures 2.15 and 2.16). FIRE halos generally produce J-factor profiles that are flatter (less peaked) towards the Galactic Center (see Figures 2.11, and 2.12, 2.13) and rounder on the sky (see bottom images of 2.5 and 2.8) , 2.6 and 2.9) , 2.7 and 2.10). Note that these differences occur despite the fact that we have normalized all of our halos to have the same local (solar location) dark matter density. That is, these results are driven by differences in the *shape* of the underlying dark matter density and velocity dispersion profiles brought about by galaxy formation processes.

One basic implication of our results is that we expect p-wave and d-wave dark matter annihilation to produce more easily detectable signals than would have been expected from DMO halos. For example, while it is typical to suspect that p-wave annihilation ($\propto (v/c)^2$)) is suppressed to undetectable levels [4] in the Milky Way today (where $v \ll c$), we showed in section 2.5 that this may not be the case. With the amplified velocities we see in our FIRE runs, the detection of (or interesting constraints on) thermal-relic p-wave dark matter may not be too far out of reach. In particular, by scaling the s-wave constraints from Fermi-LAT derived by [2], we showed that a similar analysis could bring p-wave constraints to within a factor of ~ 10 of the naive thermal cross section (see Figure 2.21). Future analyses that include detailed simulation-inspired priors on the shape of the annihilation signal in these models, could potentially approach the thermal value.

Another result worth highlighting is that we see significant scatter in the density profiles (and associated s-wave J-factor profiles) in our FIRE runs. As we begin to explore joint-constraints from multiple galaxies (e.g. M31 and the Milky Way) it will be important to allow for the possibility that even halos with similar halo masses are expected to have a large scatter in J-factor normalization. Figure 2.11, for example, shows that the variance

[4] Though see [47], who have investigated the role of the central black hole in altering the dark matter velocity dispersion.

in our FIRE s-wave J-factors is larger than one order of magnitude for our sample at few degrees from the Galactic Center, despite the fact that our halos have been fixed to have the same local density of dark matter at the solar location. Similarly, the p- and d-wave J-factor enhancement in our FIRE runs can vary considerably from halo to halo. see Figures 2.12 and 2.13. This finding for galaxies with similar properties could be important for future surveys looking for J-factor signals in both our own galaxy and beyond.

As a final point, we mention that the standard FIRE-2 implementation used in our simulations does not include the effect of AGN feedback on the gas distribution, which could affect central dark matter densities. [71] have used the Horizon simulations to explore the effect of AGN feedback on the density profiles of dark matter halos in simulations with and without AGN. Their results show AGN feedback can reduce the central dark matter density compared to runs without, especially at early times and in higher mass halos. However, at the Milky Way mass scale and at z=0, dark matter profiles of halos with and without AGN are very similar down to the radii that are converged in their simulations (5 kpc, their Figure 2). This might suggest we would see very little difference for the Milky Way itself. Nevertheless, it is possible that at smaller radii ($\sim$ 400 pc, of relevance for our work) there could be some reduction in density, even for a black hole as low mass as Sgr A*, which at $\sim 4 \times 10^6 M_\odot$ [17] is lower than expected from the tight correlation seen in ellipticals and galaxies with bulges [55]. Importantly, we do not expect the enhancement in dark matter velocities to be diminished in runs with AGN feedback. If anything, we might expect an even greater enhancement in dark matter velocities if AGN feedback were strong enough to affect the dark matter density. Indeed, in the vicinity of the black hole, it is possible that the velocity spike could be significant, further motivating continued studies of gamma-ray emission near the Galactic center [47].

Chapter 3

Analyzing the Shape of J-factor Emission Signals

3.1 Introduction

An extended source of gamma-ray emission has been detected by Fermi-LAT telescope [44, 67, 39, 20, 72, 16, 47, 8, 15]. The shape of this emission on the sky is an important ingredient for determining the source(s). These could include milli-second pulsars(MSPs), hot gas and plasma in the disk, supernovae events, and potentially dark matter annihilation (see [2] for a discussion). Although an excess has been detected, significant challenges exist in resolving the data (see [4]). Excess gamma ray flux has been seen in the direction of M31 as well, [90]. This shows that the effect is not isolated to our own MW Galaxy. In the M31 case, there are uncertainties in the astrophysical gamma-ray foreground model [90].

As an example, consider MSPs as a potential source of emission. While there is a quantitative way to decide how large of a population of millisecond pulsars should exist in the overall population of stars, (see for example [88] who did this for the case of Dwarf Spheroidal

Galaxies) there is currently only a small number of MSPs that have been determined to exist in the MW disk (100 MSPs)[88]. Thus, such analysis involves assigning a population of hypothetical MSPs using scaling functions based on the stellar masses of the population for the region in question [88, 28] Interpreting the magnitude of the signal at the galactic center as due to MSPs is left to being approximate and not definitive. It is difficult then to definitely rule out in favor of or against the gamma rays being from another source (see [53] and [85]) However, if additional criteria are examined, such as the shape of the emission signal, there could be a more definitive answer [88],[90], [2],[53], [85].

As an example of the power of emission-shape templates, [2] showed that allowing for a "boxy" bulge template for stellar emission allowed them to rule out a range of thermal WIMP dark matter models. Interestingly, however, [26] found that the Galactic Center Excess has a shape on the sky well fit by an ellipsoid with a fairly round axis ratio $0.8 - 1.2$, where the axes are aligned along the galactic plane. This is more spherical than the “boxy bulge" shape of emission reported in Ref. [61] (which has a short-to-long ratio of ~ 0.55) and used by [2] to rule out some thermal dark matter models. Instead, [26] conclude that the more spherical GCE shape is more consistent with what is expected from a dark matter annihilation signal. They suggest the disagreement is owing to the different background components used in the two analyses. Independent of who is ultimately correct in characterizing the shape of the galactic center excess, the expected shape of dark matter emission is key to the final interpretation.

Similarly, [90] have utilized the shape in the case of M31 using the PAndAS survey and removal of foreground stars to map the stars in the Galactic region of interest and then assign a probabilistic population of millisecond pulsars in the bulge. They found that this population would explain the gamma ray excess without the need for any dark matter annihilation. This was done with modeling the stellar population and its distribution. While [90] took into account the shape of the stellar populations in their analysis, they assumed that

the dark matter halo was spherical. It is possible that with a careful allowance for realistic, non-spherical dark matter structure around M31 that the dark matter interpretation could be warranted. Knowing the potential shape of such an emission signal based on its location is thus useful in itself for future studies that may rule out or limit theories for dark matter annihilation as a possible gamma ray source.

Typically, authors assume analytic dark matter profiles when interpreting indirect detection signals. Popular models include spherical NFW, spherical cored profiles, and/or 3D ellipsoidal versions of those profiles, with specific choices of axis ratios (see [2]). Numerical simulations provide a more precise prediction for the expected shapes of dark matter halos, including [12] who use Illustris simulations, with somewhat lower resolution than our own, and conclude that galaxy formation renders halos more spherical, on average, that DMO simulations.

In what follows, we examine the shape of the expected dark matter annihilation emission signal using J-factor sky maps of the simulations described in Chapter 1. Rather than estimate the 3d shape of our dark matter distributions with approximate ellipsoidal fits, we instead fit ellipses on the sky from mock observer planes. This allows a more direct prediction for what will be observed without the need to project the 3d fits. Our goal is to provide accurate dark-matter annihilation shape estimates, in order to enable studies to distinguish excess emission from the many other possible sources.

Past simulation work shows us that dark matter emission is somewhat circular on the sky. For example, [12] used hydrodynamic simulations, with somewhat lower resolution than our own, to show through their analysis that s-wave annihilation signals from dark matter sources should be fairly symmetrical with axis ratios typically greater than 0.8. It is important to note that they defined these ratios in terms of a J-factor-weighted-inertia-tensor, averaged over the whole sky. Our work, which allows us to track emission shapes quite close to the Galactic Center (within $\sim 3^{\circ}$), allows us to measure the shape as a function of angle on the

sky and we extend the shape analysis to p-wave and d-wave models as well. The reason we do this, is because it is closer to how an observational signal is measured.

3.2 Methodology

Previous studies have assumed a variety of shapes for the dark matter annihilation, informed by past numerical work on dark matter halo shapes (e.g. [2],[90]). There is a significant literature on the 3d shapes of dark matter halos, both in DMO simulations [7] and with full hydrodynamics [22]. Most of this theoretical work characterizes halos shapes by fitting the dark matter distributions to ellipsoidal configurations. These ellipsoidal fits must then be projected in the J-factor integral in order to determine the shape on the sky. We chose to work directly with the most observationally-relevant predictions for indirect detection: the J-factor itself.

We specifically characterize the shape of the J-factor on the sky. See Chapter 2 for a detailed description of our calculation of these in simulations. We find that, at a fixed $dJ/d\Omega$ contour, the shape is well-fit by an ellipse, with semi-major axis $R_{\rm major}$ and semi-minor axis $R_{\rm minor}$ measured in degrees on the sky. We use least squares fitting to fit ellipses to the J-factor emission, viewed from the solar location, as described in Chapter 2. The ratio of minor to major axes ($R_{\rm minor}/R_{\rm majo}$) allows us to characterize the shape of each contour, with ratio 1.0 corresponding to circular/spherical emission.

We provide fits to contours at specific J-factor values for s,p,d wave annihilation models and fits to contours a specific fraction of peak emission for each halo. This provides a way to measure both “brightness" or “size" of emission (at fixed J, larger $R_{\rm major}$ values are brighter and bigger on the sky) and also the shape or “flatness" of emission on the sky (at fixed fraction of peak J, larger values of $R_{\rm major}$ have flatter emission profiles).

Our results are illustrated in the figures to follow and summarized in Tables 3.1 – 3.13. As discussed in 3.4, the first set of tables (3.1 – 3.7) present $R_{\rm major}$ and $R_{\rm minor}$ values and associated axis ratios for each of our halos (DMO and FIRE) measured at fixed physical values of $\mathrm{d}J/\mathrm{d}\Omega$ for both unpaired and paired runs,and for s, p, and d-wave dark matter.The second set of tables show the same information for $\mathrm{d}J/\mathrm{d}\Omega$ contours measured at 20% of the peak flux for each halo. The second set of tables also provides the orientation angle of $R_{\rm major}$ with respect to the Galactic plane in each FIRE simulation.

3.3 Example J-factor Emission Sky Maps

Figures 3.1 - 3.6 show example all-sky J-factor maps for `Juliet`, `JulietDMO`, `M12c`, and `M12cDMO` for s-wave, p-wave, and d-wave cases. For each of the FIRE runs, the disk axis is oriented horizontally. The orientation of the DMO halo is arbitrary. The dotted horizontal and vertical lines are spaced by 30 and 45 degrees respectively, to guide the eye.

In each figure, the DMO version is shown on top, while the FIRE version is shown on the bottom. The color bars are the same for each pair of halos, though they change depending on whether it is s-wave, p-wave, or d-wave dark matter. The black lines, on the other hand, are contours plotted at a constant peak emission fraction *for each map specifically.* The lines correspond to 50,20,10,5, and 1 percent of the peak emission level, giving us 5 contours. Here we summarise the results for each type of dark matter (s-wave, p-wave, and d-wave).

s − wave maps :

In both s-wave maps (Figures 3.1 and 3.2) substructure is more apparent in DMO and much less so in FIRE. We see that the countours are more elongated DMO compared to FIRE. Interestingly, the faintest contours are slightly asymmetrical for DMO, with centers that do not seem to be in alignment (which is to say, the centers of the innermost contour don't

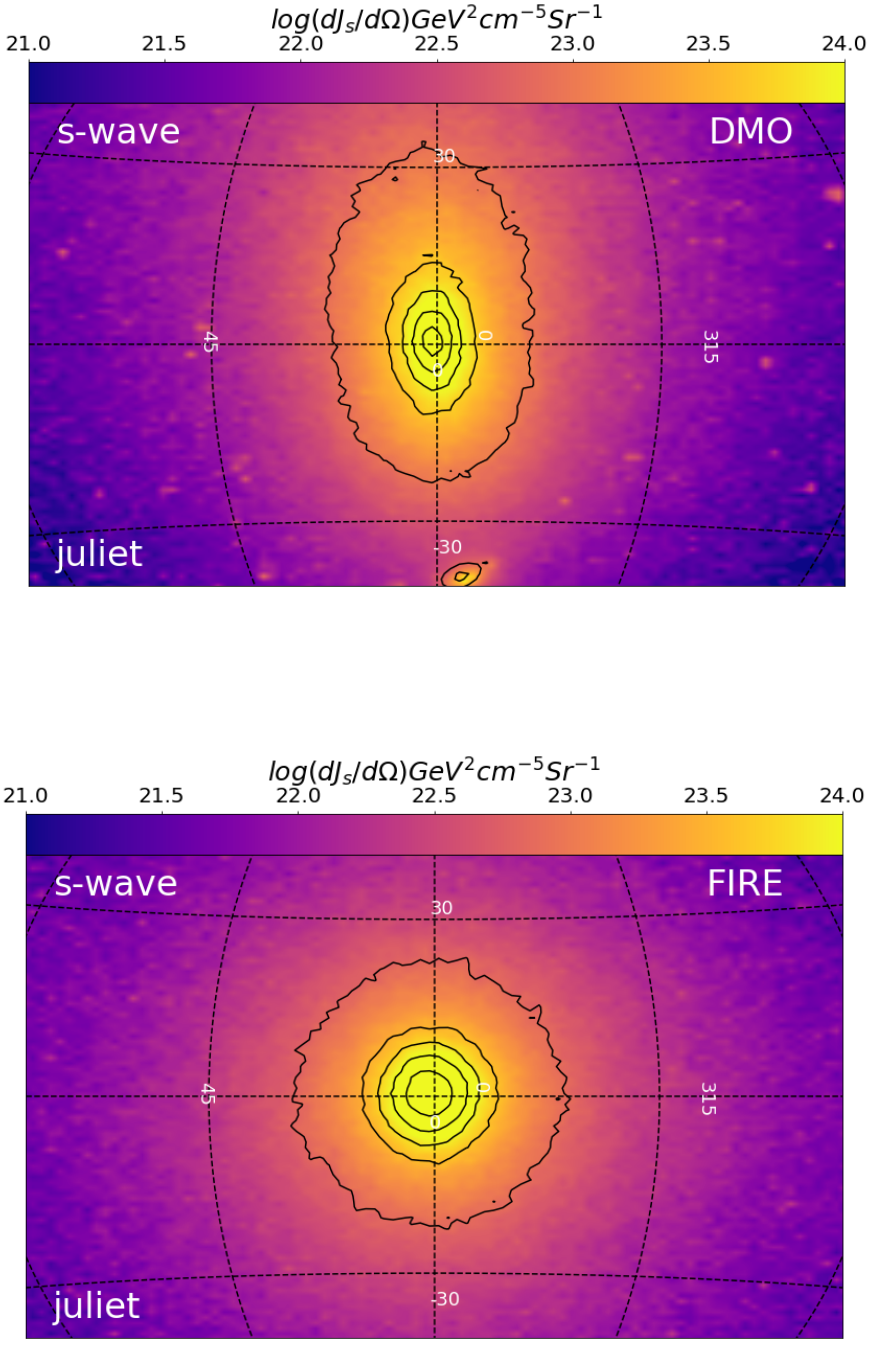

Figure 3.1: All sky maps of s-wave J-factor for `Juliet`. The DMO version is shown on top and full physics FIRE on the bottom. The horizontal and vertical lines are spaced by 30 and 45 degrees respectively, to guide the eye. To emphasize the shape of the emission, black solid contours are drawn at a fixed fraction of the maximum pixel in each halo: 0.5, 0.2, 0.1, 0.05, and 0.01. Note that FIRE contours are more symmetric and circular than the DMO contours. Note the substructure in DMO maps. We see some mild flattening along the disk plane in the FIRE run.

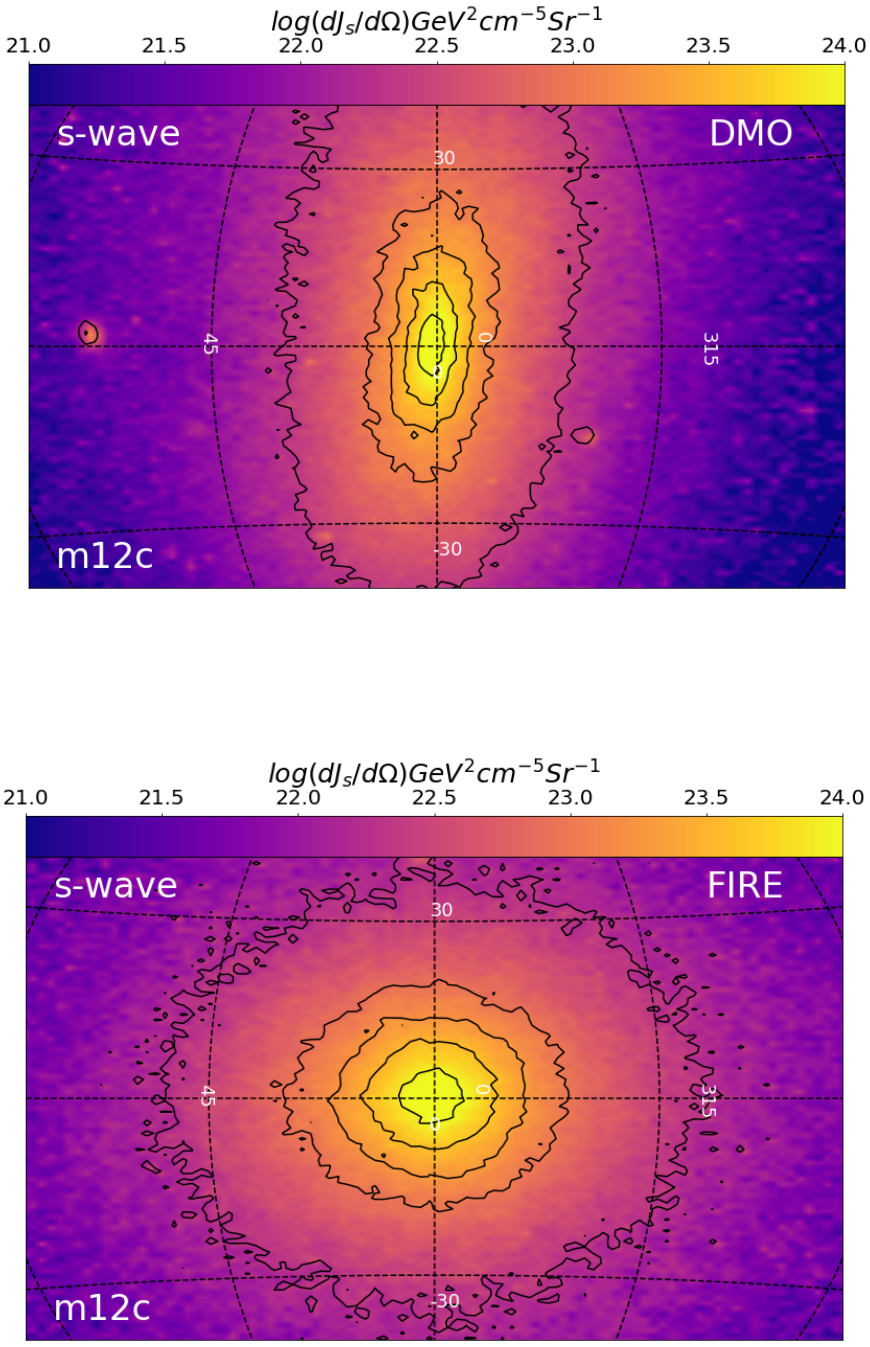

Figure 3.2: Sky maps for s-wave J-factor emission for `m12c`, DMO (top) and FIRE (bottom). Same description as for Figure 3.1. Substructures are also clearly visible in DMO map.

match with the outermost). Meanwhile, FIRE contours have centers which appear well-aligned with the center of the galaxy as defined by our halo finder. The contours for FIRE are more circular. The contour for the 50 percent peak emission is generally larger for FIRE, as expected for an emission profile that is a little bit flatter in the center. While none of the emission contours perfectly "centered", they are consistent with zero within our numerical resolution, which is roughly 2.7°.

Note that the contours are oriented vertically with respect to the Galactic plane in `m12cDMO`. However, the orientation of the plane was chosen at random in this DMO case since there is no disk in the simulation. The FIRE halos, of course, do have disks, so the Galactic plane in those cases are physically relevant. Interestingly, both `m12c` and `Juliet` we see some mild flattening of the contours along the disk planes. We find that this is generally the case for all of the FIRE halos we examine: the flattening is always along the disk plane.

p-wave maps:

Figures 3.3 and 3.4 show substructures are much less apparent for DMO maps compared to their s-wave counterparts. The DMO contours appear are quite “stretched out" compared to both the FIRE contours,and in these cases the DMO contours in the s-wave case. This is because, relative to their peak central emission, p-wave J-factor profiles are flatter than their s-wave counterparts in the DMO case (as can be seen in Figures 2.11 and 2.12). Note that the actual axis ratios of the DMO contours are actually similar to those of s-wave case, as shown below. The FIRE contours are quite similar between s-wave and p-wave. The FIRE p-wave contours resemble those of the s-wave contours, in that they are flattened mildly along the Galactic plane.

d-wave maps:

Figures 3.5 and 3.6 show the d-wave sky maps for `Juliet` and `m12c`. As in the p-wave cases, the DMO d-wave maps, and associated contours, have significantly different shapes than

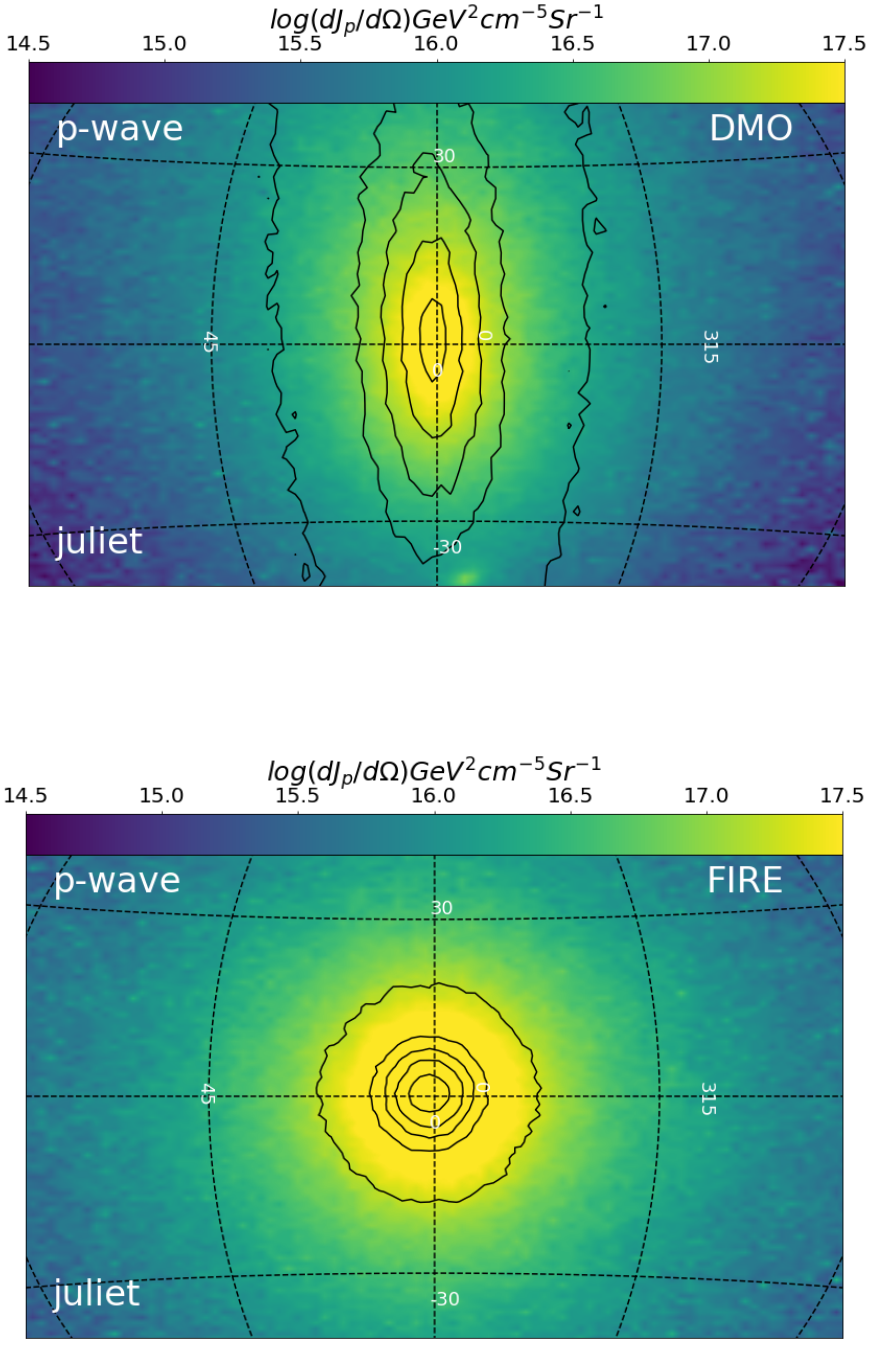

Figure 3.3: p-wave J-factor sky maps for `Juliet` DMO (top) and FIRE (bottom). J-values are color coded as indicated in the color bars (which are the same for both). Black solid contours are drawn at a fixed fraction of the maximum pixel in each halo: 0.5, 0.2, 0.1, 0.05, and 0.01. Note that the contours are quite elongated in the DMO case (though, since there is no disk, the orientation is random). FIRE contours are more symmetric and circular in comparison, with mild flattening along the disk plane.

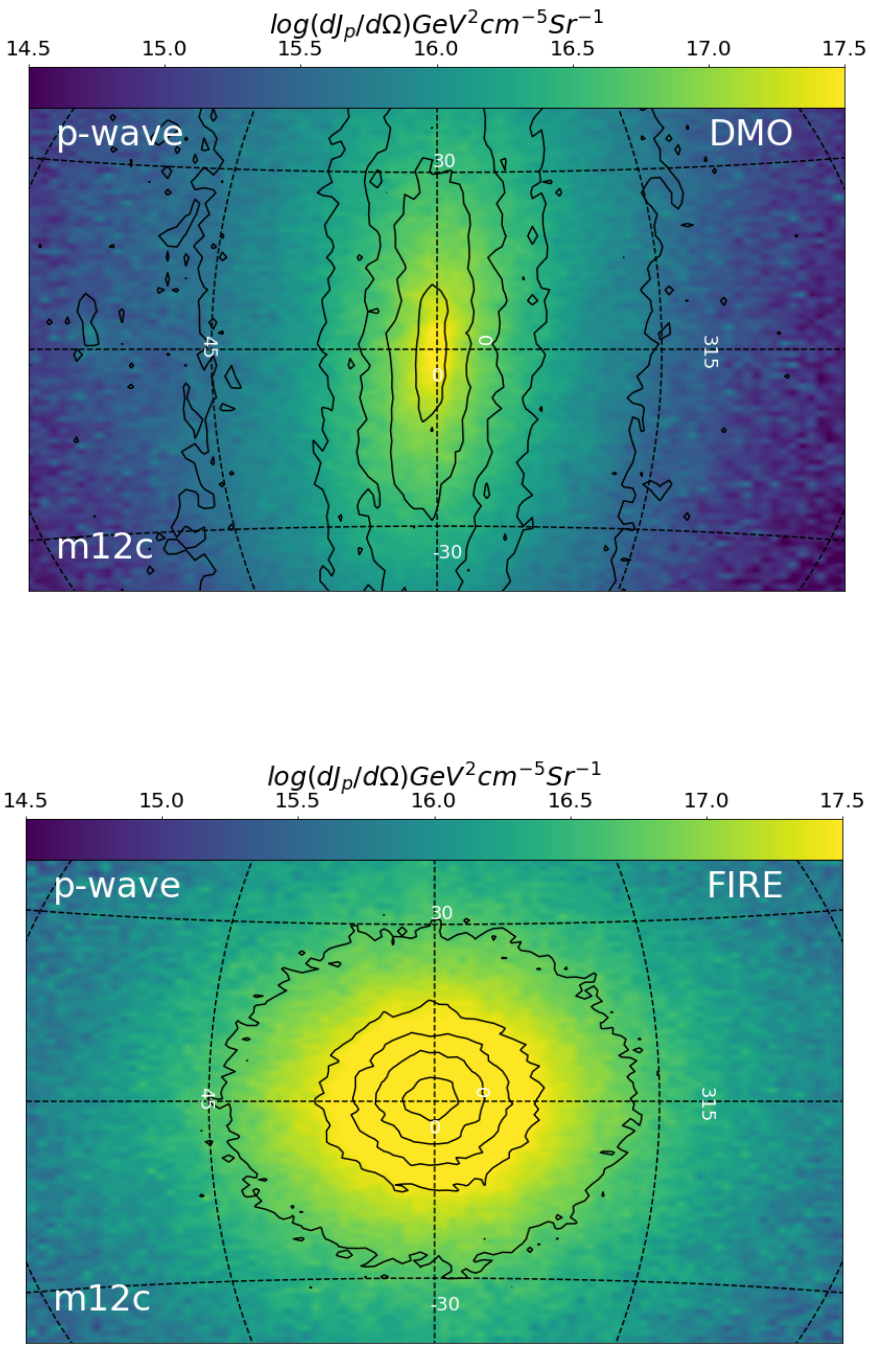

Figure 3.4: p-wave J-factor sky maps for `m12c` DMO (top) and FIRE (bottom) centered on the Galactic Center. Black solid contours are drawn at a fixed fraction of the maximum pixel in each halo: 0.5, 0.2, 0.1, 0.05, and 0.01.

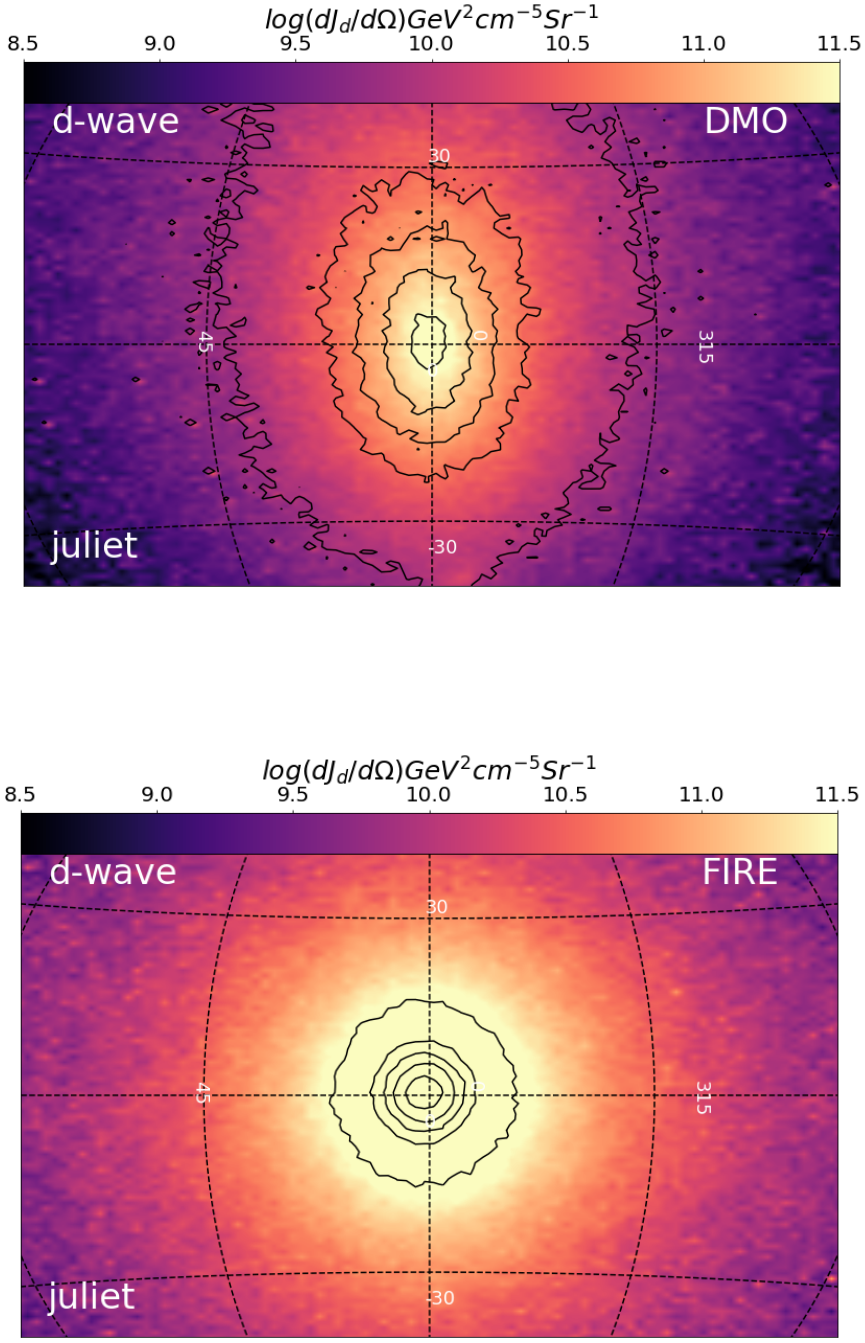

Figure 3.5: d-wave J-factor sky maps for `Juliet` DMO (top) and FIRE (bottom) centered on the Galactic Center. Contours are drawn at the same percentages of peak signal as earlier skymaps of s and p wave. d-wave contours for `Juliet` have a smaller angular extent than `m12c`. As noted in Chapter 2, differences in J-factors from halo to halo are considerable.

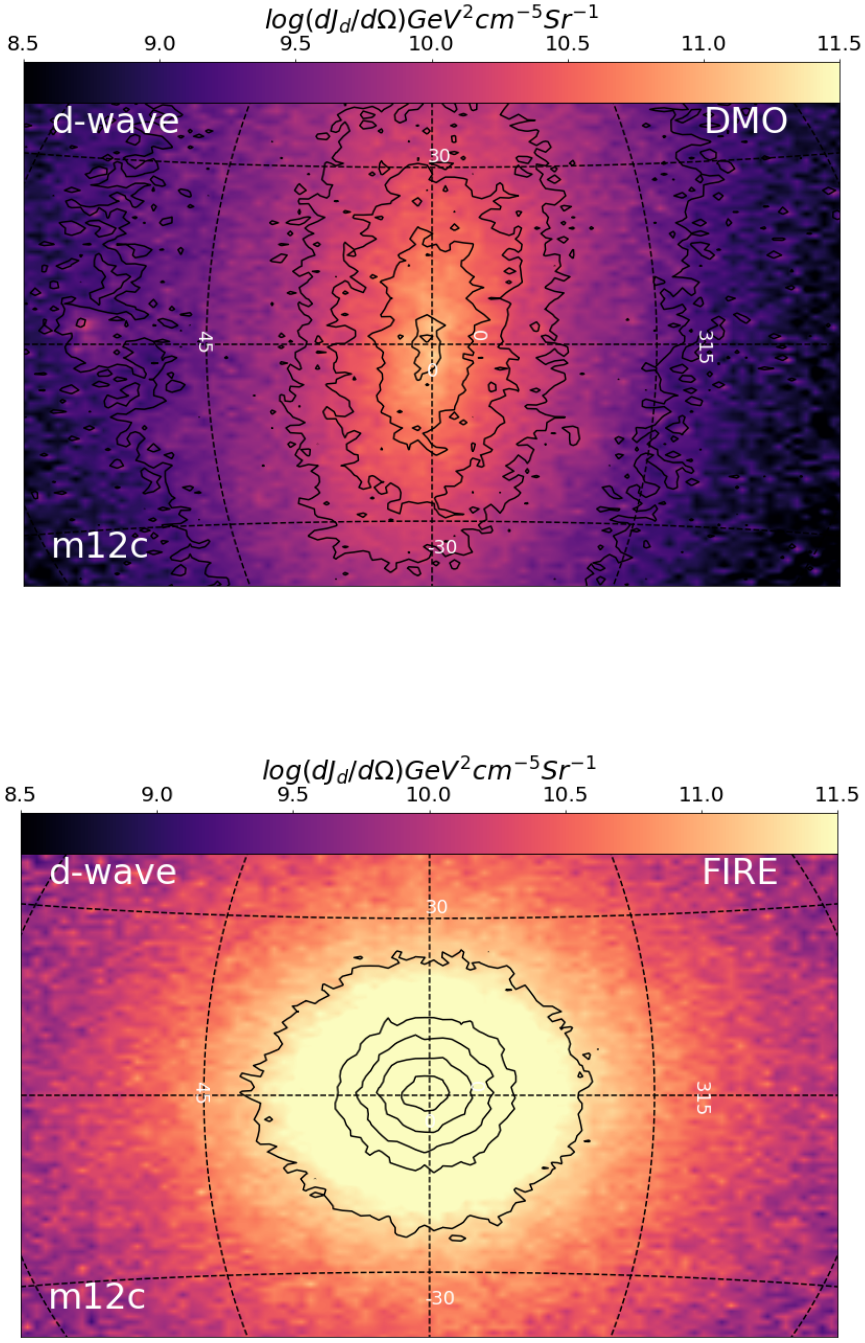

Figure 3.6: d-wave J-factor sky maps for `m12c` DMO (top) and FIRE (bottom) centered on the Galactic Center. The contours are drawn at the same percentages of the peak pixel as s and d wave maps. Compared to s-wave, the shapes of both DMO and FIRE appear rounder, but the effect is stronger for FIRE.

in the s-wave case. The FIRE runs, on the other hand, are much more similar, with less variation for the assumed mode of annihilation. The FIRE contours are much rounder, and revealed a more centrally-concentrated emission profile.

3.4 Population Results: Elliptical Fits on the Sky

Tables 3.1 – 3.13 provide a summary of shape information of on-sky ellipse fits for all of our halos, listed in DMO and FIRE pairs in each case.

In the first set of tables (3.1 – 3.7), we list $R_{\rm major}$ and $R_{\rm minor}$ values and associated axis ratios fit to contours set at fixed dJ/dΩ values that are representative of the "bright" inner regions of halos for s-, p-, and d-wave models. These tables also list the ratio of minor to major axis, which provides a measure for how far the emission deviates from circular (a value of 1.0 corresponds to perfect circle). Our fiducial choices for s-wave, p-wave, and d-wave contours are 10^{24}, $10^{17.5}$, and $10^{11.8}$ Gev^{2}cm^{-5}Sr^{-1}, respectively. Though, for a subset of the "dimmest" DMO/FIRE halo pairs were were forced to chose slightly smaller values for the dJ/dΩ contours in order to achieve a smooth fit (see Table captions). By measuring the shapes and angular extent of contours at a fixed dJ/dΩ value, we are able to compare and contrast the "brightness" or "size" of emission: at fixed values, larger $R_{\rm major}$ values are brighter and bigger on the sky.

The second set of tables (3.8 – 3.13) provide similar information, but now using dJ/dΩ contours measured at 20% of the peak flux for *each halo individually*. By measuring the shapes and angular extent of contours at a fixed fraction of peak dJ/dΩ emission, we provide information on the relative "flatness" of emission on the sky: larger values of $R_{\rm major,20}$ have flatter emission profiles, smaller R_{20} values are more peaked. For the FIRE versions of each halo, we also list the orientation angle of the major axis fit with respect to the Galactic

Table 3.1: On-sky ellipse fits to s-wave j-factor contours of fixed value 10^{24} Gev^{2}cm^{-5}Sr^{-1} ($*$ implies $10^{23.7}$). Columns list the following: (1) Simulation name. (2) The semi-major axis of the elliptical fit (3) The semi-minor axis of the elliptical fit (4) The ratio of semi-minor/semi-major axis of the elliptical fit.

Simulation	semi-major axis	semi-minor axis	ratio (major/minor)
`M12i`*	11.2°	8.95°	0.80
`M12iDMO`*	4.41°	2.92°	0.66
`M12c`	6.18°	4.21°	0.71
`M12cDMO`	6.52°	3.21°	0.49
`M12m`	3.91°	1.49°	0.38
`M12mDMO`	6.23°	4.13°	0.66
`M12f`	5.42°	4.01°	0.74
`M12fDMO`	5.53°	3.17°	0.57
`M12w`	5.08°	4.21°	0.83
`M12wDMO`	2.71°	1.96°	0.72
`M12b`	6.61°	5.24°	0.79
`M12bDMO`	5.73°	5.46°	0.95

plane. Recall that we have oriented our observer in the plane of the disk formed in each FIRE simulation, so the orientation angle is meaningful. The DMO versions are observed from an arbitrary disk plane, so the orientation with respect to the galactic plane is not physically meaningful.

As expected from the previous figures, we see from Tables 3.8 – 3.13 that the major axes of the contours are always aligned to within $\sim 4°$of the plane, with one outlier (`M12b` d-wave) aligned at 7°. This level of alignment provides a potentially powerful prior for the expected alignment of emission signals from dark matter annihilation.

Figures 3.7, 3.8, and 3.9 show the best-fit major-axis values for DMO runs (vertical axis) versus FIRE runs (horizontal axis). The top panels, in each case, show the major axis values computed at fixed $dJ/d\Omega$ values, as described above. The bottom panels, in each case, show the same except for major axis fits to contours set at 20 percent of the peak emission of each halo.

In the cases of s,p and d-wave, we find a significantly larger elliptical function in terms of its major axes and minor axes. This is expected, since in our previous results we showed in Chapter 2 that full baryonic physics enhances and increases the signal particularly its spatial extents. In many cases, the shape of the ellipse is rounder for the FIRE emission signals than it is for the DMO.

Figures 3.10 , 3.11, and 3.12 plot the axis ratios (minor/major) obtained for the 20-percent contour fits in DMO (vertial) versus FIRE (horizontal) for s-wave, p-wave, and d-wave, respectively. The solid blue lines show the one-to-one relation to guide the eye. When points lie below the line, it means the FIRE runs are rounder on the sky. We see that, typically, the FIRE runs are indeed rounder. Though not always. Importantly, the J-contours in FIRE have axis ratios that are similar, with a full range spanning $0.65 - 0.9$, and typical values around ~ 0.8. The DMO runs show much larger variance $\sim 0.4 - 0.95$.

Table 3.4: On-sky ellipse fits to p-wave contours of fixed value $10^{17.5}$ Gev^{2}cm^{-5}Sr^{-1}. Note $*$ implies $10^{16.9}$ in the same units and $**$ implies $10^{17.1}$). Columns list the following: (1) Simulation name. (2) The semi-major axis of the elliptical fit. (3) The semi-minor axis of the elliptical fit. (4) The ratio of semi-minor/semi-major axis of the elliptical fit.

Simulation	semi-major axis	semi-minor axis	ratio (minor/major)
M12i*	21.1°	16.6°	0.79
M12iDMO*	11.1°	6.04°	0.54
M12c*	33.3°	22.6°	0.67
M12cDMO*	15.6°	8.03°	0.52
M12m	24.3°	15.6°	0.64
M12mDMO	6.49°	4.42°	0.68
M12f	21.9°	17.3°	0.79
M12fDMO	3.82°	2.30°	0.60
M12w**	30.0°	23.0°	0.77
M12wDMO**	8.05°	5.68°	0.70
M12b	23.2°	19.5°	0.84
M12bDMO	7.94°	7.42°	0.93

Table 3.5: On-sky ellipse fits to p-wave contours of fixed value $10^{17.5}\mathrm{Gev}^2\mathrm{cm}^{-5}\mathrm{Sr}^{-1}$. Note $*$ implies$10^{16.9}$ and $**$ implies $10^{17.1}$ in the same units. Columns list the following:(1) Simulation name. (2) The semi-major axis of the elliptical fit (3) The semi-minor axis of the elliptical fit (4) The ratio of semi-minor/semi-major axis of the elliptical fit.

Simulation	major axis	minor axis	ratio (minor/major)
Romeo	23.6°	17.3°	0.73
RomeoDMO	8.83°	7.39°	0.84
Juliet	18.5°	15.6°	0.84
JulietDMO	10.8°	7.53°	0.70
Thelma	18.14°	13.9°	0.77
ThelmaDMO	4.53°	1.77°	0.39
Louise	16.9°	12.9°	0.76
LouiseDMO	7.60°	6.74°	0.89
Romulus	24.0°	18.0°	0.75
RomulusDMO	8.46°	5.03°	0.59
Remus	20.5°	15.7°	0.77
RemusDMO	10.7°	7.35°	0.69

Table 3.6: On-sky ellipse fits to d-wave contour values for m12 runs at dJ/dΩ values of $10^{11.5}$Gev^{2}cm^{-5}Sr^{-1}. Note $*$ implies $10^{10.8}$, $**$ implies $10^{11.8}$ Columns list the following:(1) Simulation name. (2) The semi-major axis of the elliptical fit (3) The semi-minor axis of the elliptical fit (4) The ratio of semi-minor/semi-major axis of the elliptical fit.

Simulation	major axis	minor axis	ratio (minor/major)
M12i**	22.6°	17.7°	0.79
M12iDMO*	5.77°	2.10°	0.36
M12c*	44.0°	31.4°	0.71
M12cDMO*	10.9°	6.64°	0.61
M12m	38.1°	24.8°	0.65
M12mDMO*	15.5°	12.3°	0.80
M12f	27.1°	21.2°	0.78
M12fDMO	8.31°	5.87°	0.71
M12w	28.0°	20.6°	0.74
M12wDMO*	8.93°	6.00°	0.67
M12b	33.1°	27.9°	0.84
M12bDMO	5.19°	4.93°	0.95

Table 3.7: On-sky ellipse fits to d-wave contour values for MW-M31-like pairs at dJ/dΩ contour values of $10^{11.5}$Gev^{2}cm^{-5}Sr^{-1}. Note: $*$ implies $10^{10.8}$, $**$ implies $10^{11.8}$ Columns list the following:(1) Simulation name. (2) The semi-major axis of the elliptical fit (3) The semi-minor axis of the elliptical fit (4) The ratio of semi-minor/semi-major axis of the elliptical fit.

Simulation	major axis	minor axis	ratio (minor/major)
Romeo	31.7°	23.8°	0.75
RomeoDMO	6.50°	5.20°	0.80
Juliet	23.0°	19.6°	0.85
JulietDMO	5.90°	4.67°	0.80
Thelma**	20.5°	16.6°	0.81
ThelmaDMO*	16.7°	6.98°	0.42
Louise	19.9°	15.6°	0.79
LouiseDMO	4.0°	2.8°	0.69
Romulus	35.5°	26.6°	0.75
RomulusDMO	5.81°	3.13°	0.54
Remus	27.1°	21.2°	0.78
RemusDMO	8.31°	5.87°	0.71

Table 3.8: Ellipse fits characterizing the shape of on-sky s-wave dJ/dΩ maps for each m12 simulation. Fits are to contours at 20 percent of the peak dJ/dΩ value in the map.(1) Simulation name (2) The semi-major axis of the elliptical fit (3) The semi-minor axis of the elliptical fit (4) The ratio of minor-to-major axis of the elliptical fit. (5) Orientation angle of major axis with respect to the Galactic plane. Note that the angle for DMO is not given since the orientation is arbitrary in that case.

Simulation	semi-major axis	semi-minor axis	ratio (minor/major)	angle wrt galactic plane
`M12i`	12.5°	10.1°	0.810	2.8°
`M12iDMO`	11.8°	6.20°	0.520	-
`M12c`	14.1°	9.92°	0.701	0.66°
`M12cDMO`	11.6°	5.51°	0.480	-
`M12m`	19.6°	12.7°	0.650	1.2°
`M12mDMO`	9.50°	6.51°	0.690	-
`M12f`	14.6°	11.5°	0.784	1.0°
`M12fDMO`	12.5°	6.12°	0.490	-
`M12w`	9.54°	7.06°	0.740	2.0°
`M12wDMO`	8.73°	6.02°	0.690	-
`M12b`	14.1°	11.8°	0.842	2.4°
`M12bDMO`	6.00°	5.64°	0.943	-

Table 3.9: Ellipse fits characterizing the shape of on-sky s-wave dJ/dΩ maps for each MW-M31-like pair simulations. Fits are to contours at 20 percent of the peak dJ/dΩ value in the map. (1) Simulation name. (2) The semi-major axis of the elliptical fit. (3) The semi-minor axis of the elliptical fit. (4) The ratio of minor-to-major axis of the elliptical fit. (5) Orientation angle of major axis with respect to the Galactic plane.Note that the angle for DMO is not given since the orientation is arbitrary in that case.

Simulation	semi-major axis	semi-minor axis	ratio (minor/major)	angle wrt galactic plane
Romeo	8.90°	6.57°	0.740	0.84°
RomeoDMO	5.36°	4.35°	0.810	-
Juliet	8.24°	7.01°	0.850	1.3°
JulietDMO	5.72°	4.20°	0.740	-
Thelma	20.5°	15.7°	0.765	0.70°
ThelmaDMO	11.6°	4.81°	0.415	-
Louise	12.9°	10.1°	0.780	1.0°
LouiseDMO	6.96°	5.87°	0.844	-
Romulus	5.84°	4.57°	0.783	1.0°
RomulusDMO	10.2°	5.76°	0.565	-
Remus	9.67°	7.47°	0.772	1.1°
RemusDMO	8.04°	5.25°	0.652	-

Table 3.10: Ellipse fits characterizing the shape of on-sky p-wave dJ/dΩ maps for each simulations. Fits are to contours at 20 percent of the peak dJ/dΩ value in the map.(1) Simulation name. (2) The semi-major axis of the elliptical fit (3) The semi-minor axis of the elliptical fit (4) The ratio of minor-to-major axis of the elliptical fit. (5) Orientation angle of major axis with respect to the Galactic plane. Note that the angle for DMO is not given since the orientation is arbitrary in that case.

Simulation	semi-major axis	semi-minor axis	ratio (minor/major)	angle wrt galactic plane
`M12i`	10.7°	8.4°	0.78	2.5°
`M12iDMO`	25.2°	13.4°	0.53	-
`M12c`	11.6°	8.45°	0.730	0.98°
`M12cDMO`	16.7°	8.92°	0.530	-
`M12m`	16.48°	11.2°	0.68	2.8°
`M12mDMO`	13.5°	10.1°	0.750	-
`M12f`	12.3°	9.48°	0.774	3.1°
`M12fDMO`	15.2°	7.43°	0.490	-
`M12w`	8.67°	6.19°	0.714	4.0°
`M12wDMO`	6.13°	4.49°	0.733	-
`M12b`	11.36°	9.33°	0.823	1.0°
`M12bDMO`	9.64°	9.17°	0.950	-

Table 3.11: Ellipse fits characterizing the shape of on-sky p-wave dJ/dΩ maps for each simulations. Fits are to contours at 20 percent of the peak dJ/dΩ value in the map.(1) Simulation name. (2) The semi-major axis of the elliptical fit (3) The semi-minor axis of the elliptical fit (4) The ratio of minor-to-major axis of the elliptical fit.(5) The orientation angle of major axis with respect to the Galactic plane.

Simulation	semi-major axis	semi-minor axis	ratio (minor/major)	angle wrt galactic plane
Romeo	8.66°	6.29°	0.726	1.23°
RomeoDMO	7.73°	6.47°	0.837	
Juliet	7.32°	6.2°	0.86	1.84°
JulietDMO	9.31°	6.51°	0.701	-
Thelma	17.8°	13.7°	0.768	1.8°
ThelmaDMO	18.8°	8.47°	0.449	-
Louise	11.9°	9.21°	0.772	1.7°
LouiseDMO	13.1°	10.2°	0.773	-
Romulus	5.42°	4.30°	0.793	1.0°
RomulusDMO	19.2°	10.1°	0.527	-
Remus	8.96°	6.77°	0.755	1.3°
RemusDMO	11.7°	7.94°	0.681	-

Table 3.12: Ellipse fits characterizing the shape of on-sky d-wave dJ/dΩ maps for each simulations. Fits are to contours at 20 percent of the peak dJ/dΩ value in the map.(1) Simulation name. (2) The semi-major axis of the elliptical fit (3) The semi-minor axis of the elliptical fit (4) The ratio of minor-to-major axis of the elliptical fit.(5) The Orientation angle of major axis with respect to the galactic plane. Note:these are only defined for FIRE runs which have a disk

Simulation	semi-major axis	semi-minor axis	ratio (minor/major)	angle wrt galactic plane
`M12i`	9.32°	7.30°	0.781	0.87°
`M12iDMO`	26.7°	14.3°	0.533	-
`M12c`	10.0°	6.90°	0.682	1.2°
`M12cDMO`	20.0°	10.6°	0.531	-
`M12m`	14.4°	9.71°	0.670	1.5°
`M12mDMO`	17.4°	13.2°	0.760	-
`M12f`	10.5°	8.08°	0.770	4.5°
`M12fDMO`	15.5°	9.72°	0.627	-
`M12w`	7.78°	5.76°	0.740	4.0°
`M12wDMO`	25.8°	16.8°	0.652	-
`M12b`	9.44°	7.86°	0.832	7.0°
`M12bDMO`	13.3°	12.4°	0.933	-

Table 3.13: Ellipse fits characterizing the shape of on-sky d-wave dJ/dΩ maps for each simulations. Fits are to contours at 20 percent of the peak dJ/dΩ value in the map.(1) Simulation name. (2) The semi-major axis of the elliptical fit (3) The semi-minor axis of the elliptical fit (4) The ratio of minor-to-major axis of the elliptical fit.(5) The orientation angle of major axis with respect to the galactic plane. Note: these are only defined for FIRE runs which have a disk

Simulation (ℓ, b)	major axis	minor axis	ratio (minor/major)	angle wrt galactic plane
Romeo	8.37°	6.05°	0.723	1.9°
RomeoDMO	11.2°	9.548°	0.853	-
Juliet	6.6°	5.40°	0.82	3.0°
JulietDMO	13.3°	9.4°	0.710	-
Thelma	15.5°	12.2°	0.786	4.1°
ThelmaDMO	26.9°	12.7°	0.471	-
Louise	10.7°	8.60°	0.804	0.37°
LouiseDMO	17.0°	13.6°	0.803	-
Romulus	5.10°	4.01°	0.786	1.0°
RomulusDMO	25.7°	15.2°	0.590	-
Remus	8.27°	6.18°	0.748	1.6°
RemusDMO	15.1°	10.5°	0.696	-

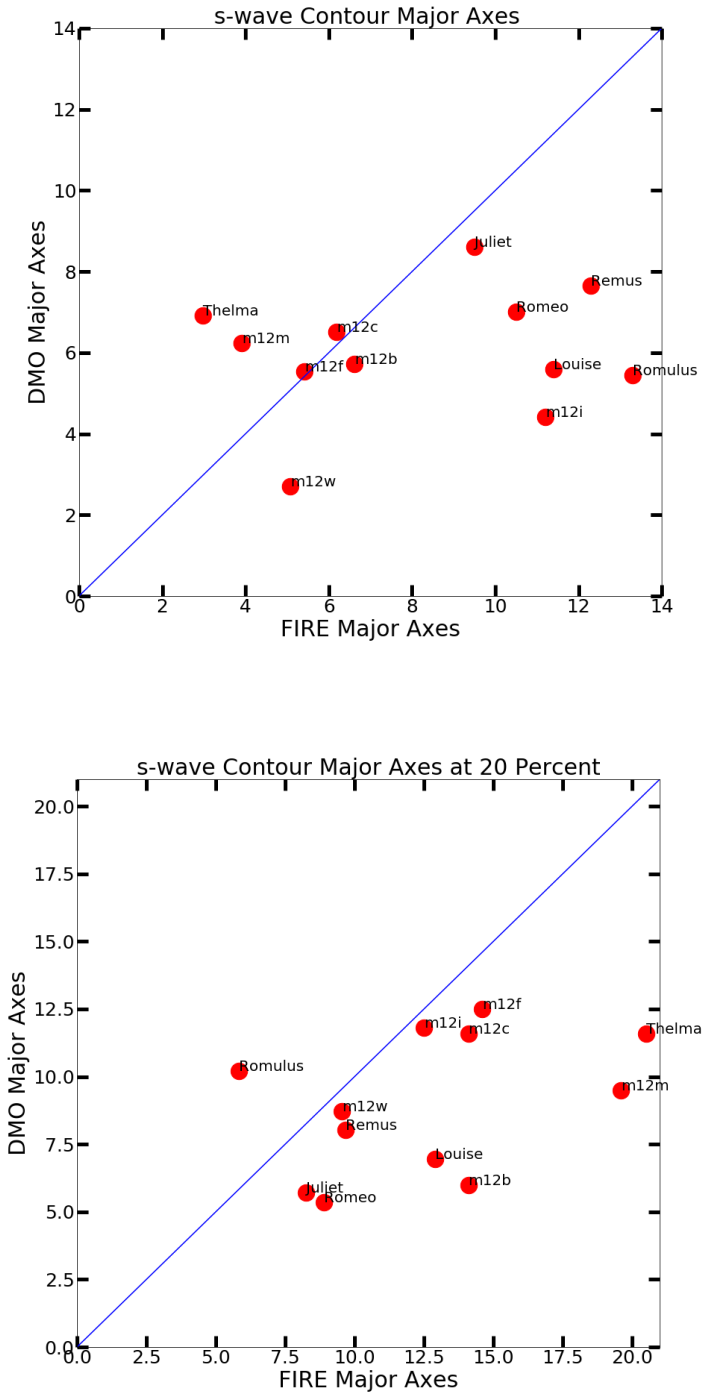

Figure 3.7: **Top** : Best-fit ellipse-fitted major axis values **in degrees** for DMO runs (vertical) and FIRE runs (horizontal). These ellipse fits correspond to a fixed contour value of 10^{24} $\mathrm{Gev^2 cm^{-5} Sr^{-1}}$on the sky. **bottom** : The same except for ellipse fits are done at 20 percent the maximum value in the map. We see that the FIRE runs are typically more extended at fixed fraction of peak emission, meaning that the profiles are “flatter" in shape.

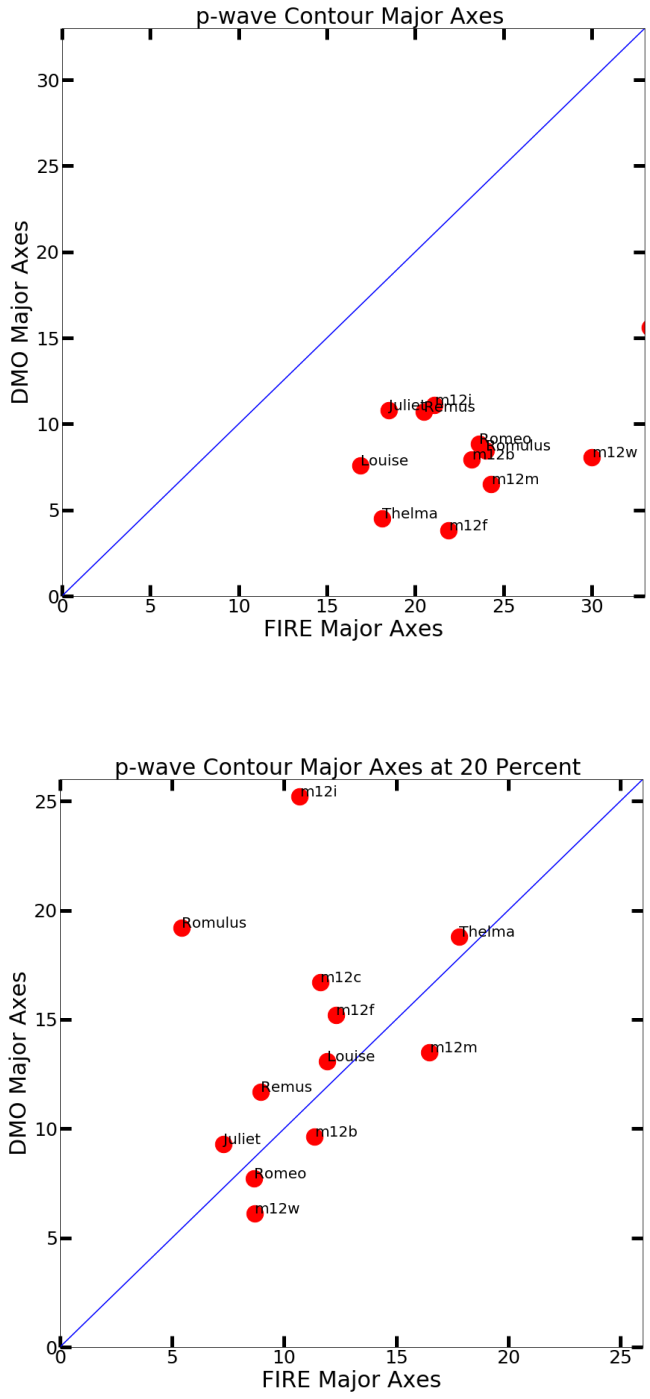

Figure 3.8: The same as Figure 3.7 except for p-wave. The upper panel shows ellipse fits to contours at $10^{17.5}$ Gev^{2}cm^{-5}Sr^{-1}.

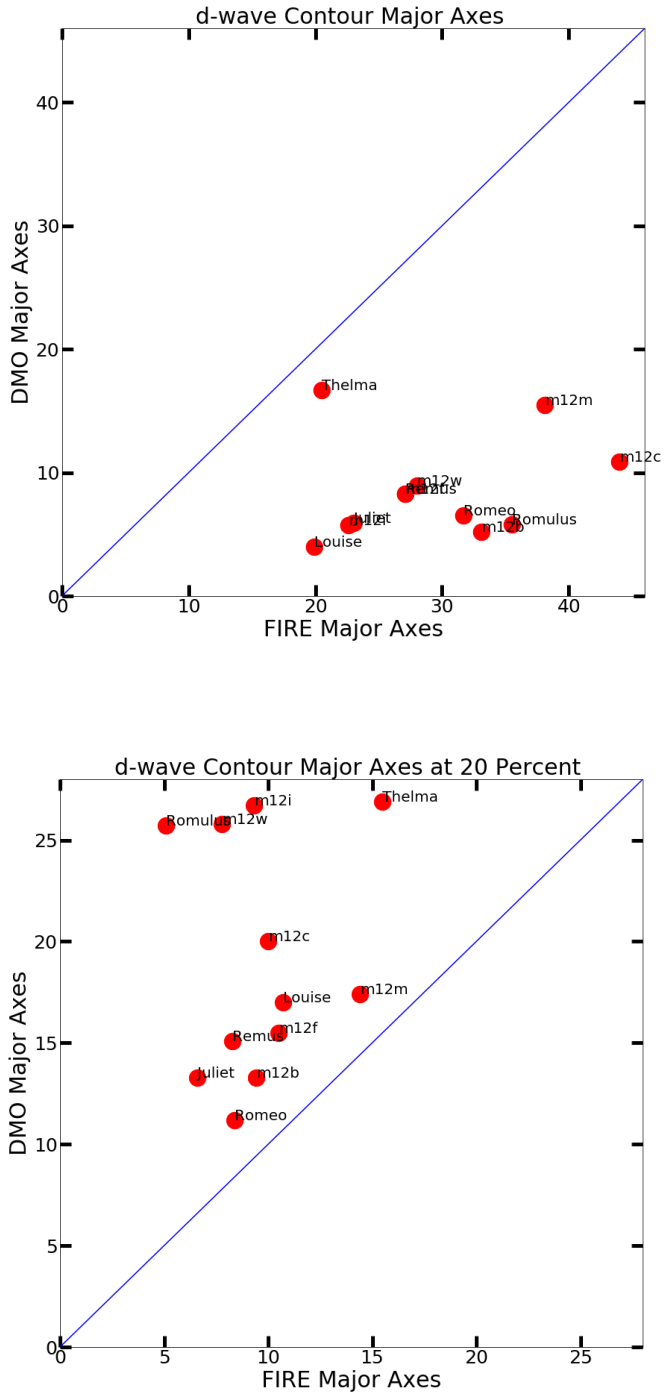

Figure 3.9: The same as Figure 3.7 except for d-wave. The upper panel shows ellipse fits to contours at $10^{11.8}$ Gev^{2}cm^{-5}Sr^{-1}.

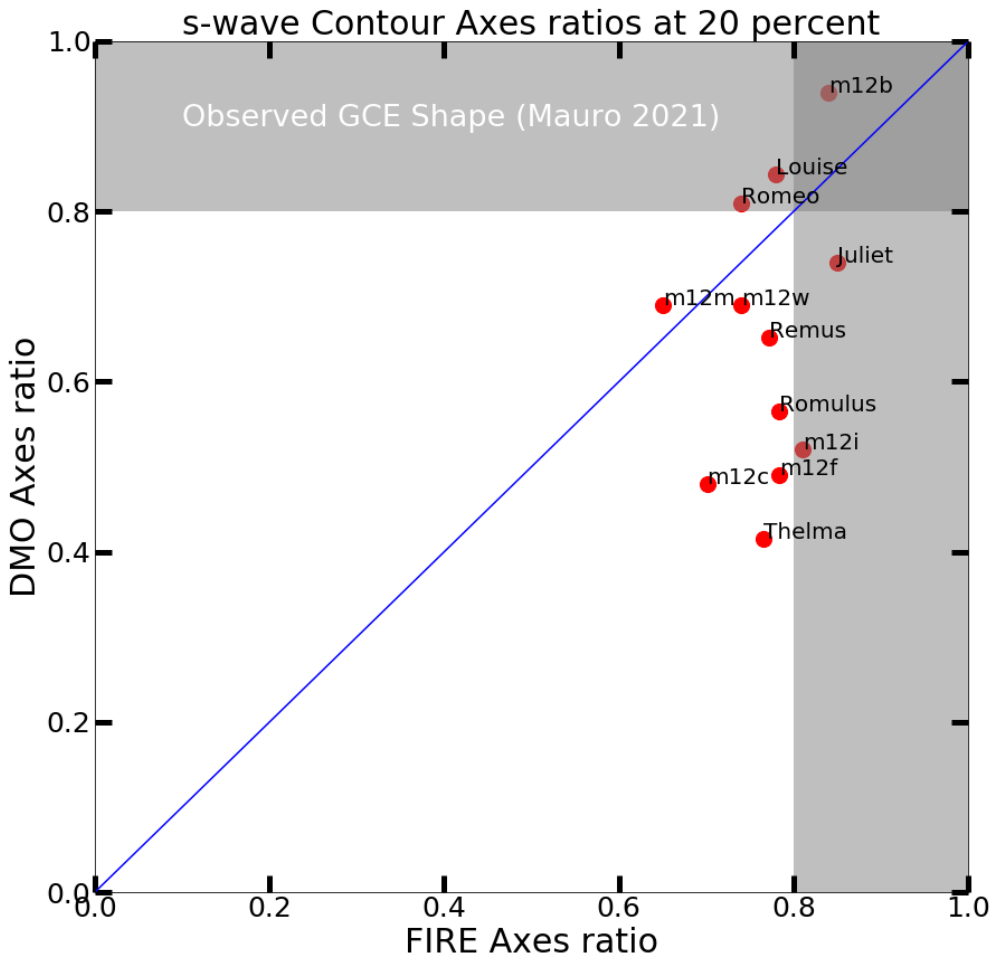

Figure 3.10: Ratios of axes (semi-minor/semi-major) of contour fits for s-wave at the 20 percent peak value of DJ/DO for the given halo. Note that FIRE halos have ratios of semi-minor to semi-major that are close to 0.8, while for DMO the axes range 0.4 to almost 1.

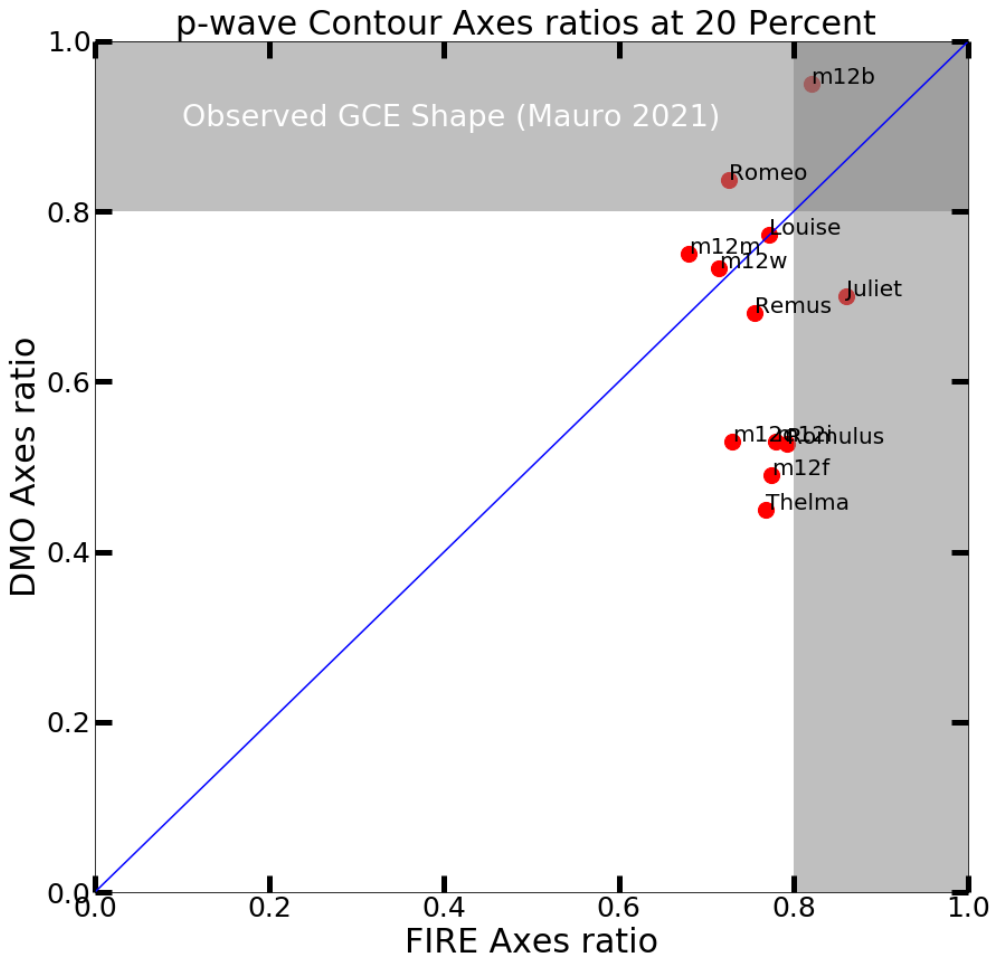

Figure 3.11: Ratios of axes (semi-minor/semi-major) of contour fits for p-wave at the 20 percent peak value of DJ/DO for the given halo. Note that FIRE halos have ratios of semi-minor to semi-major that are close to 0.8, while for DMO the axes range 0.4 to almost 1.

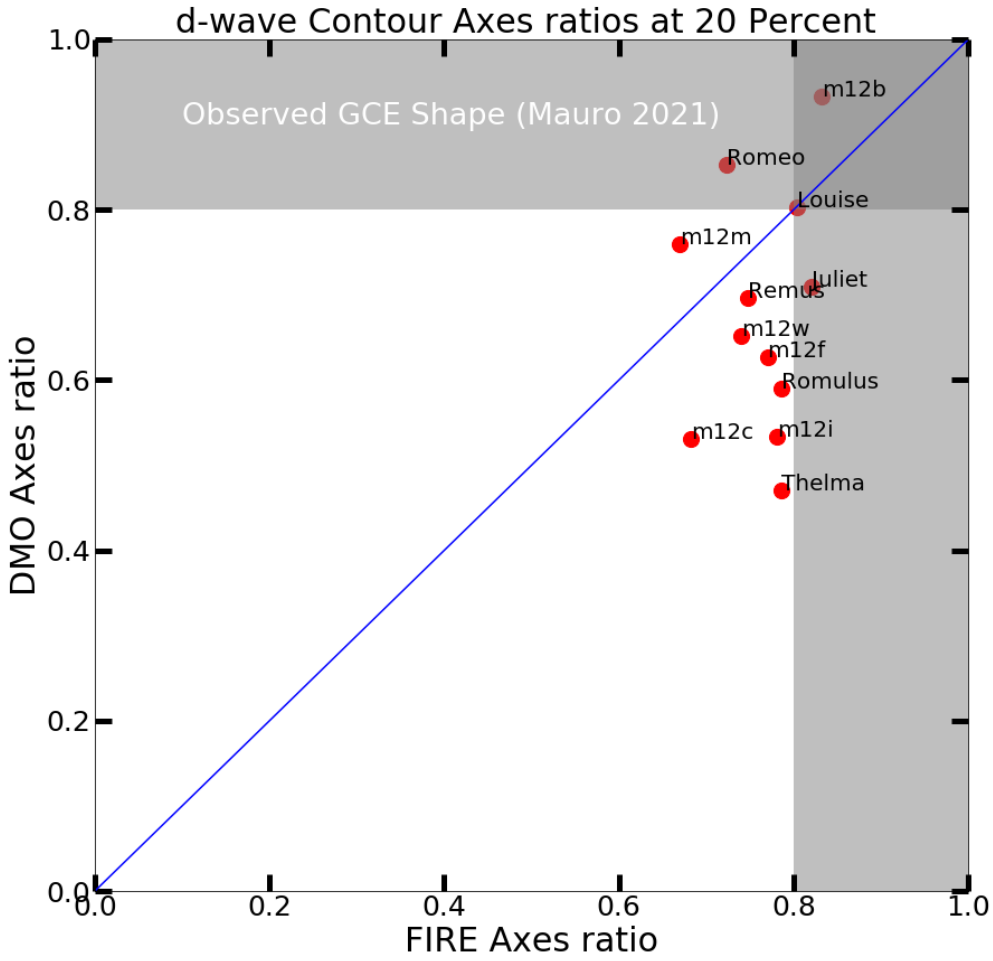

Figure 3.12: Ratios of axes (semi-minor/semi-major) of contour fits for d-wave at the 20 percent peak value of DJ/DO for the given halo. Note that for d-wave FIRE the ratios of semi-minor to semi-major are even more constrained and even closer to the value of 0.8, while for DMO the axes range slightly above 0.4 to almost 1.

3.5 Axes Ratios at Specific Contour Values

We have consistently found that FIRE halos have a much greater extent, particularly for p and d waves. Here we also show the ratios of major axes for FIRE/DMO halos. As can be seen in figures 3.13, 3.14 and 3.15, The ratios of semi- minor to semi- major axes show a greater range than the same ratios when the contour is chosen at the 20 percent of peak value for each halo. Here we see that even for the case of fixed levels for s,p, and d-wave DJ/DO, the majority of FIRE halos approach 0.8 for s wave, with notable outliers m12m. Interestingly, m12m comes much closer to 0.8 for p-wave and d-wave.

3.6 Conclusion

Using high-resolution zoom cosmological simulations of Milky-Way analogs described in 2.1, we have constructed sky maps of dJ/DΩ for s,p and d-wave dark matter annihilation models and explored their shapes on the sky. Examples of these maps are shown in Figures 2.5 - 2.10. In order to quantify the shape of the emission on the sky we have fit ellipses to contours of constant dJ/DΩ emission. From this analysis we report the following results:

1. Fully self-consistent galaxy formation FIRE runs produce fairly circular emission contours, with the ratio of semi-minor to semi-major axes is typically ~ 0.8 for all three annihilation models considered. The full range of ratios is $0.65 - 0.87$.

2. Less complete, DMO runs display a much larger range of shapes on the sky $(0.4 - 0.95)$ and are typically more elliptical than their FIRE counterparts.

3. For FIRE runs, we find that the major axis of the J-factor contours align closely with the galactic plane, within a few degrees for all cases.

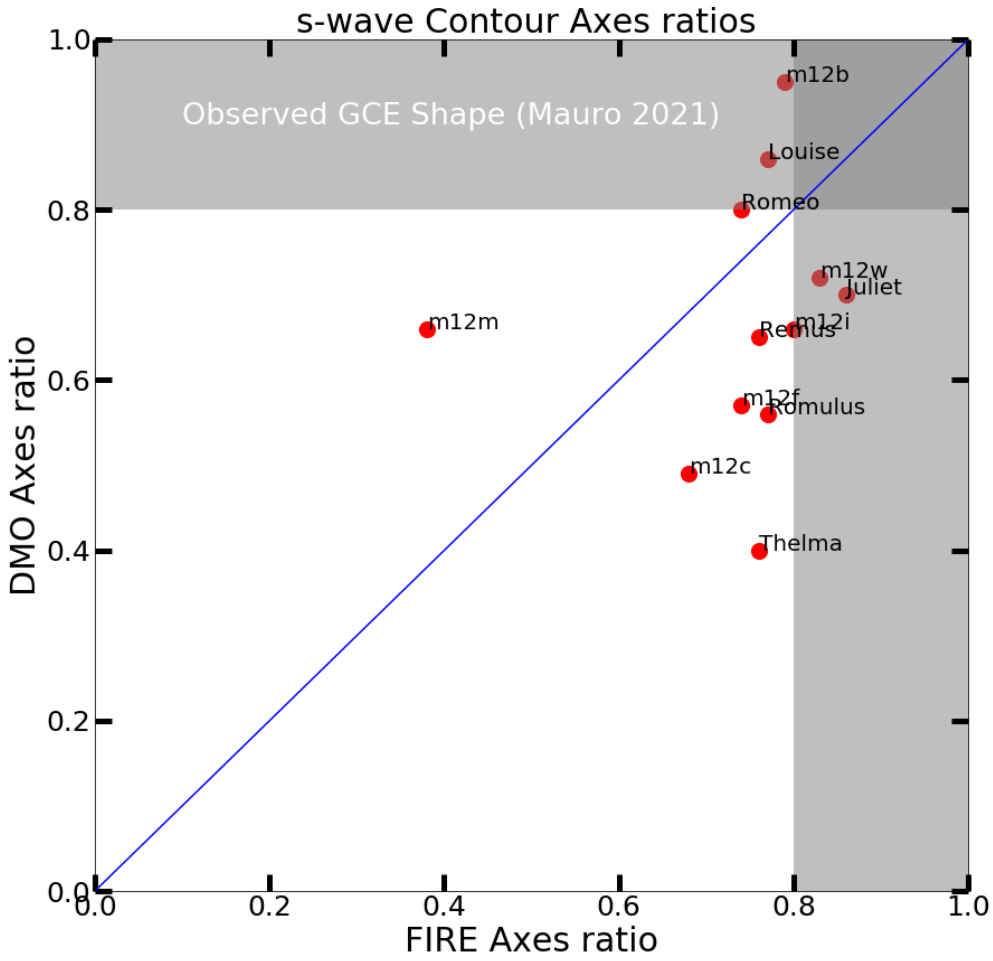

Figure 3.13: Ratios of axes (semi-minor/semi-major) of contour fits for s-wave for fixed value DJ/DO (10^{24}) Note that for s-wave the values are less constrained than for ratios taken at 20 percent values (see Chapter 3) and vary from 0.65 to 0.85 for FIRE, while for DMO the axes range from below 0.4 to almost 1.

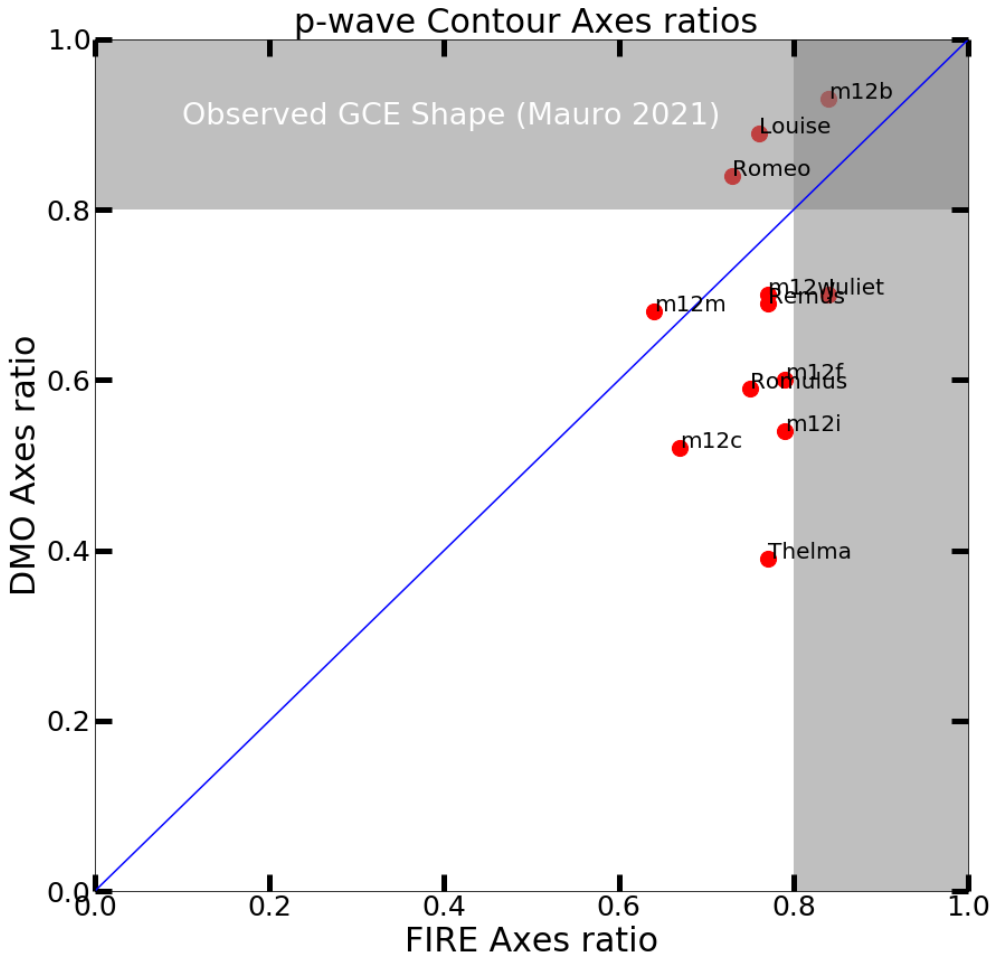

Figure 3.14: Ratios of axes (semi-minor/semi-major) of contour fits for p-wave for fixed value DJ/DO ($10^{17.5}$) Note that for p-wave the values are less constrained than for contours chosen at 20 percent of peak (see Chapter 3) and vary from 0.65 to 0.85 for FIRE, while for DMO the axes range from below 0.4 to almost 1.

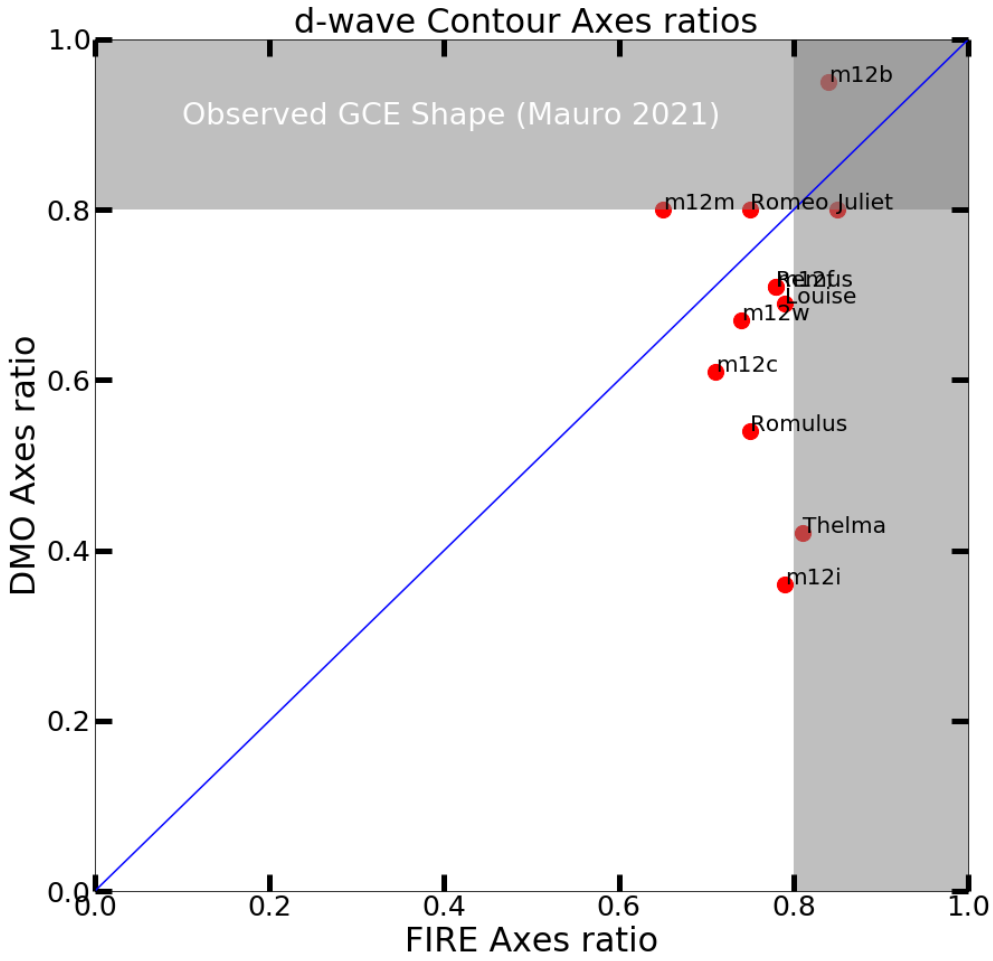

Figure 3.15: Ratios of axes (semi-minor/semi-major) of contour fits for d-wave for fixed value DJ/DO ($10^{11.5}$) Note that for d-wave the values are less constrained than when contours are chosen from the 20 percent peak (see Chapter 3) and vary from 0.65 to 0.85 for FIRE, while for DMO the axes range from below 0.4 to almost 1.

These results provide new expectations for the shape of dark matter annihilation emission signals. Specifically, if analysis priors were based on DMO expectations (which is standard) we would assume semi-minor to semi-major axes with a range of values for s,p,and d-wave emission (see Figures 3.10 , 3.11, and 3.12.) On the contrary, for the more accurate FIRE halos, the same ratios for the axes have a much narrow range of expected values near ~ 0.8. This is critical, as it shows a new expectation for what the expected signal would be in terms of its shape.

We also find that the major axis of the J-factor maps for FIRE halos are always aligned with the galactic plane within a few degrees, meaning that excess emission out of the plane would be hard to explain with a dark matter annihilation signal. We have provided the angles measured with respect to the galactic plane in tables 3.4,3.5,3.6,3.7,3.8, and 3.9).

There has been some debate in the literature on the shape of emission in the Galactic Center Excess. Ref. [61] find that the excess is described by a "boxy bulge" shape, with short to long axis ratio (in our language) ~ 0.55. This is quite flattened compared to our best-derived expectations from FIRE simulations (though not outside the realm that would have been expected from our DMO simulations, for example `ThelmaDMO` is more flattened than this.). Indeed Ref.[2] have used this result to rule out a large class of thermal s-wave WIMP models. Interestingly, however, [26] found that the Galactic Center Excess has a shape on the sky well fit by an ellipsoid with a fairly round axis ratio $\sim 0.8 - 1$. This shape of excess would be more easily explained by the shapes we report here.

Our theoretical results are in broad agreement with previous work, though no one has previously presented the same analysis and had comparable resolution. [12] used a J-factor-weighted inertia tensor over the whole sky and found that fully hydrodynamic halos tended to produce systematically more circular shapes on the sky than dark matter only versions. Though not defined in precisely the same way, they report typical values of ~ 0.8 for the associated axis ratios, in good agreement with our work.

Future indirect searches for annihilating dark matter in the Milky Way, M31, and other galaxies will continue to rely on templates to model possible sources. We have provided results that should be useful for dark matter templates here. In the future it would be interesting to use simulations to look at whether the stellar maps correlate with or inform the expected dark matter shape in ways that provide more information. Higher resolution simulations (with 8-times better mass resolution and improved, FIRE-3 physics) will provide an important tool for this exploration. This is something we will do in the future.

Bibliography

[1] K. N. Abazajian. The consistency of Fermi-LAT observations of the galactic center with a millisecond pulsar population in the central stellar cluster. , 2011(3):010, Mar. 2011.

[2] K. N. Abazajian, S. Horiuchi, M. Kaplinghat, R. E. Keeley, and O. Macias. Strong constraints on thermal relic dark matter from Fermi-LAT observations of the Galactic Center. , 102(4):043012, Aug. 2020.

[3] K. N. Abazajian and M. Kaplinghat. Detection of a gamma-ray source in the Galactic Center consistent with extended emission from dark matter annihilation and concentrated astrophysical emission. , 86(8):083511, Oct. 2012.

[4] M. Ackermann, M. Ajello, A. Albert, A. Allafort, W. Atwood, M. Axelsson, L. Baldini, J. Ballet, G. Barbiellini, D. Bastieri, et al. The fermi large area telescope on orbit: event classification, instrument response functions, and calibration. *The Astrophysical Journal Supplement Series*, 203(1):4, 2012.

[5] M. Ackermann, M. Ajello, A. Albert, W. B. Atwood, L. Baldini, J. Ballet, G. Barbiellini, D. Bastieri, R. Bellazzini, E. Bissaldi, R. D. Blandford, E. D. Bloom, R. Bonino, E. Bottacini, T. J. Brandt, J. Bregeon, P. Bruel, R. Buehler, T. H. Burnett, R. A. Cameron, R. Caputo, M. Caragiulo, P. A. Caraveo, E. Cavazzuti, C. Cecchi, E. Charles, A. Chekhtman, J. Chiang, A. Chiappo, G. Chiaro, S. Ciprini, J. Conrad, F. Costanza, A. Cuoco, S. Cutini, F. D'Ammando, F. de Palma, R. Desiante, S. W. Digel, N. Di Lalla, M. Di Mauro, L. Di Venere, P. S. Drell, C. Favuzzi, S. J. Fegan, E. C. Ferrara, W. B. Focke, A. Franckowiak, Y. Fukazawa, S. Funk, P. Fusco, F. Gargano, D. Gasparrini, N. Giglietto, F. Giordano, M. Giroletti, T. Glanzman, G. A. Gomez-Vargas, D. Green, I. A. Grenier, J. E. Grove, L. Guillemot, S. Guiriec, M. Gustafsson, A. K. Harding, E. Hays, J. W. Hewitt, D. Horan, T. Jogler, A. S. Johnson, T. Kamae, D. Kocevski, M. Kuss, G. La Mura, S. Larsson, L. Latronico, J. Li, F. Longo, F. Loparco, M. N. Lovellette, P. Lubrano, J. D. Magill, S. Maldera, D. Malyshev, A. Manfreda, P. Martin, M. N. Mazziotta, P. F. Michelson, N. Mirabal, W. Mitthumsiri, T. Mizuno, A. A. Moiseev, M. E. Monzani, A. Morselli, M. Negro, E. Nuss, T. Ohsugi, M. Orienti, E. Orlando, J. F. Ormes, D. Paneque, J. S. Perkins, M. Persic, M. Pesce-Rollins, F. Piron, G. Principe, S. Rainò, R. Rando, M. Razzano, S. Razzaque, A. Reimer, O. Reimer, M. Sánchez-Conde, C. Sgrò, D. Simone, E. J. Siskind, F. Spada, G. Spandre, P. Spinelli, D. J. Suson, H. Tajima, K. Tanaka, J. B. Thayer, L. Tibaldo, D. F. Torres, E. Troja, Y. Uchiyama, G. Vianello, K. S. Wood, M. Wood, G. Zaharijas, S. Zimmer, and Fermi

LAT Collaboration. The Fermi Galactic Center GeV Excess and Implications for Dark Matter. , 840(1):43, May 2017.

[6] M. Ajello, A. Albert, W. B. Atwood, G. Barbiellini, D. Bastieri, K. Bechtol, R. Bellazzini, E. Bissaldi, R. D. Blandford, E. D. Bloom, R. Bonino, E. Bottacini, T. J. Brandt, J. Bregeon, P. Bruel, R. Buehler, S. Buson, G. A. Caliandro, R. A. Cameron, R. Caputo, M. Caragiulo, P. A. Caraveo, C. Cecchi, A. Chekhtman, J. Chiang, G. Chiaro, S. Ciprini, J. Cohen-Tanugi, L. R. Cominsky, J. Conrad, S. Cutini, F. D'Ammando, A. de Angelis, F. de Palma, R. Desiante, L. Di Venere, P. S. Drell, C. Favuzzi, E. C. Ferrara, P. Fusco, F. Gargano, D. Gasparrini, N. Giglietto, P. Giommi, F. Giordano, M. Giroletti, T. Glanzman, G. Godfrey, G. A. Gomez-Vargas, I. A. Grenier, S. Guiriec, M. Gustafsson, A. K. Harding, J. W. Hewitt, A. B. Hill, D. Horan, T. Jogler, G. Jóhannesson, A. S. Johnson, T. Kamae, C. Karwin, J. Knödlseder, M. Kuss, S. Larsson, L. Latronico, J. Li, L. Li, F. Longo, F. Loparco, M. N. Lovellette, P. Lubrano, J. Magill, S. Maldera, D. Malyshev, A. Manfreda, M. Mayer, M. N. Mazziotta, P. F. Michelson, W. Mitthumsiri, T. Mizuno, A. A. Moiseev, M. E. Monzani, A. Morselli, I. V. Moskalenko, S. Murgia, E. Nuss, M. Ohno, T. Ohsugi, N. Omodei, E. Orlando, J. F. Ormes, D. Paneque, M. Pesce-Rollins, F. Piron, G. Pivato, T. A. Porter, S. Rainò, R. Rando, M. Razzano, A. Reimer, O. Reimer, S. Ritz, M. Sánchez-Conde, P. M. Saz Parkinson, C. Sgrò, E. J. Siskind, D. A. Smith, F. Spada, G. Spandre, P. Spinelli, D. J. Suson, H. Tajima, H. Takahashi, J. B. Thayer, D. F. Torres, G. Tosti, E. Troja, Y. Uchiyama, G. Vianello, B. L. Winer, K. S. Wood, G. Zaharijas, and S. Zimmer. Fermi-LAT Observations of High-Energy Gamma-Ray Emission toward the Galactic Center. , 819(1):44, Mar. 2016.

[7] B. Allgood, R. A. Flores, J. R. Primack, A. V. Kravtsov, R. H. Wechsler, A. Faltenbacher, and J. S. Bullock. The shape of dark matter haloes: dependence on mass, redshift, radius and formation. , 367(4):1781–1796, Apr. 2006.

[8] C. A. Argüelles, A. Diaz, A. Kheirandish, A. Olivares-Del-Campo, I. Safa, and A. C. Vincent. Dark Matter Annihilation to Neutrinos. *arXiv e-prints*, page arXiv:1912.09486, Dec. 2019.

[9] R. Bartels, S. Krishnamurthy, and C. Weniger. Strong Support for the Millisecond Pulsar Origin of the Galactic Center GeV Excess. , 116(5):051102, Feb. 2016.

[10] R. Bartels, E. Storm, C. Weniger, and F. Calore. The Fermi-LAT GeV excess as a tracer of stellar mass in the Galactic bulge. *Nature Astronomy*, 2:819–828, Aug. 2018.

[11] L. Bergström, P. Ullio, and J. H. Buckley. Observability of γ rays from dark matter neutralino annihilations in the Milky Way halo. *Astroparticle Physics*, 9(2):137–162, Aug. 1998.

[12] N. Bernal, L. Necib, and T. R. Slatyer. Spherical cows in dark matter indirect detection. *Journal of Cosmology and Astroparticle Physics*, 2016(12):030, 2016.

[13] G. Bertone and D. Hooper. History of dark matter. *Reviews of Modern Physics*, 90(4):045002, Oct. 2018.

[14] G. Bertone, D. Hooper, and J. Silk. Particle dark matter: evidence, candidates and constraints. , 405(5-6):279–390, Jan. 2005.

[15] E. Board, N. Bozorgnia, L. E. Strigari, R. J. J. Grand, A. Fattahi, C. S. Frenk, F. Marinacci, J. F. Navarro, and K. A. Oman. Velocity-dependent J-factors for annihilation radiation from cosmological simulations. , 2021(4):070, Apr. 2021.

[16] K. K. Boddy, J. Kumar, and L. E. Strigari. Effective J -factor of the Galactic Center for velocity-dependent dark matter annihilation. , 98(6):063012, Sept. 2018.

[17] A. Boehle, A. M. Ghez, R. Schödel, L. Meyer, S. Yelda, S. Albers, G. D. Martinez, E. E. Becklin, T. Do, J. R. Lu, K. Matthews, M. R. Morris, B. Sitarski, and G. Witzel. An Improved Distance and Mass Estimate for Sgr A* from a Multistar Orbit Analysis. , 830(1):17, Oct. 2016.

[18] G. L. Bryan and M. L. Norman. Statistical Properties of X-Ray Clusters: Analytic and Numerical Comparisons. , 495(1):80–99, Mar. 1998.

[19] E. Carlson and S. Profumo. Cosmic ray protons in the inner galaxy and the galactic center gamma-ray excess. *Physical Review D*, 90(2):023015, 2014.

[20] J. Choquette, J. M. Cline, and J. M. Cornell. p -wave annihilating dark matter from a decaying predecessor and the Galactic Center excess. , 94(1):015018, July 2016.

[21] K. T. E. Chua, A. Pillepich, M. Vogelsberger, and L. Hernquist. Shape of dark matter haloes in the Illustris simulation: effects of baryons. , 484(1):476–493, Mar. 2019.

[22] K. T. E. Chua, M. Vogelsberger, A. Pillepich, and L. Hernquist. The impact of galactic feedback on the shapes of dark-matter haloes. , July 2022.

[23] T. Daylan, D. P. Finkbeiner, D. Hooper, T. Linden, S. K. Portillo, N. L. Rodd, and T. R. Slatyer. The characterization of the gamma-ray signal from the central milky way: A case for annihilating dark matter. *Physics of the Dark Universe*, 12:1–23, 2016.

[24] V. P. Debattista, O. A. Gonzalez, R. E. Sanderson, K. El-Badry, S. Garrison-Kimmel, A. Wetzel, C.-A. Faucher-Giguère, and P. F. Hopkins. Formation, vertex deviation, and age of the Milky Way's bulge: input from a cosmological simulation with a late-forming bar. , 485(4):5073–5085, June 2019.

[25] V. P. Debattista, B. Moore, T. Quinn, S. Kazantzidis, R. Maas, L. Mayer, J. Read, and J. Stadel. The Causes of Halo Shape Changes Induced by Cooling Baryons: Disks versus Substructures. , 681(2):1076–1088, July 2008.

[26] M. Di Mauro. Characteristics of the galactic center excess measured with 11 years of f e r m i-lat data. *Physical Review D*, 103(6):063029, 2021.

[27] J. Diemand, M. Kuhlen, and P. Madau. Dark Matter Substructure and Gamma-Ray Annihilation in the Milky Way Halo. , 657(1):262–270, Mar. 2007.

[28] J. T. Dinsmore and T. R. Slatyer. Luminosity functions consistent with a pulsar-dominated Galactic Center excess. , 2022(6):025, June 2022.

[29] S. Dodelson. *Modern cosmology*. Elsevier, 2003.

[30] J. Einasto, A. Kaasik, and E. Saar. Dynamic evidence on massive coronas of galaxies. , 250(5464):309–310, July 1974.

[31] C.-A. Faucher-Giguère, A. Lidz, M. Zaldarriaga, and L. Hernquist. A New Calculation of the Ionizing Background Spectrum and the Effects of He II Reionization. , 703(2):1416–1443, Oct. 2009.

[32] J. L. Feng. Supersymmetry and Cosmology. *arXiv e-prints*, pages hep–ph/0405215, May 2004.

[33] S. Garrison-Kimmel, P. F. Hopkins, A. Wetzel, J. S. Bullock, M. Boylan-Kolchin, D. Kereš, C.-A. Faucher-Giguère, K. El-Badry, A. Lamberts, E. Quataert, and R. Sand erson. The Local Group on FIRE: dwarf galaxy populations across a suite of hydrodynamic simulations. , 487(1):1380–1399, July 2019.

[34] S. Garrison-Kimmel, P. F. Hopkins, A. Wetzel, K. El-Badry, R. E. Sanderson, J. S. Bullock, X. Ma, F. van de Voort, Z. Hafen, C.-A. Faucher-Giguère, C. C. Hayward, E. Quataert, D. Kereš, and M. Boylan-Kolchin. The origin of the diverse morphologies and kinematics of Milky Way-mass galaxies in the FIRE-2 simulations. , 481(3):4133–4157, Dec. 2018.

[35] S. Garrison-Kimmel, A. Wetzel, J. S. Bullock, P. F. Hopkins, M. Boylan-Kolchin, C.-A. Faucher-Giguère, D. Kereš, E. Quataert, R. E. Sanderson, A. S. Graus, et al. Not so lumpy after all: modelling the depletion of dark matter subhaloes by milky way-like galaxies. *Monthly Notices of the Royal Astronomical Society*, 471(2):1709–1727, 2017.

[36] S. Garrison-Kimmel, A. Wetzel, J. S. Bullock, P. F. Hopkins, M. Boylan-Kolchin, C.-A. Faucher-Giguère, D. Kereš, E. Quataert, R. E. Sanderson, A. S. Graus, and T. Kelley. Not so lumpy after all: modelling the depletion of dark matter subhaloes by Milky Way-like galaxies. , 471(2):1709–1727, Oct. 2017.

[37] S. Garrison-Kimmel, A. Wetzel, P. F. Hopkins, R. Sanderson, K. El-Badry, A. Graus, T. K. Chan, R. Feldmann, M. Boylan-Kolchin, C. C. Hayward, J. S. Bullock, A. Fitts, J. Samuel, C. Wheeler, D. Kereš, and C.-A. Faucher-Giguère. Star formation histories of dwarf galaxies in the FIRE simulations: dependence on mass and Local Group environment. , 489(4):4574–4588, Nov. 2019.

[38] J. M. Gaskins. A review of indirect searches for particle dark matter. *Contemporary Physics*, 57(4):496–525, Oct. 2016.

[39] F. Giacchino, L. Lopez-Honorez, and M. H. G. Tytgat. Scalar dark matter models with significant internal bremsstrahlung. , 2013(10):025, Oct. 2013.

[40] R. J. J. Grand and S. D. M. White. Baryonic effects on the detectability of annihilation radiation from dark matter subhaloes around the Milky Way. , 501(3):3558–3567, Mar. 2021.

[41] R. Guo, C. Liu, S. Mao, X.-X. Xue, R. J. Long, and L. Zhang. Measuring the local dark matter density with LAMOST DR5 and Gaia DR2. *Monthly Notices of the Royal Astronomical Society*, 495(4):4828–4844, 05 2020.

[42] A. B. Gurvich. FIRE Studio: Movie making utilities for the FIRE simulations, Feb. 2022.

[43] O. Hahn and T. Abel. Multi-scale initial conditions for cosmological simulations. , 415(3):2101–2121, Aug. 2011.

[44] D. Hooper and L. Goodenough. Dark matter annihilation in the Galactic Center as seen by the Fermi Gamma Ray Space Telescope. *Physics Letters B*, 697(5):412–428, Mar. 2011.

[45] P. F. Hopkins. A new class of accurate, mesh-free hydrodynamic simulation methods. , 450:53–110, June 2015.

[46] P. F. Hopkins, A. Wetzel, D. Kereš, C.-A. Faucher-Giguère, E. Quataert, M. Boylan-Kolchin, N. Murray, C. C. Hayward, S. Garrison-Kimmel, C. Hummels, R. Feldmann, P. Torrey, X. Ma, D. Anglés-Alcázar, K.-Y. Su, M. Orr, D. Schmitz, I. Escala, R. Sanderson, M. Y. Grudić, Z. Hafen, J.-H. Kim, A. Fitts, J. S. Bullock, C. Wheeler, T. K. Chan, O. D. Elbert, and D. Narayanan. FIRE-2 simulations: physics versus numerics in galaxy formation. , 480(1):800–863, Oct 2018.

[47] C. Johnson, R. Caputo, C. Karwin, S. Murgia, S. Ritz, J. Shelton, F.-L. Collaboration, et al. Search for gamma-ray emission from p-wave dark matter annihilation in the galactic center. *Physical Review D*, 99(10):103007, 2019.

[48] G. Jungman, M. Kamionkowski, and K. Griest. Supersymmetric dark matter. , 267:195–373, Mar. 1996.

[49] M. Kamionkowski, S. M. Koushiappas, and M. Kuhlen. Galactic substructure and dark-matter annihilation in the Milky Way halo. , 81(4):043532, Feb. 2010.

[50] C. Karwin, S. Murgia, I. Moskalenko, S. Fillingham, A.-K. Burns, and M. Fieg. Dark Matter Interpretation of the Fermi-LAT Observations Toward the Outer Halo of M31. *arXiv e-prints*, page arXiv:2010.08563, Oct. 2020.

[51] C. Karwin, S. Murgia, T. M. P. Tait, T. A. Porter, and P. Tanedo. Dark matter interpretation of the Fermi-LAT observation toward the Galactic Center. , 95(10):103005, May 2017.

[52] T. Kelley, J. S. Bullock, S. Garrison-Kimmel, M. Boylan-Kolchin, M. S. Pawlowski, and A. S. Graus. Phat ELVIS: The inevitable effect of the Milky Way's disc on its dark matter subhaloes. , 487(3):4409–4423, Aug. 2019.

[53] S. S. Kimura, K. Murase, and P. Mészáros. Soft gamma rays from low accreting supermassive black holes and connection to energetic neutrinos. *Nature communications*, 12(1):1–11, 2021.

[54] T. Kolb. *The early universe*. Addison-Wesley, 1990.

[55] J. Kormendy and L. C. Ho. Coevolution (Or Not) of Supermassive Black Holes and Host Galaxies. , 51(1):511–653, Aug. 2013.

[56] M. R. Krumholz and N. Y. Gnedin. A Comparison of Methods for Determining the Molecular Content of Model Galaxies. , 729(1):36, Mar 2011.

[57] J. Kwan, C. Sánchez, J. Clampitt, J. Blazek, M. Crocce, B. Jain, J. Zuntz, A. Amara, M. R. Becker, G. M. Bernstein, C. Bonnett, J. DeRose, S. Dodelson, T. F. Eifler, E. Gaztanaga, T. Giannantonio, D. Gruen, W. G. Hartley, T. Kacprzak, D. Kirk, E. Krause, N. MacCrann, R. Miquel, Y. Park, A. J. Ross, E. Rozo, E. S. Rykoff, E. Sheldon, M. A. Troxel, R. H. Wechsler, T. M. C. Abbott, F. B. Abdalla, S. Allam, A. Benoit-Lévy, D. Brooks, D. L. Burke, A. C. Rosell, M. Carrasco Kind, C. E. Cunha, C. B. D'Andrea, L. N. da Costa, S. Desai, H. T. Diehl, J. P. Dietrich, P. Doel, A. E. Evrard, E. Fernandez, D. A. Finley, B. Flaugher, P. Fosalba, J. Frieman, D. W. Gerdes, R. A. Gruendl, G. Gutierrez, K. Honscheid, D. J. James, M. Jarvis, K. Kuehn, O. Lahav, M. Lima, M. A. G. Maia, J. L. Marshall, P. Martini, P. Melchior, J. J. Mohr, R. C. Nichol, B. Nord, A. A. Plazas, K. Reil, A. K. Romer, A. Roodman, E. Sanchez, V. Scarpine, I. Sevilla-Noarbe, R. C. Smith, M. Soares-Santos, F. Sobreira, E. Suchyta, M. E. C. Swanson, G. Tarle, D. Thomas, V. Vikram, A. R. Walker, and DES Collaboration. Cosmology from large-scale galaxy clustering and galaxy-galaxy lensing with Dark Energy Survey Science Verification data. , 464(4):4045–4062, Feb. 2017.

[58] A. Lazar, J. S. Bullock, M. Boylan-Kolchin, T. Chan, P. F. Hopkins, A. S. Graus, A. Wetzel, K. El-Badry, C. Wheeler, M. C. Straight, et al. A dark matter profile to model diverse feedback-induced core sizes of λcdm haloes. *Monthly Notices of the Royal Astronomical Society*, 497(2):2393–2417, 2020.

[59] M. Lisanti. Lectures on Dark Matter Physics. In J. Polchinski and et al., editors, *New Frontiers in Fields and Strings (TASI 2015*, pages 399–446, Jan. 2017.

[60] X. Ma, P. F. Hopkins, A. R. Wetzel, E. N. Kirby, D. Anglés-Alcázar, C.-A. Faucher-Giguère, D. Kereš, and E. Quataert. The structure and dynamical evolution of the stellar disc of a simulated Milky Way-mass galaxy. , 467(2):2430–2444, May 2017.

[61] O. Macias, C. Gordon, R. M. Crocker, B. Coleman, D. Paterson, S. Horiuchi, and M. Pohl. Galactic bulge preferred over dark matter for the Galactic centre gamma-ray excess. *Nature Astronomy*, 2:387–392, Mar. 2018.

[62] R. Mandelbaum, A. Slosar, T. Baldauf, U. Seljak, C. M. Hirata, R. Nakajima, R. Reyes, and R. E. Smith. Cosmological parameter constraints from galaxy-galaxy lensing and galaxy clustering with the SDSS DR7. , 432(2):1544–1575, June 2013.

[63] A. Martin, J. Shelton, and J. Unwin. Fitting the Galactic Center gamma-ray excess with cascade annihilations. , 90(10):103513, Nov. 2014.

[64] F. J. Mercado, J. S. Bullock, M. Boylan-Kolchin, J. Moreno, A. Wetzel, K. El-Badry, A. S. Graus, A. Fitts, P. F. Hopkins, C.-A. Faucher-Giguère, et al. A relationship between stellar metallicity gradients and galaxy age in dwarf galaxies. *Monthly Notices of the Royal Astronomical Society*, 501(4):5121–5134, 2021.

[65] H. Mo, F. Van den Bosch, and S. White. *Galaxy formation and evolution*. Cambridge University Press, 2010.

[66] J. J. Monaghan. Smoothed particle hydrodynamics. , 30:543–574, Jan. 1992.

[67] S. Murgia. The fermi lat galactic center excess: Evidence of annihilating dark matter? *Annual Review of Nuclear and Particle Science*, 70(1):455–483, 2020.

[68] L. Necib, M. Lisanti, S. Garrison-Kimmel, A. Wetzel, R. Sanderson, P. F. Hopkins, C.-A. Faucher-Giguère, and D. Kereš. Under the firelight: stellar tracers of the local dark matter velocity distribution in the milky way. *The Astrophysical Journal*, 883(1):27, 2019.

[69] J. Oñorbe, S. Garrison-Kimmel, A. H. Maller, J. S. Bullock, M. Rocha, and O. Hahn. How to zoom: bias, contamination and Lagrange volumes in multimass cosmological simulations. , 437(2):1894–1908, Jan. 2014.

[70] M. E. Orr, C. C. Hayward, P. F. Hopkins, T. K. Chan, C.-A. Faucher-Giguère, R. Feldmann, D. Kereš, N. Murray, and E. Quataert. What FIREs up star formation: the emergence of the Kennicutt-Schmidt law from feedback. , 478(3):3653–3673, Aug 2018.

[71] S. Peirani, Y. Dubois, M. Volonteri, J. Devriendt, K. Bundy, J. Silk, C. Pichon, S. Kaviraj, R. Gavazzi, and M. Habouzit. Density profile of dark matter haloes and galaxies in the horizon–agn simulation: the impact of agn feedback. *Monthly Notices of the Royal Astronomical Society*, 472(2):2153–2169, 2017.

[72] M. Petač, P. Ullio, and M. Valli. On velocity-dependent dark matter annihilations in dwarf satellites. , 2018(12):039, Dec. 2018.

[73] Planck Collaboration, N. Aghanim, Y. Akrami, M. Ashdown, J. Aumont, C. Baccigalupi, M. Ballardini, A. J. Banday, R. B. Barreiro, N. Bartolo, S. Basak, R. Battye, K. Benabed, J. P. Bernard, M. Bersanelli, P. Bielewicz, J. J. Bock, J. R. Bond, J. Borrill, F. R. Bouchet, F. Boulanger, M. Bucher, C. Burigana, R. C. Butler, E. Calabrese, J. F. Cardoso, J. Carron, A. Challinor, H. C. Chiang, J. Chluba, L. P. L. Colombo, C. Combet, D. Contreras, B. P. Crill, F. Cuttaia, P. de Bernardis, G. de Zotti, J. Delabrouille, J. M. Delouis, E. Di Valentino, J. M. Diego, O. Doré, M. Douspis, A. Ducout, X. Dupac, S. Dusini, G. Efstathiou, F. Elsner, T. A. Enßlin, H. K. Eriksen, Y. Fantaye, M. Farhang, J. Fergusson, R. Fernandez-Cobos, F. Finelli, F. Forastieri, M. Frailis,

A. A. Fraisse, E. Franceschi, A. Frolov, S. Galeotta, S. Galli, K. Ganga, R. T. Génova-Santos, M. Gerbino, T. Ghosh, J. González-Nuevo, K. M. Górski, S. Gratton, A. Gruppuso, J. E. Gudmundsson, J. Hamann, W. Handley, F. K. Hansen, D. Herranz, S. R. Hildebrandt, E. Hivon, Z. Huang, A. H. Jaffe, W. C. Jones, A. Karakci, E. Keihänen, R. Keskitalo, K. Kiiveri, J. Kim, T. S. Kisner, L. Knox, N. Krachmalnicoff, M. Kunz, H. Kurki-Suonio, G. Lagache, J. M. Lamarre, A. Lasenby, M. Lattanzi, C. R. Lawrence, M. Le Jeune, P. Lemos, J. Lesgourgues, F. Levrier, A. Lewis, M. Liguori, P. B. Lilje, M. Lilley, V. Lindholm, M. López-Caniego, P. M. Lubin, Y. Z. Ma, J. F. Macías-Pérez, G. Maggio, D. Maino, N. Mandolesi, A. Mangilli, A. Marcos-Caballero, M. Maris, P. G. Martin, M. Martinelli, E. Martínez-González, S. Matarrese, N. Mauri, J. D. McEwen, P. R. Meinhold, A. Melchiorri, A. Mennella, M. Migliaccio, M. Millea, S. Mitra, M. A. Miville-Deschênes, D. Molinari, L. Montier, G. Morgante, A. Moss, P. Natoli, H. U. Nørgaard-Nielsen, L. Pagano, D. Paoletti, B. Partridge, G. Patanchon, H. V. Peiris, F. Perrotta, V. Pettorino, F. Piacentini, L. Polastri, G. Polenta, J. L. Puget, J. P. Rachen, M. Reinecke, M. Remazeilles, A. Renzi, G. Rocha, C. Rosset, G. Roudier, J. A. Rubiño-Martín, B. Ruiz-Granados, L. Salvati, M. Sandri, M. Savelainen, D. Scott, E. P. S. Shellard, C. Sirignano, G. Sirri, L. D. Spencer, R. Sunyaev, A. S. Suur-Uski, J. A. Tauber, D. Tavagnacco, M. Tenti, L. Toffolatti, M. Tomasi, T. Trombetti, L. Valenziano, J. Valiviita, B. Van Tent, L. Vibert, P. Vielva, F. Villa, N. Vittorio, B. D. Wandelt, I. K. Wehus, M. White, S. D. M. White, A. Zacchei, and A. Zonca. Planck 2018 results. VI. Cosmological parameters. , 641:A6, Sept. 2020.

[74] B. E. Robertson and A. R. Zentner. Dark matter annihilation rates with velocity-dependent annihilation cross sections. , 79(8):083525, Apr. 2009.

[75] V. H. Robles, T. Kelley, J. S. Bullock, and M. Kaplinghat. The Milky Way's halo and subhaloes in self-interacting dark matter. , 490(2):2117–2123, Dec. 2019.

[76] V. C. Rubin, J. Ford, W. K., and N. Thonnard. Extended rotation curves of high-luminosity spiral galaxies. IV. Systematic dynamical properties, Sa -> Sc. , 225:L107–L111, Nov. 1978.

[77] O. Sameie, M. Boylan-Kolchin, R. Sanderson, D. Vargya, P. F. Hopkins, A. Wetzel, J. Bullock, A. Graus, and V. H. Robles. The central densities of Milky Way-mass galaxies in cold and self-interacting dark matter models. , 507(1):720–729, Oct. 2021.

[78] J. Samuel, A. Wetzel, E. Tollerud, S. Garrison-Kimmel, S. Loebman, K. El-Badry, P. F. Hopkins, M. Boylan-Kolchin, C.-A. Faucher-Giguère, J. S. Bullock, et al. A profile in fire: resolving the radial distributions of satellite galaxies in the local group with simulations. *Monthly Notices of the Royal Astronomical Society*, 491(1):1471–1490, 2020.

[79] R. Sanderson, A. Wetzel, S. Sharma, and P. Hopkins. Better Galactic Mass Models through Chemistry. *Galaxies*, 5(3):43, Aug. 2017.

[80] R. E. Sanderson, A. Wetzel, S. Loebman, S. Sharma, P. F. Hopkins, S. Garrison-Kimmel, C.-A. Faucher-Giguère, D. Kereš, and E. Quataert. Synthetic gaia surveys from the fire cosmological simulations of milky way-mass galaxies. *The Astrophysical Journal Supplement Series*, 246(1):6, 2020.

[81] X. Shen, P. F. Hopkins, L. Necib, F. Jiang, M. Boylan-Kolchin, and A. Wetzel. Dissipative dark matter on FIRE - I. Structural and kinematic properties of dwarf galaxies. , 506(3):4421–4445, Sept. 2021.

[82] V. Springel, S. D. M. White, C. S. Frenk, J. F. Navarro, A. Jenkins, M. Vogelsberger, J. Wang, A. Ludlow, and A. Helmi. Prospects for detecting supersymmetric dark matter in the Galactic halo. , 456(7218):73–76, Nov. 2008.

[83] G. Steigman, B. Dasgupta, and J. F. Beacom. Precise relic wimp abundance and its impact on searches for dark matter annihilation. *Phys. Rev. D*, 86:023506, Jul 2012.

[84] F. Stoehr, S. D. M. White, V. Springel, G. Tormen, and N. Yoshida. Dark matter annihilation in the halo of the Milky Way. , 345(4):1313–1322, Nov. 2003.

[85] N. Tominaga, K. Maeda, H. Umeda, K. Nomoto, M. Tanaka, N. Iwamoto, T. Suzuki, and P. A. Mazzali. The connection between gamma-ray bursts and extremely metal-poor stars: black hole-forming supernovae with relativistic jets. *The Astrophysical Journal*, 657(2):L77, 2007.

[86] V. Trimble. Existence and nature of dark matter in the universe. , 25:425–472, Jan. 1987.

[87] A. R. Wetzel, P. F. Hopkins, J.-h. Kim, C.-A. Faucher-Giguère, D. Kereš, and E. Quataert. Reconciling Dwarf Galaxies with ΛCDM Cosmology: Simulating a Realistic Population of Satellites around a Milky Way-mass Galaxy. , 827(2):L23, Aug. 2016.

[88] M. Winter, G. Zaharijas, K. Bechtol, and J. Vandenbroucke. Estimating the gev emission of millisecond pulsars in dwarf spheroidal galaxies. *The Astrophysical Journal Letters*, 832(1):L6, 2016.

[89] D. M. Wittman, J. A. Tyson, D. Kirkman, I. Dell'Antonio, and G. Bernstein. Detection of weak gravitational lensing distortions of distant galaxies by cosmic dark matter at large scales. , 405(6783):143–148, May 2000.

[90] F. Zimmer, O. Macias, S. Ando, R. M. Crocker, and S. Horiuchi. The andromeda gamma-ray excess: Background systematics of the millisecond pulsars and dark matter interpretations. *arXiv preprint arXiv:2204.00636*, 2022.